COINCIDENCE STUDY OF $^{27}Al(^{16}O,^{12}Cx)^{27}Al$ AT 65 MeV

BY

MAN-YEE B. TSANG

A dissertation submitted in partial fulfillment

of the requirements for the degree of

DOCTOR OF PHILOSOPHY

UNIVERSITY OF WASHINGTON

1980

University of Washington

Abstract

COINCIDENCE STUDY OF $^{27}Al(^{16}O,^{12}C\alpha)^{27}Al$ AT 65 MeV

by ManYee B. Tsang

Chairman of the Supervisory Committee: Professor Robert Vandenbosch

Department of Chemistry

A particle-particle coincidence technique was used to study the reaction mechanism for the $^{27}Al(^{16}O,^{12}C\alpha)$ reaction at 65 MeV ^{16}O bombarding energy. Both in-plane and out-of-plane ^{12}C-α angular correlations have been measured at two carbon detector angles, θ_c=-30° and -40°. The carbon particles were identified with a traditional DE-E telescope counter while both DE-E telescope and time-of-flight methods have been employed to identify the alpha particles. The time-of-flight method enables measurement of very low energy alpha particles at back angles.

In contrast with a previous study (Ha 77), in which the alpha particles were identified only by the telescope method, the C-α angular correlation from the present experiment shows a slight back angle rise past 90° when plotted in the center of mass system of $^{31}P^*$ and a strong forward angle peak towards the beam to the smallest angle measured. By fitting back angle and out-of-plane data, the majority of the C-α coincidence events can be accounted for by the evaporation of $^{31}P^*$. A small amount of alpha particles from the break-up of $^{16}O^*$ were detected at angles around that of the carbon detector. Less than 10% of the alpha particles

detected are of pre-equilibrium origin. This is in sharp contrast to the earlier results of Harris et al. (Ha 77a) which indicates that pre-equilibrium alpha decay is the dominant process. The extracted "pre-equilibrium" alpha emission exhibits strong forward peaking on the opposite side of the beam direction as the carbon detector. The average alpha energy of the pre-equilibrium component is higher than that of the evaporative component. For θ_c=-40°, both the in-plane and out-of-plane C-α angular correlations are consistent with evaporation from $^{31}P^*$.

A Monte-Carlo three-body trajectory computer program was written to study the dynamics of the ^{12}C, α and ^{27}Al exit channel in the combined Coulomb and nuclear force field. The ^{16}O is initially represented as a bound state of ^{12}C and α. Both the Woods-Saxon and proximity potentials have been used as nuclear potentials. Even though this calculation is much more ambitious and comprehensive than previous attempts, the results do not reproduce the experimental results.

Doctoral Dissertation

In presenting this dissertation in partial fulfillment of the requirements for the Doctoral degree at the University of Washington, I agree that the Library shall make its copies freely available for inspection. I further agree that extensive copying of this dissertation is allowable only for scholarly purposes. Requests for copying or reproduction of this dissertation may be referred to University Microfilms, 300 North Zeeb Road, Ann Arbor, Michigan 48106, to whom the author has granted "the right to reproduce and sell (a) copies of the manuscript in microform and/or (b) printed copies of the manuscript made from microform."

Signature Wanlee B. Tsang

Date June 10, 80

TABLE OF CONTENTS

LIST OF TABLES

LIST OF FIGURES

ACKNOWLEGEMENTS

I would like to express my deepest appreciation to my advisor and teacher, Professor Robert Vandenbosch who suggested this dissertation topic, for his advice and encouragement whenever the research work seemed to reach a dead end. In addition to the reading committee, I am also grateful to Professor Issac Halpern for reading this dissertation critically while making valuable suggestions and Professor Gouterman for his continued encouragement throughout my graduate study.

It has been a pleasure to have Dr. Raymond Puigh as a co-worker. I am indebted to him for many sleepless nights and weekends which he spent in trouble shooting and taking data for this work. His jokes and junk food sure made the time past faster and the atmosphere livelier. I would also like to thank Mr. Alan Seamster for his assistance in data taking.

Nearly everyone in the Nuclear Physics Lab has contributed one way or another in this dissertation. I am grateful to Professor William Weitkamp for giving me help and advice at various times during my stay in the Nuclear Physics Lab, and the technical staff for providing assistance in the machine operation both during and after working hours. I am especially indebted to Mr. Harold Fauska who spent one Thanksgiving weekend fixing up the interface of the computer for data taking. Most of the work that required the computers (including the manuscript of this

dissertation) would have been impossible without the help of Mr. Kelly Green and Mr. Richard Seymour. Mr. Louis Geissel, Mr. Allen Willman and the machine shop deserve credit for making some of the equipment used in this experiment.

No words can express my appreciation to Bill Lynch, my partner in life with whom I have learned experimental nuclear physics and so many enjoyable aspects of life. Without his help and support, this work would be impossible.

CHAPTER I

INTRODUCTION, BACKGROUND AND MOTIVATION

A. INTRODUCTION

In the past several years, there has been an increased interest in prompt or pre-equilibrium light particle emission in heavy ion reactions. The work described in this dissertation is an attempt to understand the nature of pre-equilibrium alpha particle emission in the light heavy ion system $^{27}Al + ^{16}O$ at 65 MeV. This chapter gives some general background for this type of experiment. In addition, a summary of the current understanding of alpha emission is presented. Finally, the motivation for the present work is given.

Although most studies of pre-equilibrium light particle emission are very recent, the importance of this reaction mechanism at energies of about 10 MeV per nucleon has been known for some time. In 1961, Britt and Quinton (Br 61) bombarded ^{12}C, ^{16}O and ^{14}N on Au and Bi. They detected the alpha particles coming out from the reaction. Typical incident energy of the projectiles was about 10 MeV/nucleon. The emitted alpha cross-section observed was quite large, about 30% of the total cross-section. The alpha particles were emitted predominantly in the forward direction. Even though no satisfactory explanation was given for the above phenomenon, the work was ignored for the following decade. Then, in 1970's after the discovery of

quasi-elastic and deeply inelastic scattering, there was renewed interest in light particle emission in heavy ion reactions.

Many papers have been published on quasi-elastic and deeply inelastic scattering including a review article by Schroder and Huizenga (Sc 77). One of the characteristics of the deeply inelastic scattering is the appearance in the energy spectrum of a broad bell shaped bump which peaked at energies well below the beam energy. Another is that the angular momentum transferred from the center of mass motion into internal degree of freedom is large; therefore light particle, especially alpha particle emission, is an important decay process since it carries away large amount of angular momentum. Various experiments have been conducted in recent years trying to understand the energy dissipation mechanism and time scale involved for the quasi elastic and deeply inelastic reactions. One type of experiment consists of detecting the alpha particle and a heavy fragment in coincidence. The measured angular correlations are distinctly anisotropic with strong peaking at forward scattering angles. From the width of the peak in the angular correlation, some authors have deduced a time scale of the reaction to be about 5×10^{-22} sec, far too short for equilibrium to be achieved.

B. Theoretical Considerations

1. Orbiting:

Experimentally, deeply inelastic scattering is distinguished from quasi-elastic scattering by the Q value of the

reaction. The reactions with very negative Q values are operationally defined as deeply inelastic scattering. Reactions with less negative Q values are labelled as quasi-elastic scattering. Wilczynski first proposed orbiting i.e. negative angle scattering to explain the deeply inelastic scattering observed in $^{232}Th + ^{40}Ar$ system (Wil 73). In negative angle scattering, the projectile orbits around the target and crosses over the beam axis as shown in the right of Fig. I-1a. In the remainder of this dissertation, quasi-elastic scattering and deeply inelastic scattering have been associated loosely with non-orbiting and orbiting trajectories respectively. In both cases, energy, charge and mass are exchanged between the projectile and target.

Recent experiments which measured the gamma-ray circular polarization have confirmed the orbiting phenomenon in some heavy ion systems (Tr 77) including the $^{27}Al + ^{16}O$ system at 100 MeV (Ha 78).

2. Sequential Process :

A large amount of mass and charge is transferred in a deeply inelastic reaction. The charge distribution of the reaction products peaks quite strongly around the charge of the projectile (We 77). This feature suggests that both the target and projectile substantially retain their identities in the reaction with emission of light particles. If the alpha particle is emitted after the two fragments are separated, one then can ask the question : Is the alpha particle emitted from a target-like

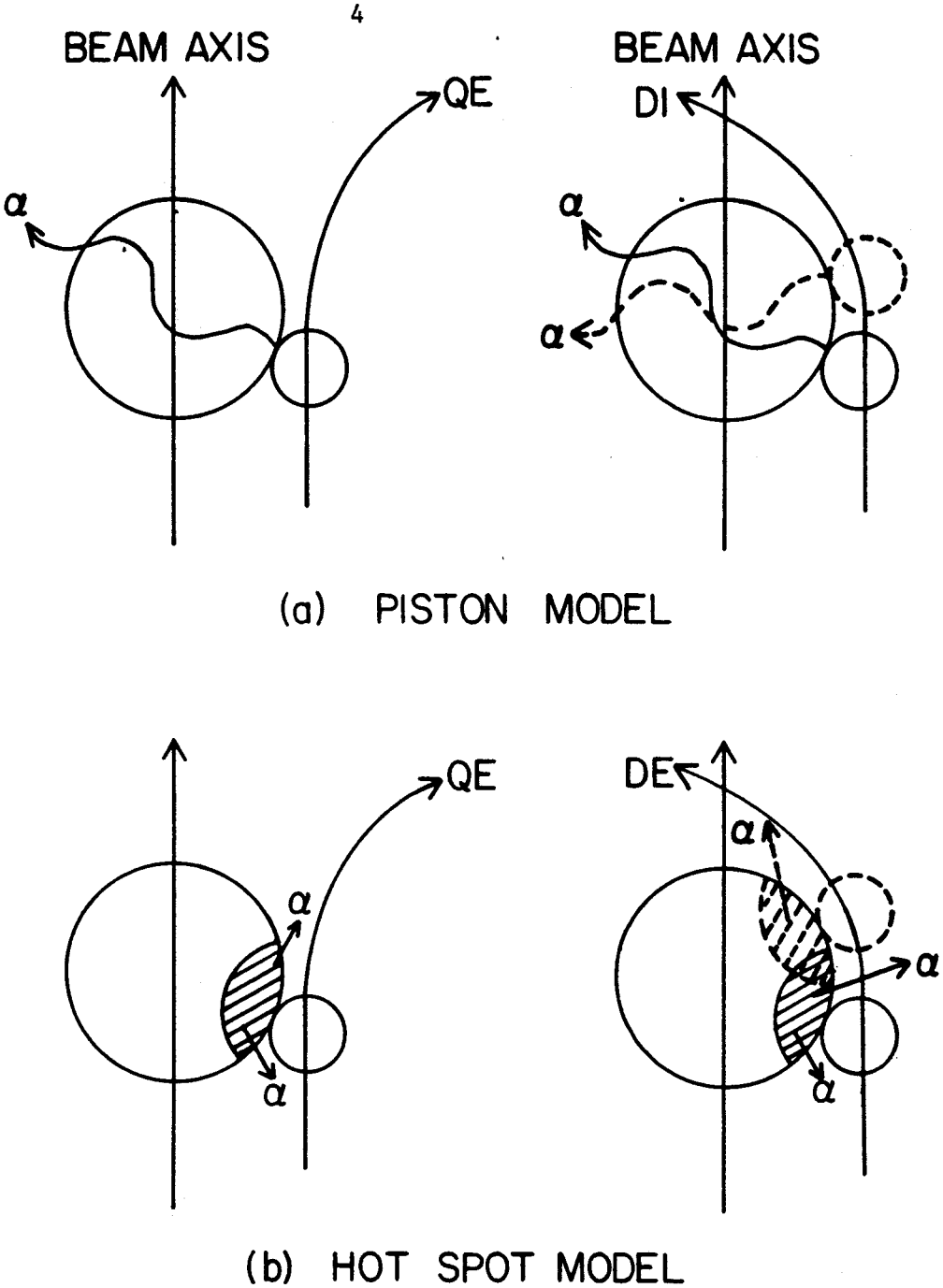

Fig. I-1 Schematic illustration for two pre-equilibrium alpha decay models. a.) Piston model, b.) Hot spot model.

or projectile-like fragment ? This question can be answered provided the reaction proceeds sequentially as follows :

$$T + P \rightarrow X + Y^* \qquad \text{I-1}$$

$$Y^* \rightarrow \alpha + Z \qquad \text{I-2}$$

where T and P are target and projectile respectively; X and Y are the reaction products from a two body reaction. Y^* is excited and it subsequently decays into an alpha particle and Z. Formulation into sequential process has the advantage that the kinematics can be easily calculated once X and Y^* can be identified. If Y is a target-like fragment, then the alpha particles will be expected to be emitted in or near the recoil direction of Y. On the other hand, if Y is the projectile-like fragments, the alpha particles will be detected mainly in a cone around the direction of Y and the heavy ion detector.

3. Pre-equilibrium alpha decay models:

The exact nature of pre-equilibrium alpha decay is not completely understood. Only a few models have been proposed to explain the mechanism for pre-equilibrium alpha emission. The two models which have received quite a lot of attention in the recent literature are the "piston" model and the "hot spot" model.

a. Piston Model : First proposed by Gross and Wilczynski (Gr 77), this process is depicted in Fig. I-1a. Alpha particles induced by the radial component of the dissipative force are emitted in the early stage of collision. The alpha particles go through the nucleus and come out or knock out another alpha particle from the other side from the point of impact. This

mechanism is analogous to the shooting of a BB-gun, hence the name "piston model". When the projectile orbits around the target as shown in the right side of Fig. I-1a, the area of contact between the target and projectile is large. In principle, the alpha particle can originate from any contact point and propagates through the target nucleus. For simplicity only two alpha trajectories are shown. This piston model predicts different projectile-like fragment, alpha particle angular correlations for quasi elastic scattering and deeply inelastic scattering.

b. Hot Spot Model : The model was first proposed by Gottschalk and Westrom (Go 78) in connection with the experiment $^{58}Ni(^{16}O,^{12}C\alpha)$ at 92 MeV by Ho et al. (Ho 77). The incident particle excites a localized part of the target nucleus and causes that part to de-excite by alpha emission as shown in Fig. I-1b. The calculation for this model will be discussed in more detail in Chapter VI. A calculation by Gottschalk and Westrom using this concept predicts that the prompt alpha emission will peak on either side of the direction of the heavy ion detector with a deep valley around it. This valley where the alpha yield is very low is termed the "shadow region". This "shadow region" cannot be seen easily from the pictorial diagram of Fig I-1b. Rather, the existence of the "shadow region" can be understood quite easily in the calculation since the alpha particle is assumed to be absorbed if it comes within the distance of nuclear density of either one of the remaining residual fragments.

In addition to these "pictorial" models, three-body

calculations involving the alpha particle and two residual fragments have been carried out by various groups (Go 78, Ga 78, Ha 78). A more detailed discussion of this type of calculation will be presented in Chapter VI.

C. Experimental Situation

All the pre-equilibrium alpha emission experiments have been performed in the following manner. Coincidence techniques involving two particle identifying detectors were used to obtain angular correlations of the fragments. One of these two detectors is used to identify the heavy fragment X in Equation I-1. This detector is fixed at an angle close to the grazing angle while the other detector detects the alpha particle in coincidence with X. The alpha particle detector normally is moved in the reaction plane defined by the heavy ion detector and the beam direction. In some studies, the alpha detector is also moved in the plane which is perpendicular to the reaction plane. A summary of coincidence experiments in the literature is listed in Table I-1

The angular correlations observed in these experiments do not follow any systematic trend. In one case, $^{197}Au + ^{32}S$ at 373 MeV (Ga 78), the angular correlation is observed to be on the same side of the beam as the heavy ion detector. In another case, $^{58}Ni + ^{11}B$, the angular correlation is observed to peak on the opposite side of the beam as the heavy ion detector (Bh 78). In the case of $^{58}Ni + ^{16}O$, the angular correlation function monotonously increases towards the beam direction. Furthermore,

Table I.1

List of Coincidence Reactions

Reaction	E_{lab}	E_{cm}	E/A	Reference
$^{27}Al + ^{16}O$	65	40.8	4	Present Work
$^{27}Al + ^{16}O$	65	40.8	4	Ha 77a
$^{27}Al + ^{16}O$	88	55.3	5.5	Sa 79
$^{27}Al + ^{16}O$	100	62.8	6.3	Ha 77b
$^{27}Al + ^{14}N$	70	46.1	5	Bi 79
$^{27}Al + ^{14}N$	100	65.9	7.1	Bi 79
$^{58}Ni + ^{16}O$	92	72.1	5.9	Ho 77
$^{58}Ni + ^{16}O$	96	75.2	6	Ho 77
$^{93}Nb + ^{14}N$	90	78.2	7	Sh 77
$^{93}Nb + ^{14}N$	110	95.6	8	Sh 77
$^{12}C + ^{11}B$	116	60.5	10.6	Bh 78
$^{58}Ni + ^{11}B$	116	97.5	10.6	Bh 78
$^{208}Pb + ^{16}O$	140	130	9	Ge 77
$^{208}Pb + ^{16}O$	310	287.9	20	Ge 77
$^{197}Au + ^{16}O$	310	286.7	20	Ge 77
$^{197}Au + ^{32}S$	373	320.9	11.4	Ga 77

the origin of the alpha particle for these types of reactions is also not clear and actually may differ from experiment to experiment. For example, the experimental result for $^{27}Al + ^{16}O$ at 88 MeV (Sa 79) suggests that fragmentation of the projectile is the dominant process while at 65 MeV on the same system, the work of Harris et al. (Ha 77a) suggests that pre-equilibrium alpha decay proceeds sequentially through the break-up of the target-like fragment. In still another experiment, $^{58}Ni + ^{16}O$ by Ho et al. (Ho 77), a "hot spot" model is suggested to explain the mechanism of pre-equilibrium alpha emission.

An understanding of the limitations of all these coincidence experiments is necessary before any conclusion can be drawn from them.

1. The cross-section for the coincidence experiment is very small, thus the statistics are not very good for most measurements. In most experiments, the peak position is deduced from a few points. This is especially true when the peak lies near the beam direction. Elastic scattering of beam particles in the target puts a practical limit as to how close the detector can be placed to the beam. Without data at the forward angles close to the beam direction, any statement about the exact peak position of the angular correlation is only speculative. One exception is the coincidence experiment of $^{197}Au + ^{32}S$. However in this case, a stopper foil was placed in front of the alpha telescope to stop elastically scattered beam particles in the forward angles. One disadvantage of using an absorber foil is the fact that it also

absorbs some of the alpha particles. This presents a problem since an extrapolation of the shape of the alpha energy spectrum is required to account for the absorbed alpha particles. Another exception is the $^{27}Al + ^{16}O$ reaction at 65 MeV studied by Harris et al. (Ha 77a). Results from that experiment show that the C-α angular correlation peaks along the recoil direction of $^{31}P^{*}$, away from the beam direction. This experiment will be discussed in more detail later. The present work contradicts the results of Harris et al.

2. The angular correlation from most coincidence experiments plotted in the center of mass system of Y in Equation I-1 exhibits a strong forward and backward asymmetry. All the results obtained do not rule out a contribution coming from statistical evaporation from the intermediate nucleus Y. In order to understand the contribution of statistical evaporation from the intermediate nucleus Y, backward angle data as well as data from the out-of-plane angular correlation are very important. The data at these angles should reveal the nature of the evaporative component. However, kinematically, the alpha particles that are detected at the backward angles have much lower laboratory energies. Therefore experiments at these backward angles will be affected by the cutoff of low energy alpha particles in the experimental set up. Most of the experiments listed in Table I-1 suffer this problem at backward angles.

3. It was briefly mentioned in Section B-4 of this chapter and later in more detail in Chapter V-B-1 that if the

alpha particles originate from the break up of a projectile-like compound nucleus, the alpha particles are expected to peak in a cone very close to the heavy ion detector. In this case, there is the physical limitation of apparatus setup as to how close one can put the two detectors together.

In conclusion, the results obtained in any coincidence experiments should be viewed with caution. One common feature of the angular correlations of alpha particles and heavy fragments in all the systems studied is that they all tend to peak towards the beam in the laboratory system. The width of the angular correlation is narrow, indicating that the reaction time scale is in the order of 10^{-22} sec, one order of magnitude shorter than the time scale needed for the system to equilibrate.

D. Motivation for the Present Work

The pioneering work of Harris et al. (Ha 77a) on the system of $^{27}Al + ^{16}O$ at 65 MeV suggested that sequential pre-equilibrium alpha emission from $^{31}P^*$ (E_x=14.5 MeV) is the dominant mechanism. The angular correlation data of Harris et al. is plotted in the center of mass system of $^{31}P^*$ in Fig. I-2. Very little alpha particles were observed past 90^o in the center of mass system indicating the absence of an evaporative component. The result of Harris et al was very surprising and interesting at the time when the work was first published. If the observation were true, the properties of and mechanisms in producing pre-equilibrium alphas could be studied with a relatively simple system at low energies.

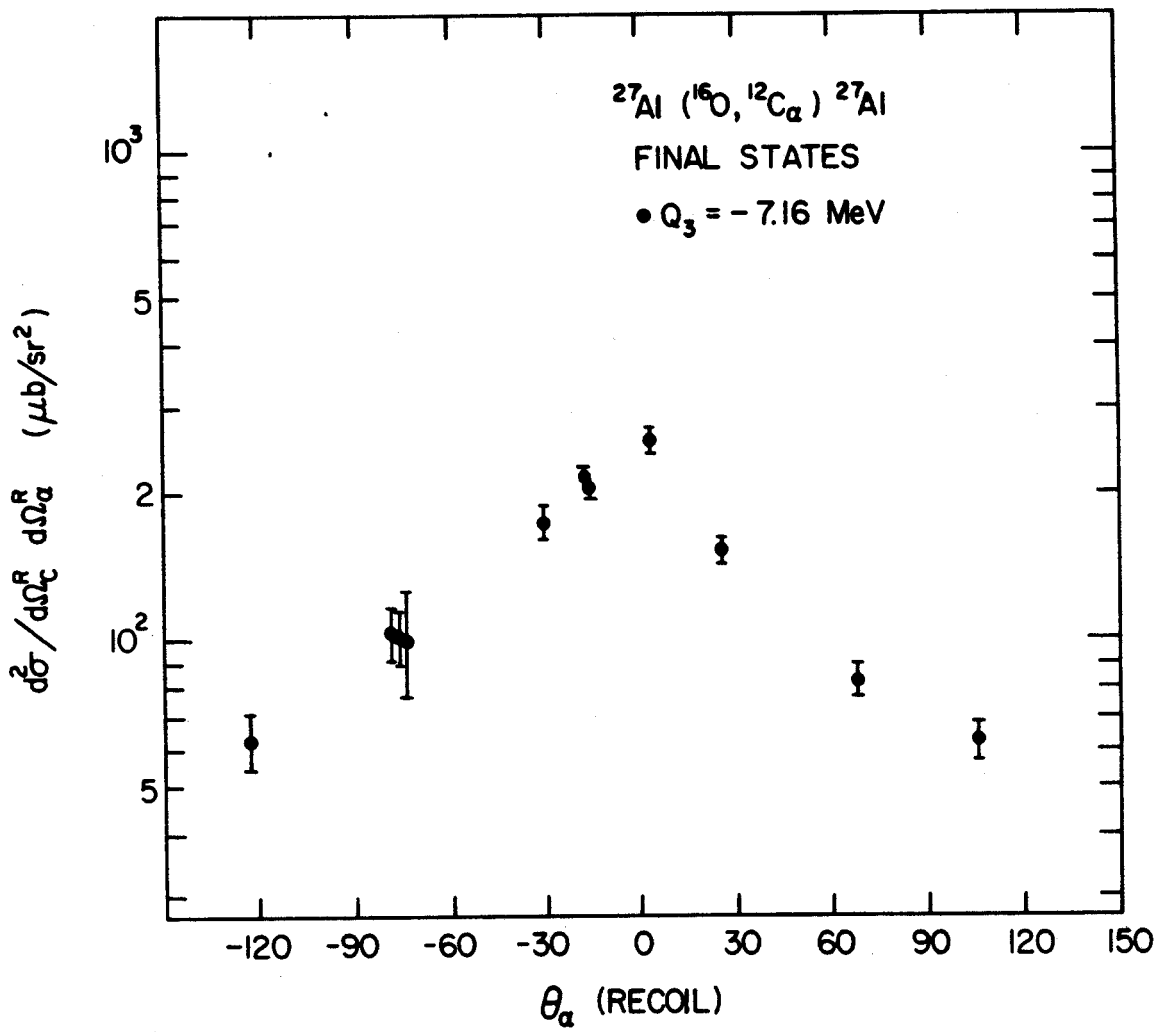

Fig. I-2 Angular correlation function of ^{12}C-α coincidence events as a function of α angle in the ^{31}P*(E_x=14.5 MeV) recoil center of mass system from the work of Harris et al (Ha 77a). The ^{31}P* recoil direction is defined to be 0 degree.

Furthermore, the peaking of the C-α angular correlation on the other side of the beam from the carbon detector suggested orbiting of the carbon particle around the ^{27}Al nucleus. The role of evaporation was neglected for most systems studied at that time. It is very important to know how to extract the evaporation contribution and to compare the pre-equilibrium contribution obtained with the evaporative component. The present work was originally designed to explore the region at backward angles, to better determine the contribution of the evaporation component from $^{31}P^{*}$ and to study the dependence of pre-equilibrium alpha decay as a function of the heavy ion detector angle

This work was carried out with 65 MeV ^{16}O which corresponds to about 4 MeV per nucleon. The bombarding energy is lower than the energies used in most experiments listed in Table I-1. However, all available evidence indicates that measurements of the pre-equilibrium alpha decay process at low energy is qualitatively quite similar to measurements at higher energy. One advantage the low energy experiment should have over the higher energy experiments is the hope that with less excitation energy available, the reaction mechanism can be understood better without interference from other complicated processes.

65 MeV ^{16}O is well within the operating range of the FN tandem linear accelerator in the Nuclear Physics Laboratory of University of Washington. The availability of beam time allows careful and in depth study of the present system. This is especially important since the cross-section for the coincident

experiment of this type is very small, about 100 $\mu b/sr^2$.

In Chapter II, the experimental methods used in the present work are described. On line data acquisition and off line data analysis are discussed in Chapter III. Different schemes of presenting the data are discussed in Chapter IV. In Chapter V experimental results from the present work are presented and contributions to the data from different reaction mechanisms are sorted out. A dynamical three-body trajectory program has been written to understand pre-equilibrium alpha emission and is discussed in Chapter VI. Finally a few suggestions to further improve this system is given in Chapter VII. This last chapter also contains conclusions about this work as well as about this type of coincidence experiment in general.

CHAPTER II

EXPERIMENTAL PROCEDURE AND APPARATUS

A. Experimental Approaches

Two different experimental methods were used in the present work. The first system involved two traditional DE-E telescopes detecting carbon and alpha particles in coincidence. The second system used an array of single detectors to detect alpha particles in coincidence with a DE-E telescope that identifies carbon particles. These two methods are described in detail below.

1 Two-Telescopes Method:

Both carbon and alpha particles are detected in coincidence using two telescope counters. This is a standard technique. (Ha 77a, Ge 77, Ho 77, Sh 78, Ga 78 Bi 79). Extensive discussion of particle identification with telescope counters can be found in various articles (Go 75, En 74). Basically, this method utilizes the fact that particles with a given energy but with different masses and charges lose different amounts of energy passing through a thin detector (DE) The particles eventually stop in another detector (E) mounted directly behind the DE counter. Thus, total energy of the particle is given by the sum of energy deposited in DE and E detectors. Empirically, over a limited range of energies, the relation between range (R) and energy of a particular particle (E) is given by a simple power law.

$$R = aE_{tot}^{n}$$

$$a = k(Mq_{eff})^{-1} \qquad \text{II-1}$$

where R is the total thickness of detectors needed to stop the particle ; E_{tot} is the total energy of particle ; n is an empirical parameter ; q_{eff} is the effective charge ; M is the mass of the particles and k is a constant.

This method of identification can be understood more clearly by looking at the following diagram.

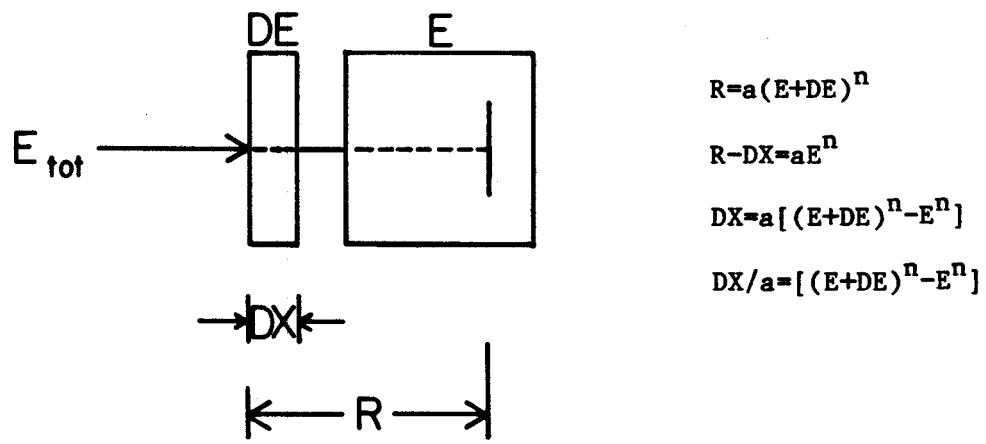

Fig II-1 Schematic diagram showing the mathematical relationship used to obtain the particle identification in a DE-E counter telescope.

DX in the diagram is the thickness of the DE counter and DX/a is defined as the particle identification (PID) function. For fixed DX, the PID function is proportional to the product M x q_{eff}. Ideally it should be independent of the particle energy. In all the experimental runs, n is found empirically to

be 1 73 for alpha particles. For carbon particles, $(E+1.7DE)^{1.69}-E^{1.69}$ gives the best PID function.

This two-telescopes system suffers the following disadvantages:

i. Kinematically, the alpha particles detected in the forward angles have much higher energy than those detected in the backward angles. Typically, the alpha particles detected vary in energy between 0 to 25 MeV. In the particle identification method, a fixed DE only gives optimum PID resolution over a limited range of energy. An 8.7μ DE counter was used with a 300μ E detector to detect alpha particles in the forward angles. Alpha particles with 2 MeV or less energy will be stopped in the 8.7μ DE counter. In order to increase the efficiencies of collecting low energy alpha particles at backward angles, the thinnest DE counter available (5μ) was used. Even so, the finite thickness of the DE detector stops very low energy alpha particles at and below .5 MeV Experimentally, due to detector noise and discriminator level of the electronic system, the lowest alpha energy detected was higher than that dictated by the thickness of the alpha DE detector.

ii. The multiparameter on-line data acquisition program RALPH (Chapter III-B) only accommodates four parameters in coincidence. However the two-telescopes systems require five parameters, namely carbon DE input (DEC), carbon E input (EC) alpha DE input (DEα), alpha E input (Eα) and the time difference (TAC) between events in the two telescope counters. The TAC

spectrum is needed to subtract the contribution of random coincidence events from the data. Ideally all these five parameters should be stored in the computer. In order to meet the limitations of RALPH, the electronic system was designed so that the TAC spectrum was recorded off line and two hardware gates corresponding to the peak region and a flat region of the TAC spectrum were used to separate "real" coincidence events from "random" coincidence events before they were recorded by the computer. A more detailed description is given in Chapter III-A-1.

2 Time-of-Flight (TOF) Method:

The above shortcomings were eliminated by taking data using a single counter instead of a telescope to detect alpha particles. A very simple relationship $E=.5mv^2$ relates the velocity of a particle to its mass and energy. Rearranging the terms and dimensions gives the following formula relating the flight time of the particle and its mass

$$T = (MD^2/2E)^{1/2} \qquad \text{II-2}$$

where T is the time of flight in ns ; D is the distance (flight path) in cm ; E is the energy in MeV and M is the mass in amu.

Equation II-2 can also be rearranged to yield M in terms of E and T for D fixed. In that case, M is proportional to ET^2 Experimentally, D is given by the detector distance to the target. Energy is detected in the detector. T, however, is not directly measurable. What is measured is the time difference (T_{diff})

between arrival of a carbon particle in the carbon telescope (T_c) and the arrival of a coincident event in the alpha detector (T')

$$T_{diff}=T_c-T' \qquad \text{II-3}$$

Ideally if the carbon particles can be detected right after the reaction in the target i.e. $T_c=0$, this would give a measure of the starting time for the alpha particles flight time. To simplify the following arguments, the energy of the carbon particles , hence T_c, is assumed to be fixed. From Equations II-2 and II-3, at a constant energy, the timing resolution (DT) required to separate an alpha particle from another particle X is given by the following equation :

$$DT = (D^2/2E)^{1/2}[(m)^{1/2} - (m_x)^{1/2}] \qquad \text{II-4}$$

There are two cases needed to be considered :

i. X is heavier than alpha : Experimentally, the majority of the heavy ions detected in the alpha detectors in coincidence with carbon particles detected in the carbon telescope have energies less than 12 MeV. Furthermore, the mass of these heavy ions is greater than 10. As the minimum DT is given by the maximum E, the worst case would be when E=12 MeV, M_x=10. Equation II-3 gives DT to be 4.7 ns.

ii. X is lighter than alpha : Experimentally, protons are the only particles detected in coincidence with carbon particles that are lighter than alphas. The alpha particles of interest have energy less than 25 MeV. With this knowledge, the

alpha detectors were chosen to be 300μ thick so that protons with more than 6 MeV of energy will pass through and the energy deposited in the detector will be less than 6 MeV. These high energy protons cannot be confused with alphas or other particles as seen in Fig. II-2. For 6 MeV alphas and protons, DT computed from Equation II-3 is greater than 5.7 ns. A two dimensional plot of E vs T for protons, alphas and ^{16}O is shown in Fig. II-2.

From the above analysis, the timing resolution needed to distinguish alpha particles from all other particles is of the order of 5 ns and can be achieved easily. One other complication comes from the fact that the carbon energy is not fixed. Thus the simplification that T_c is constant which was introduced earlier is not valid. The carbon particles of interest typically have energies between 30 to 60 MeV. As the carbon telescope is placed ~ 7.6 cm from the target during the experiment, it takes from 3.4 to 2.4 ns for the carbon particles to reach the carbon telescope counter. This uncertainty of 1 ns is negligible when compared to the 5 ns timing resolution required to separate alpha particles from other particles. The only effect it introduces is to broaden out the TAC peak.

With this method, up to four single detectors located at four different alpha laboratory angles can be used in coincidence with one carbon telescope. This arrangement allows more than one alpha angle to be measured at once. This is of tremendous advantage to this type of coincidence experiment since the cross sections are very small and it takes a long time to collect

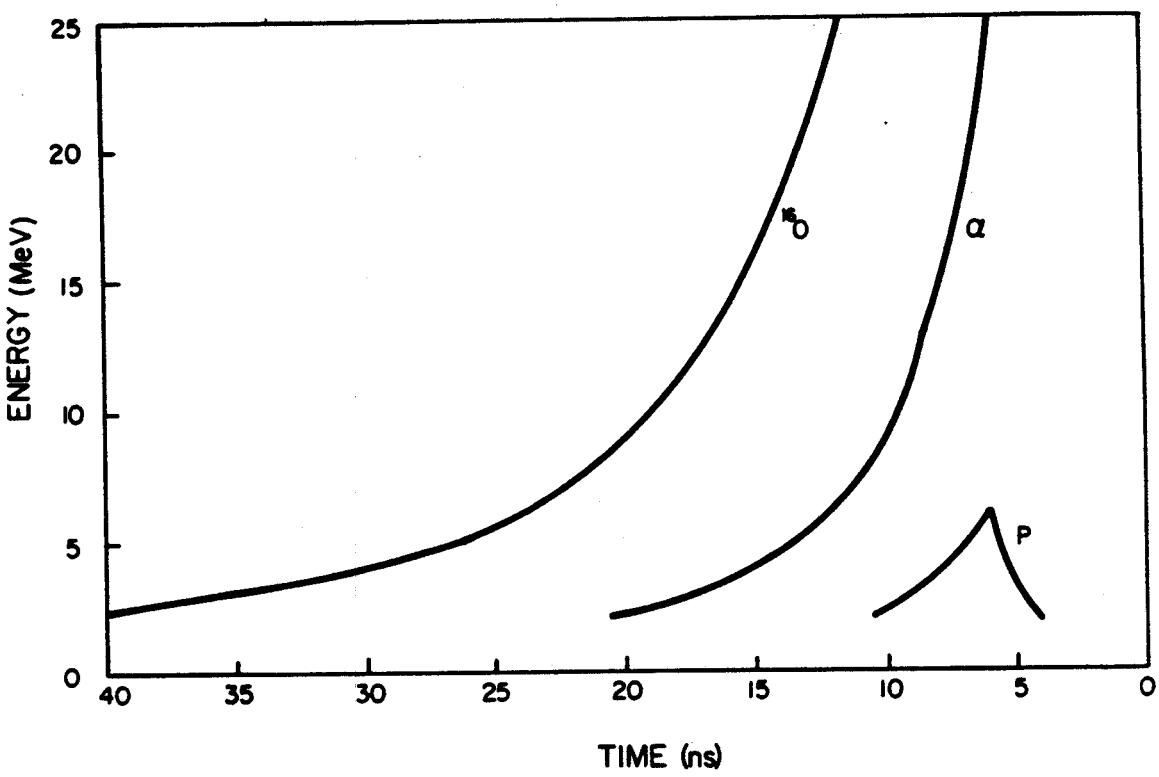

Fig. II-2 Energy versus time plot for proton, alpha and ^{16}O.

statistically significant data.

B. Accelerator And Ion Sources

The two-stage Tandem in the Nuclear Physics Laboratory of University of Washington is equipped with a Direct Extraction Ion Source (DEIS) and a sputter source (UNIS) to produce various heavy ions. The accelerator and beam transport system have been described in detail by Weitkamp (We 74). The 65 MeV ^{16}O beam used throughout the experiment was produced by extracting OH^- ions from the DEIS after water vapor was bled into the duoplasmatron. Production and acceleration of the oxygen beam has been discussed by Webb (We 77). The ^{12}C beam used to calibrate the carbon telescope is produced by sputtering Cs onto a carbon cone. The operation and modification of the sputter source has been discussed by Roth (Ro 75,76).

C. Detector Array

All the detectors used were commercially available totally depleted transmission and partially depleted surface barrier detectors. Throughout the experiment, three DE counters (14.7μ, 17.3μ, and 20μ) were used during different runs in the carbon telescope. The carbon E detector was a partially depleted 300μ detector. The carbon telescope counter typically had a solid angle of 5 to 10 msr. In the two-telescopes method, due to different alpha energies in the forward and backward angles, two telescope counters were used: an 8.7μ-300μ (DE-E) for the forward

angles and a 5μ-300μ for the backward angles. The alpha telescope at the forward angle subtended a solid angle of about 1.3 msr. At backward angles, without large number of elastic scattered particles, the solid angle for the alpha telescope was as large as 5 msr. All the alpha detectors were transmission surface barrier detectors, 250μ to 300μ thick. In order to provide a sufficient flight path for the alpha particles to be identified, the alpha detectors were placed ~20 cm from the target. Thus, to compensate for the loss of solid angles, the detector areas had to be as big as possible, typically 300 to 450 mm^2. The aperture sizes varied from 10 mm in diameter for the forward angle detectors to 22 mm in diameter for the alpha detectors at back angles. All the detectors were thermo-electrically cooled to 0^oC to suppress noise and leakage current of the counters. When the detectors were cooled, they also gave better timing signals. Area defining circular tantalum apertures, mounted directly in front of the detectors, were covered with 98 $\mu g/cm^2$ Ni foils to avoid condensation of pump oil onto the detector surface. These foils plus small magnets placed in front of the detectors protected the detectors from low energy electrons produced by the beam on the target.

D. Calibration of Detectors

As most of the carbon particles detected have energies between 30 and 60 MeV the carbon telescope was calibrated with 30, 44, and 60 MeV ^{12}C beams produced by the sputter source

scattered off a 180 $\mu g/cm^2$ Au target. The alpha telescope and the single detectors array were calibrated with an ^{241}Am source which produces 5.5 MeV alpha particles and a ^{212}Po source which produces 8.78 MeV alpha particles.

E. Targets

1. Preparation:

The targets used in most of the experimental runs were prepared by evaporating 99.999% pure ^{27}Al wire from a special intermetallic boat (resistivity: 1000-2000 $\mu\Omega$) onto a glass slide coated with teepol as parting agent. As oxygen reacts with aluminum readily to form an oxide layer, special care had to be taken in reducing the amount of oxygen contaminant present in the target. The evaporation took place in a high vacuum ($5x10^{-7}$ torr). Also, during the evaporation, the glass slides rested on a copper plate which was continuously cooled by water. Afterwards, the slides were stored in Ar gas until ready to use. Even with these precautions, formation of a thin layer of Al_2O_3 on the surface of the ^{27}Al target cannot be avoided (Ma 63).

2. Contaminants and Carbon Build-up :

The oxygen and carbon contents in these targets were determined by backward angle scattering of 3 MeV protons (Sh 51, Re 56). The oxygen contaminant was assumed to be in the form of Al_2O_3. These contaminants (carbon and oxygen) were shown to be present originally in less than 1% atomic abundance. Back-streaming of mechanical pump oil into the scattering chamber

during the experiment caused a layer of carbon to be formed on the part of the target hit by the beam The C(^{16}O,Cx) events are kinematically separated from the ^{27}Al(^{16}O,Cx) events with Q=-7.16 MeV at the angles measured in this experiment. The effect of carbon build-up was studied by bombarding a 370μg/cm^2 carbon target. The total energy spectrum for events from both the ^{nat}C(^{16}O,Cx) and ^{27}Al(^{16}O,Cx) reactions at θ_c=-30^o are shown in Fig II-3 While only an upper limit of carbon buildup could be measured by determining the amount of carbon in the target at the end of the experiment, nevertheless it was determined that in the region of the peak corresponding to the ^{27}Al(^{16}O,Cx) reaction leaving ^{12}C in it ground state, the contribution from carbon build up contamination was negligible. The carbon build-up was greatly reduced by improving the pumping system in the scattering chamber described in the next section.

F. Scattering Chamber Set Up

All measurements were done in the 61 cm chamber in Cave II. This chamber is electrically insulated from local ground. All the power supplies and cables are grounded in the counting room area thus reducing ground loops. The chamber is equipped with a mechanical pump for roughing the chamber and a diffusion pump for high vacuum. A liquid nitrogen cold trap separates the diffusion pump from the chamber. In an effort to reduce carbon build-up on the target due to back streaming of pump oil from the mechanical pump, a VEECO coaxial trap which traps oil without collecting

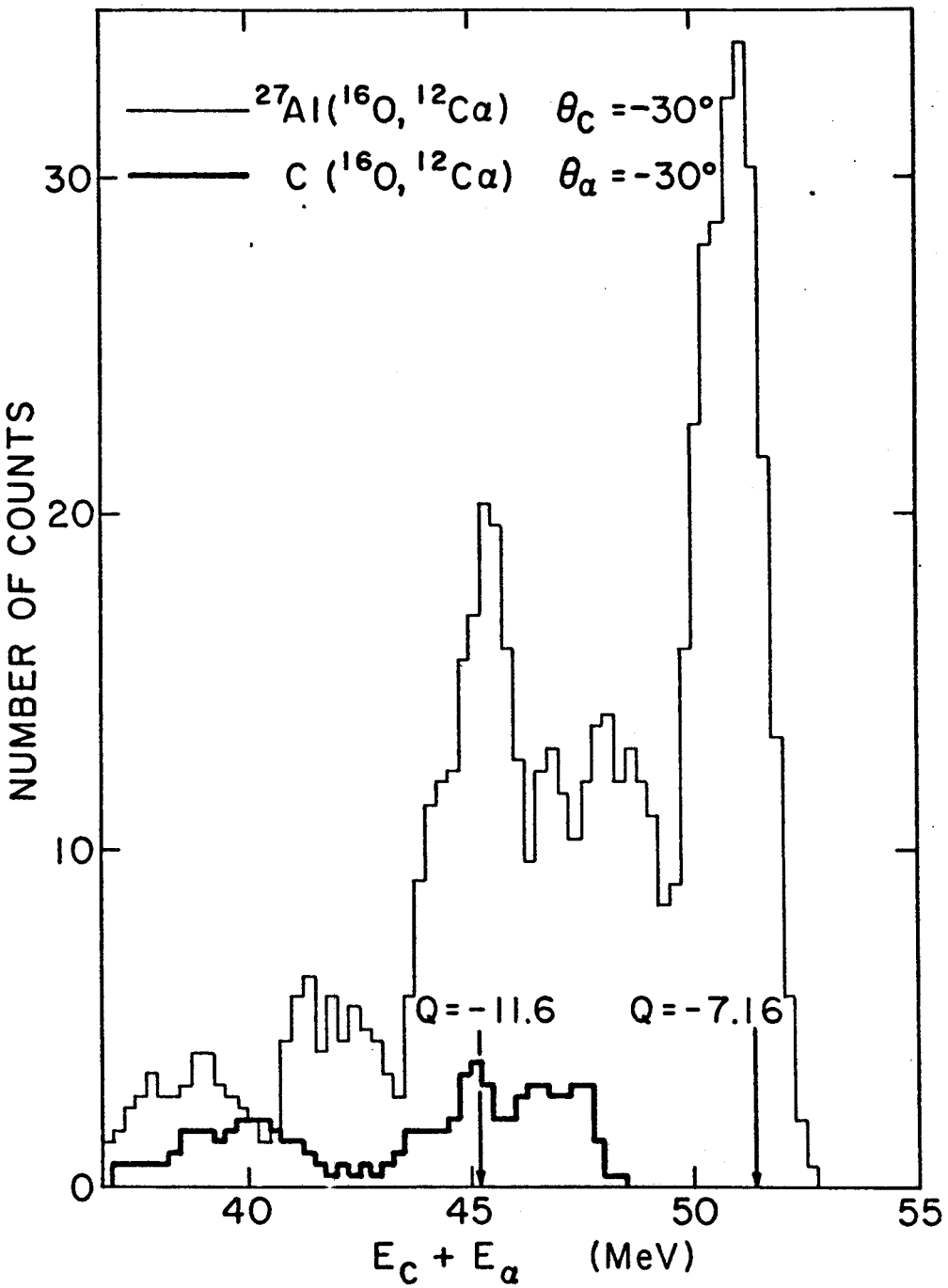

Fig. II-3 Total energy spectrum of $^{nat}C(^{16}O\ ^{12}C\alpha)$ and $^{27}Al(^{16}O,^{12}C\alpha)$ at $\theta_\alpha = -30°$, $\theta_c = -30°$. Both spectra are normalized with same amount of beam current. The $^{nat}C(^{16}O,^{12}C\alpha)$ energy spectrum is also normalized to the maximum amount of C build-up on the target determined at the end of the experiment.

water vapor was installed between the mechanical pump and the chamber. In addition, a small liquid nitrogen cold trap with a copper tubing attachment surrounding the target was also used during the experiment. An integral collimator box is located directly upstream from the chamber. Tantalum apertures, 5.6 mm and 4 0 mm in diameter were placed in the box 40.6 mm and 55.9 mm from the target respectively. The faraday cup is located about 1 meter downstream from the beam exit port of the chamber.

1. In-Plane Set up :

The chamber set up for the in-plane C-α angular correlation measurement is shown in Fig. II-4. The scattering chamber is equipped with two movable arms that can be rotated 360^{o} by a remote control device and positioned to an accuracy of $.1^{o}$. The carbon telescope was mounted on the upper arm fixed at θ_c(θ_c=-30^{o} or -40^{o}) while the alpha telescope or detector array was mounted on the lower arm. A target ladder with four target positions was mounted from the top of the chamber lid. The beam is focused through an aperture of 3.2mm diameter mounted in one of the target positions.

2. Out-of-Plane Set Up :

The scattering chamber does not have a movable out-of-plane arm. A simple modification of the in-plane array was used to measure the out-of-plane C-α angular correlation. Instead of being mounted parallel to the chamber floor, the alpha-detector array was mounted on the lower arm perpendicular to the chamber floor. However, due to the size of the chamber the array could

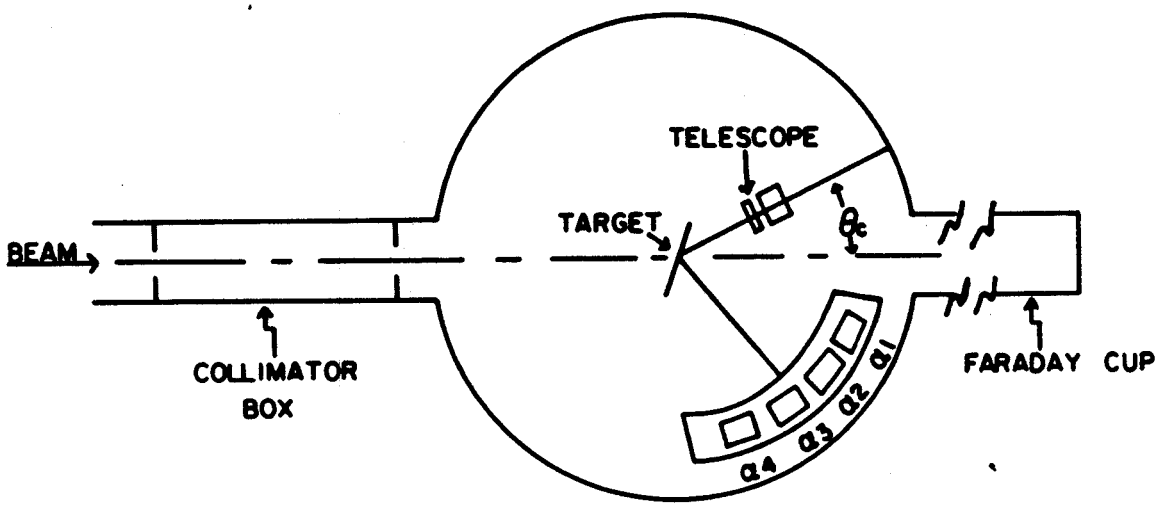

Fig. II-4 Top view of the in-plane experimental set-up

only span 60^{o} out of plane. Three alpha detectors were fixed at $\phi_{\alpha}=0^{o}$, 30^{o}, and 60^{o}. The fourth detector was mounted in the center of the chamber top. The whole arrangement is illustrated in Fig II-5. An ^{27}Al target was clamped down by the target holder in the target position. The target can be rotated 360^{o} in plane by a remotely controlled device and was manually rotated to 30^{o} out of plane.

Both the in-plane and out-of-plane set up also included a monitor counter situated out of plane at a polar angle of 30^{o}.

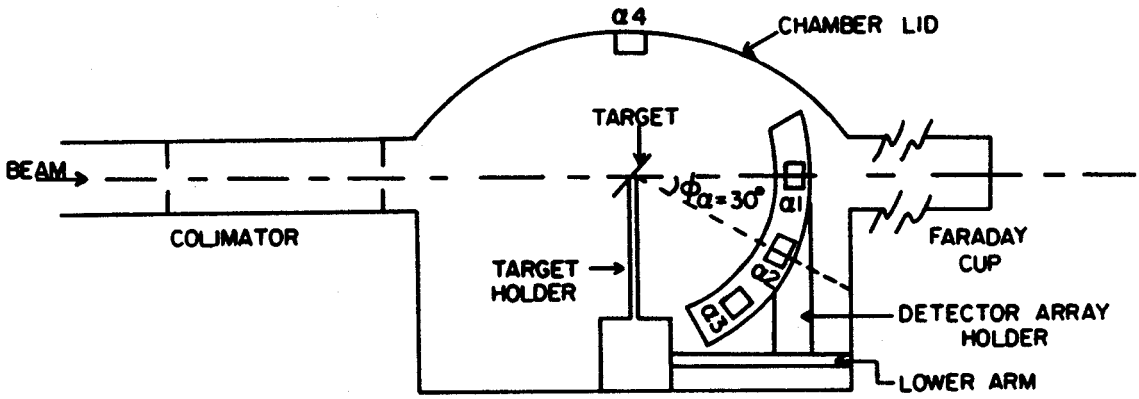

Fig. II-5 Side view of the out-of-plane α detector array.

CHAPTER III

ELECTRONICS AND COMPUTER PROGRAMS

A. Electronics

Most of the electronic modules including the power supply bins were commercially bought. The particle identification system used conventional coincidence circuits. In order to minimize high frequency pickup on the fast timing signals from the detector preamps, all the fast electronics were placed with the preamps next to the scattering chamber. The other electronics were located in the counting room area.

1. Two-Telescopes Method:

The electronic system used in the two-telescopes method is shown in Fig. III-1. The following considerations were taken into account in designing the electronic system.

i Two types of events were collected during the experiment, namely the single events detected by both the carbon DE and E counters (2-fold coincidence events) and the events that were detected by both the carbon and alpha telescopes (4-fold coincidence events). The mechanism by which the computer processes an event is illustrated on the right side of the dashed line in Fig. III-1. A bit is set in the format register of the interface for each analog to digital converter (ADC) for which a gate signal is received. The event occur interrupt signals the computer to process an incoming coincidence event. The computer

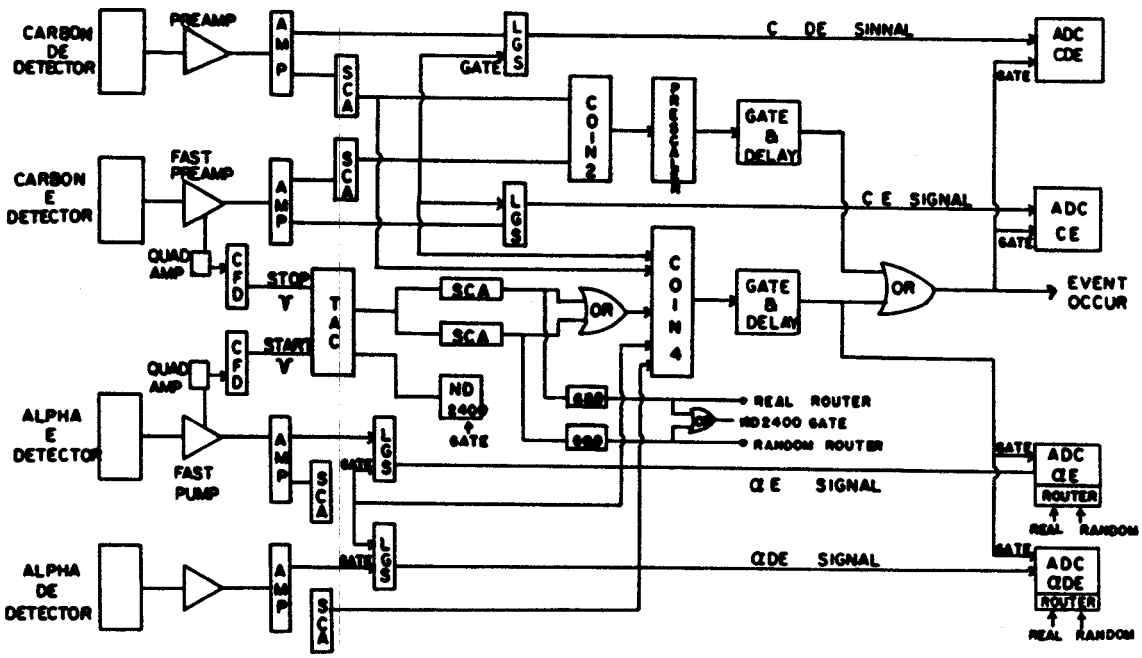

Fig. III-1 Schematic diagram of electronic system used in the two-telescope method

then interrogates the format registers. If all the ADC format registers are set, the event will be treated as a 4-fold coincidence events. If only the carbon DE and E ADC's receive the gate signals, the event will be treated as a 2-fold coincidence events. If neither conditions is satisfied, it will be counted as a non-valid event. After each event is processed, all the format registers and the event-occur interrupt will be cleared until the next event comes.

ii. There were many more 2-fold coincidence events than 4-fold coincidence events. As the computer processes the coincidence event relatively slowly, in order to reduce dead time of the carbon DE and E ADC's, a prescaler was introduced to cut down the counting rate of the carbon telescope single events by a factor of 100.

iii. A time-to-amplitude converter (TAC) was used to measure the time difference between the arrival of an event in the carbon telescope and the arrival of a coincidence event in the alpha telescope. In all the experimental runs, the TAC had a time range of 400 ns i.e. any events that came within 400 ns after the TAC registered a start signal would be considered as coincidence events. Depending on the counting rate of the alpha telescope in forward or backward angles, signals from the alpha telescope can be used either as the stop or start pulse for the TAC. The data collected consisted of both real as well as random events. The TAC spectrum is needed to subtract the contribution of random coincidence events from the data. Due to limitation of the

on-line data taking program RALPH, the TAC spectrum had to be recorded off line with a multichannel analyser (ND2400). The TAC output was sent through two single channel analysers (SCA) in parallel. The upper and lower level of one SCA corresponds to the peak region of the TAC spectrum ("real" window) and the other SCA has an upper and lower window corresponding to the flat region of the TAC spectrum ("random" window). The "random" window is typically five times longer than the "real" window. These SCA outputs generated the routing signals for the computer so that each alpha DE and E spectrum contained two energy spectra corresponding to the "real" and "random" parts of the TAC.

Signals from each of the detector were amplified with a preamp and a standard linear amplifier. The prompt bipolar signal from each of the amplifiers was then sent to a single channel analyser which gave a 10 volt high, .5 μsec wide output pulse. These output logic signals were then used in the coincidence units (COIN2 and COIN4) and for timing and gating purposes. The delayed unipolar pulse from the each of the amplifier passed through a linear gate stretcher before entering the ADC

2. Time-of-flight Method :

Fig III-2 shows the schematic electronic diagram used in the time of flight method. This electronic system was similar to the system used in the two-telescopes method with the exception that the alpha detector array replaced both the alpha DE and E needed for the telescope. As the TAC spectrum was recorded on line, all the electronics needed to generate the "real" and

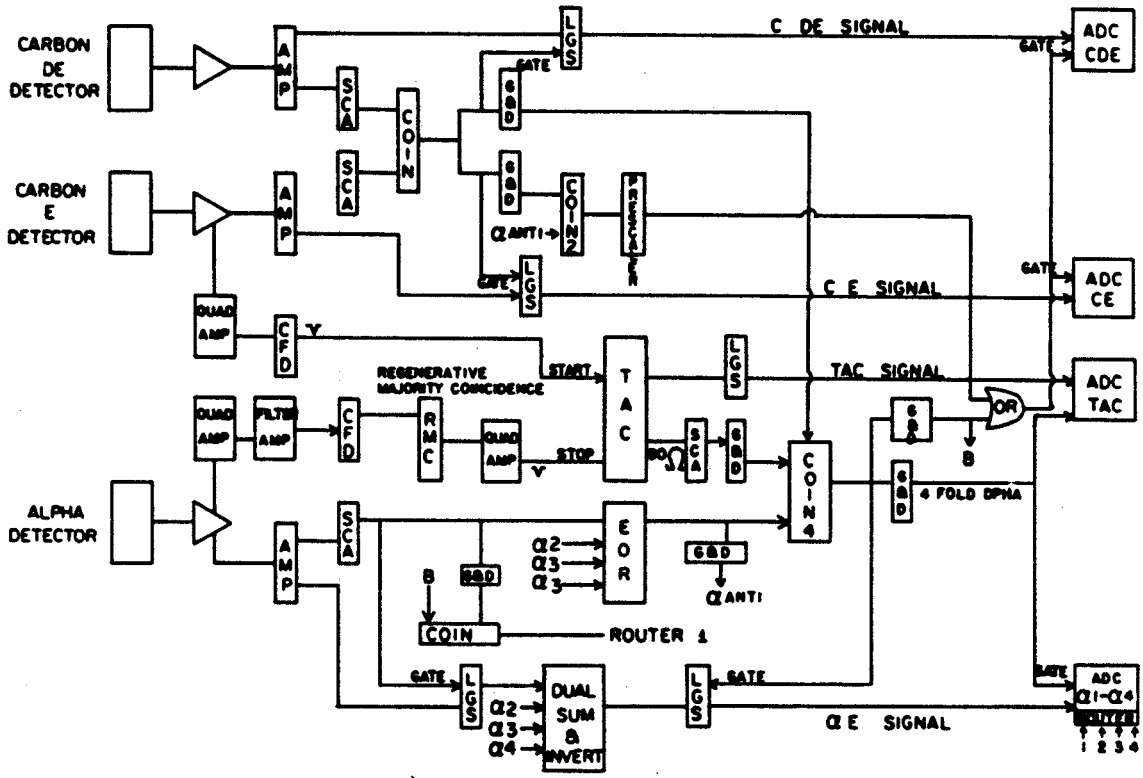

Fig. III-2 Schematic diagram of electronic system used in the time-of-flight method.

"random" routers were eliminated. Since all four alpha detectors in the array were routed into one ADC and one TAC the electronics were more complicated and are described in the following paragraph.

Signals from any of the four alpha detectors were first amplified by a preamp. The timing output from the preamp was subsequently amplified by a quad amplifier and a filter amplifier. The amplified output was then sent to a constant fraction discriminator (CFD). The sharp negative pulse from the CFD was sent to a regenerative majority coincidence box (RMC) which was adjusted to accept single events and thus functioned as an OR unit. The output signal of the RMC was very much reduced and had to be amplified by a quad amp stage before it could be sent through a delay line to the stop input for the TAC. The energy output signal of the preamp was sent to a standard linear amplifier. In order to handle high counting rates, especially at forward angles, all the alpha amplifiers operated with a time constant of .25 μsec. The bipolar outputs of the amplifiers were sent to SCA's to generate logic pulse for timing and gating purposes. The delayed unipolar output of the amplifier went to a linear gate stretcher. The linear output was then sent to a dual sum and invert (DSI) module which is a linear pulse adder. There was always a possibility that undesired outputs of the DSI came from addition of accidental coincidence pulses from different detectors in the DSI. These outputs were eliminated by requiring that a logic output from the SCA of each alpha detector go through

a common exclusive or (EOR) unit. The gating signal for the alpha ADC was generated in the 4-fold coincidence unit (COIN4) requiring simultaneous presence of the EOR output , TAC signal and output from the coincidence of carbon DE and E SCA's. The router signal for each detector was generated by requiring coincidence between the logic signal from the corresponding SCA and the COIN4 outputs. Since the time of flight system had no DE detector to range out those low energy heavy ions at forward angles, many more signals were generated in the alpha system. In order to further eliminate pileup at the alpha ADC, the linear outputs from the DSI were gated by the COIN4 output before they were sent to the ADC. All these complicated systems for gating out undesired signals were necessary to reduce the dead time in the electronic system, the ADC's, and the computer.

B. On-line Data Acquisition Program

All the data collection was done with the SDS 930 computer using the program RALPH (Sa 77) RALPH is a four parameter, multi-coincidence program. In the two-telescopes method, the four parameters are carbon DE (CDE), carbon E (CE), alpha DE (αDE) and alpha E (αE). In the case of time of flight system, the αDE parameter was replaced by the TAC. Two types of events were collected, the 4-fold and 2-fold (carbon singles) coincidence events. Section A-1 of this chapter explains how the an incoming event is distinguished to be a 4-fold coincidence, a 2-fold coincidence or a non-valid event.

Aside from the four original parameters which correspond to the data collected by the four ADC's, RALPH allows creation of pseudo parameters or functions. Each pseudo parameter is actually an algebraic function of one or more of the original parameters or previously defined functions. The following functions were created during this experiment : total energy of the carbon telescope (CTOT) and the PID function of the carbon telescope (CPID).

$$CTOT = CE + CDE/DIV$$

where CE is the carbon E; CDE is the carbon DE and DIV is the an input constant that accounts for the difference in the carbon DE and E detector amplifiers gains.

$$CPID = (CTOT^n - CE^n)/MUL$$

where n is the empirical exponent of the PID function defined in Equation II-1 and MUL is the compression factor.

Both CTOT and CPID functions were built into the RALPH program. The program user has to specify the parameters used e.g. CDE, CE and input the constants DIV n, and MUL when setting up RALPH for data collection. Since all these functions have to be computed for each event during data collection, all multiplication and division are accomplished by binary bit shifting in order to speed up the computation. Thus, the input constants DIV and MUL have to be integral powers of 2. A table of the form I_{ch}^n where I_{ch} corresponds to channel number was created ahead of time and stored in the upper 16K memory of the computer. The CPID is calculated with the aid of this table.

Spectra corresponding to data collected by each of the ADC's are called raw spectra. In addition to these, RALPH also allows additional spectra called gated spectra to be created. These gated spectra can be one or two dimensional plots whose axes are the original parameters or previously defined pseudo parameters. One important feature of the gated spectra is that conditions i.e. digital windows corresponding to a certain part of a raw spectrum or another previously defined function, can be used to establish the gating conditions. Only events that satisfy the conditions will be accumulated in the corresponding gated spectrum.

Before the actual data collection took place, the functions CPID and CTOT were created. A gated spectrum with no conditions was defined to be the CPID function and displayed. A typical CPID spectrum produced by RALPH is shown in Fig. III-3. Based on the information from the CPID spectrum, a pair of digital windows corresponding to the carbon particles detected by the carbon telescope is obtained.

For the two-telescopes system, a second two-dimensional (2D) array was defined with horizontal and vertical axes to be DE and E parameters of the alpha telescope respectively. A constraint corresponding to the digital windows obtained from the CPID function was placed on all the events that would be accumulated in this 2D array. Thus, this spectrum only contained events that were coincidence with the carbon events detected in the carbon telescope. Due to limitation of storage space, the 2D

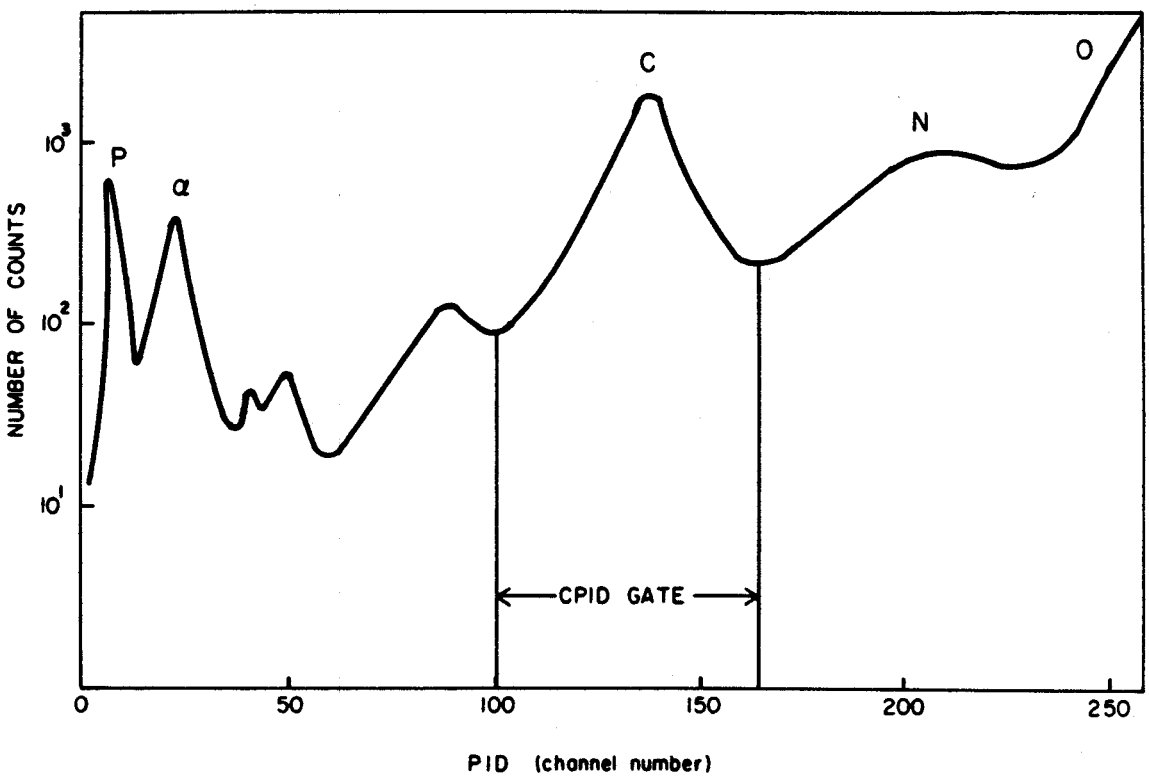

Fig. III-3 Example of PID spectrum of the C-telescope obtained on-line with the data acquisition program RALPH.

arrays produced by RALPH are limited to 32X32 and only provided some glimpses of the data being collected. A more detailed analysis of the data had to be done off-line. A 2D array that accompanies the CPID spectra of Fig. III-3 is shown in Fig. III-4. In the time of flight system αE vs. TAC for a particular alpha detector was plotted as shown in Fig. III-5.

RALPH has another completely independent parameter which collected the monitor spectrum. During data collection, only the 2-fold and 4-fold coincidence data were accumulated event by event in a buffer. When the buffer was full, the data were dumped onto a magnetic tape for off-line analysis at a later time All the accumulated raw and gated spectra were displayed "live" on a cathode ray tube (CRT) display. These spectra were dumped periodically onto the magnetic tape.

C. Off-Line Data Analysis Program

1. EDNA :

Most of the off-line data analysis was done with a twin SDS 930 computer. This computer is very similar to the on-line SDS computer except it does not have the CRT display nor an upper 16K memory. However, a disk with 512K words storage space is attached to it. The program EDNA (Sa 77) was written specifically to analyse the data produced by RALPH.

During each experimental run, an enormous amount of data was collected. However, only a tiny fraction of these data consisted of the carbon alpha coincidence events with the

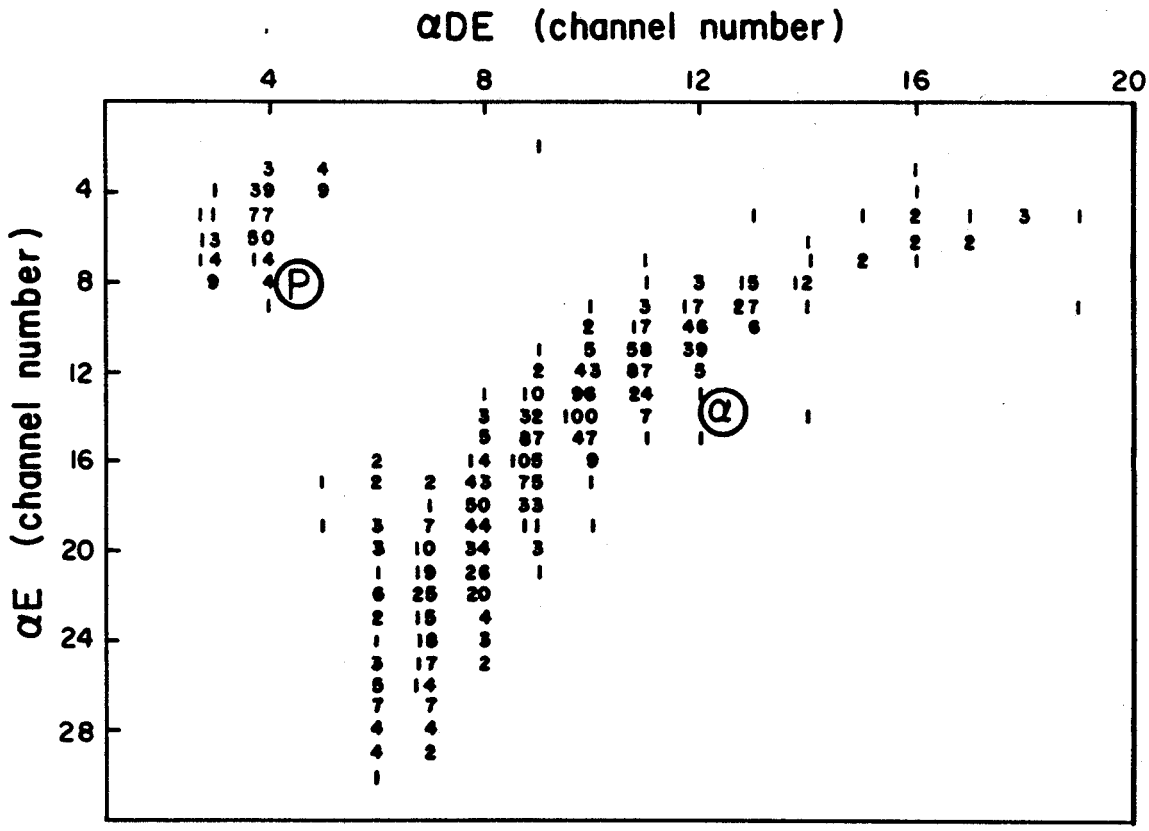

Fig III-4 Example of αE vs. αDE two dimensional plot obtained with RALPH in the two-telescope method.

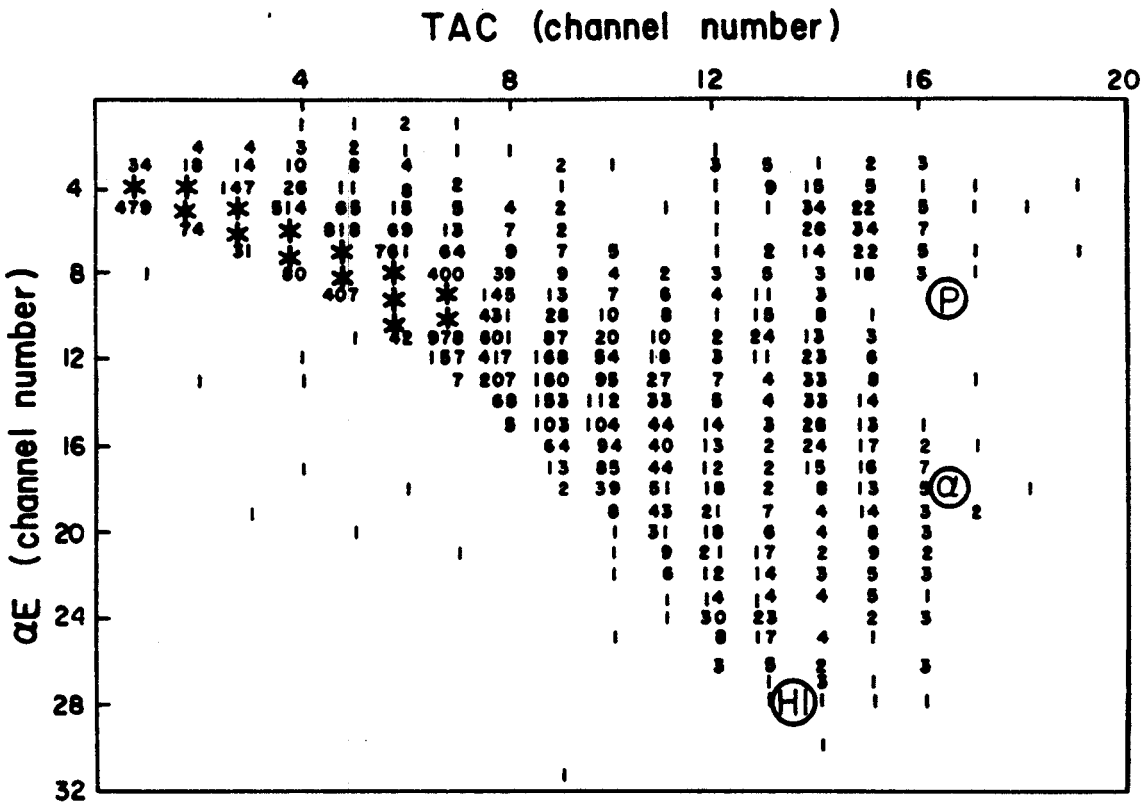

Fig III-5 Example of αE vs. TAC two dimensional plot obtained with RALPH in the time-of-flight method.

appropriate Q values of the reaction $^{27}Al + ^{16}O \rightarrow ^{12}C + \alpha + ^{27}Al$. One function of EDNA was to sort through the raw data with various conditions i.e. digital windows as used in RALPH, in order to extract the events of interest. In the process of sorting, the disk is of great advantage since it allows a rapid access time to the stored data versus sorting from magnetic tapes. Up to two different disk files can reside on the disk at the same time.

Six different pseudo parameters or functions can be created in EDNA. By inputting the appropriate constants and parameters, the following functions were generated at different times during the data analysis : (i) energy of the carbon telescope (E_c); (ii) energy of the alpha telescope (E_α); (iii) PID function of the carbon telescope; (iv) PID function of the alpha telescope and (v) total energy of the coincidence events (E_c+E_α). In the case of time of flight method, instead of defining an alpha PID function, an ET^2 function where E is the alpha energy and T is given by the TAC, of the alpha detector was defined. These functions are more sophisticated than the CPID or CTOT functions used in RALPH. EDNA can generate one dimensional spectra or 64X64 two dimensional arrays of the data with up to eight gating conditions.

The procedure used to analyse the data is illustrated in Fig. III-6. 4-fold coincidence events written on tape by RALPH were read into the disk with appropriate sorting conditions. A PID function for the carbon telescope was defined from which the carbon PID gates were extracted. The 4-fold coincidence events in

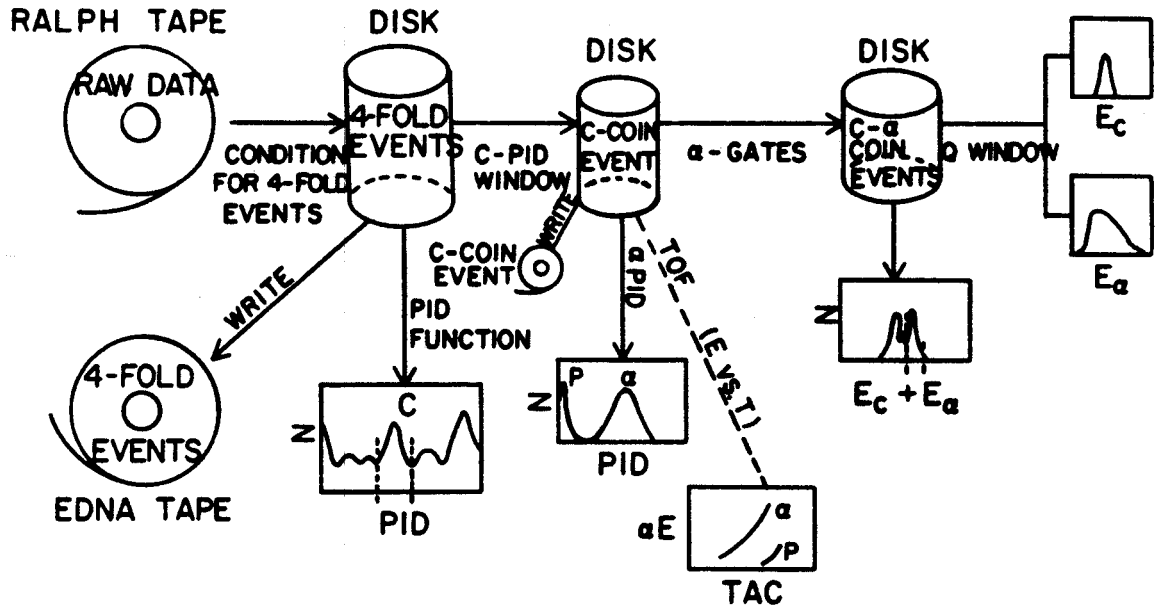

Fig III-6 Schematic illustration of data analysis using the computer program EDNA.

the disk were further sorted using the carbon PID gates obtained. The resultant carbon coincidence events were stored in a second disk file and were used to generate a PID function of the alpha telescope. These data were again sorted using the real or random alpha PID gates. A total energy spectrum E_c+E_α, which corresponds to the Q spectrum of the reaction $^{27}Al + ^{16}O \rightarrow ^{12}C + \alpha + ^{27}Al$, was obtained. The final carbon energy (E_c) and alpha energy (E_α) spectra were created by putting a Q window of -7.16+1 13 MeV on the carbon alpha coincidence events using the total energy function E_c+E_α. The width of the Q window was chosen to ensure that events from contaminants in the target would not be included in the Q window. Data from the time of flight method were treated in a very similar way. The alpha particles were identified by defining an ET^2 function .

EDNA uses floating point arithmetic to compute the exponent E**n in the PID function. This method is relatively slow when handling large amounts of data. In order to facilitate manipulation of data at a later time the sorted data e.g. 4-fold coincidence events and carbon coincidence events were written onto a magnetic tape from the disk. When needed, all these data can be retrieved using EDNA.

2. RSORT :

Towards the end of this project, the disk of the off-line SDS computer broke down and never did recover. Another program RSORT (Fr 79) was used to do the off-line analysis on the new VAX/VMS computer. RSORT was written with a different sorting

structure than EDNA. Instead of defining PID and ET^2 functions to obtain the appropriate carbon and alpha gates. RSORT allows a polygon composed up to ten pairs of points to be drawn around the events of interest in a 2D plot. This feature allows the "gates" to be computed much faster since no exponential functions are required. This is especially important as it allows all carbon single events (carbon particles detected by the carbon telescope) to be sorted out in a resonable amount of time. These events were used to normalize data from different runs. With the new gating feature in RSORT, the Q window consists of a polygon on the E_c vs. E_α 2D plots. This way of gating greatly facilitates extracting events of interest at backward angles.

CHAPTER IV

REDUCTION OF DATA

Before presenting the experimental data from this work in the next chapter, general background information which is needed to understand the data analysis are described here. Section A briefly explains the assumptions used in the data analysis. The off-line analysis using computer programs EDNA and RSORT have been discussed in detail in Chapter III. The method used for subtraction of random events and problems associated with it are discussed in Section B. In Section C through E, different formalisms and quantities used in presenting the data are explained. Errors are discussed in Section F.

A. Data Analysis

A three-body final state of $^{27}Al + ^{16}O \rightarrow ^{12}C + \alpha + ^{27}Al + Q$ is assumed in the data analysis. For most of the angles measured, two major groups of events with Q=-7.16 and Q=-11.59 MeV are observed. The former group with Q=-7.16 MeV corresponds to events with all three final products ^{12}C, α and ^{27}Al in their ground states. The latter group of events, Q=-11.59 MeV can be either events with ^{12}C in its first excited state (2^+) or ^{27}Al in one of its excited states. Attention has been mainly focused on the first group with Q=-7.16 MeV.

The relationship between Q, E_c and E_α is derived in

Appendix A. Using that relationship, the location of events with a certain Q value in a E_c vs. E_α plot can be predicted. Such a plot for $\theta_c=-30^o$, $\theta_\alpha=30^o$, and $Q=-7.16 \pm 1.13$ MeV is shown on Fig. IV-1.

Examples of energy spectra obtained in this experiment will be presented and discussed in the next chapter.

B. Subtraction of Random Events

For the data obtained with the two-telescopes method, the random events (C-α coincidence events in the random part of the TAC spectrum) were analysed in parallel with the real events with the same carbon PID gates, alpha PID gates and Q windows. A corresponding number of random events was subtracted channel by channel to obtain the final carbon and alpha energy spectra. For the case of the time-of-flight method, the alpha PID gate for the accidental events consisted of a polygon with ten times the area of the polygon used to obtain the real events. The random polygonal gate is located in a region of the E_α vs. TAC 2D plot well away from the "real" coincidence events. For the forward angles with $\theta_c=30^o$, the random events were only a small percentage of the total events, < 5%. However, the percentage of the random events is much higher, up to 15% at backward angles and at angles on the same side as the carbon telescope. The random rate is a factor of two worse at all alpha angles when the carbon detector is placed at -40^o. When the random rate is high, random subtraction is especially important in order to obtain the correct

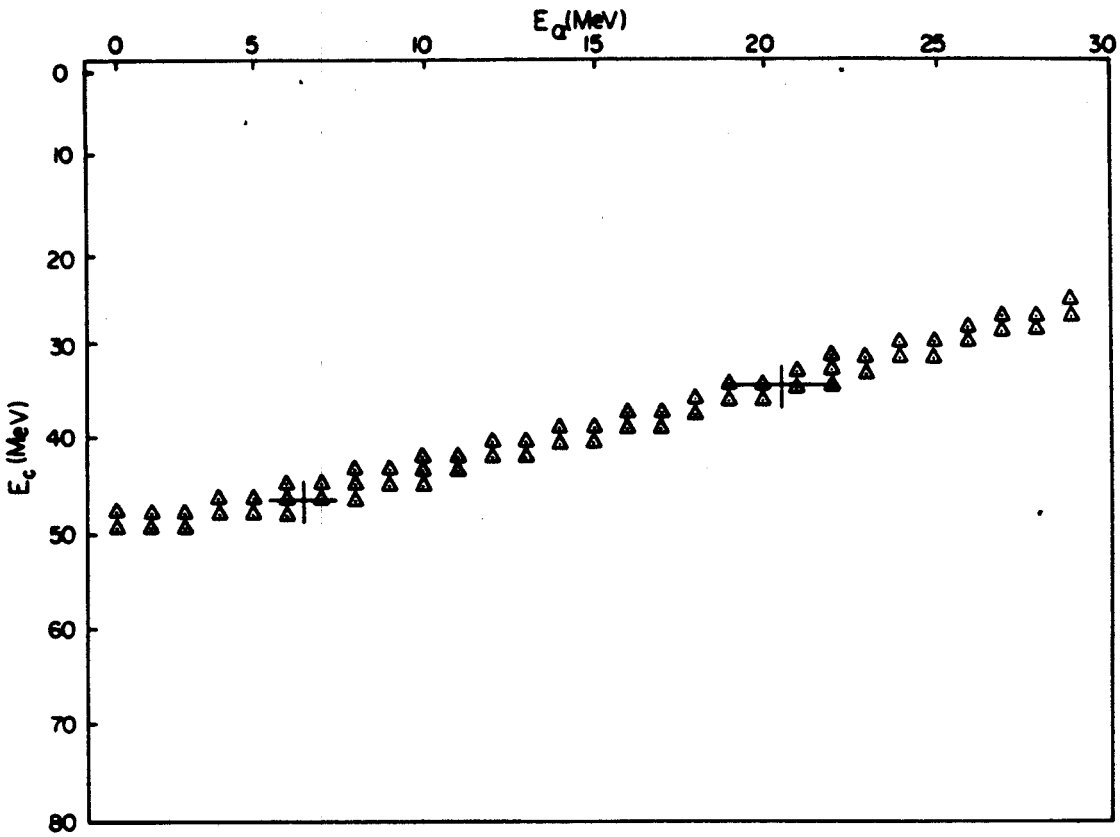

Fig. IV-1 E_c vs. E_α two dimensional plot for θ_c=-30°, θ_α=30°, ϕ_α=0° and Q=-7.16±1.13 MeV The crosses in the plot mark the same points as the crosses in Fig V-3.

shape of the alpha energy spectra.

C. Presentation of Data in the Laboratory Frame

The following formula is used to extract the double differential cross-section $(d^2\sigma/d\Omega_c d\Omega_\alpha)^{lab}$ in the laboratory system.

$$N_{c-\alpha} = N_{beam} \cdot N_{tgt} \cdot (d^2\sigma/d\Omega_c d\Omega_\alpha)^{lab} \cdot \Delta\Omega_c \cdot \Delta\Omega_\alpha \qquad \text{IV-1}$$

where $N_{c-\alpha}$ is the total number of C-α coincidence events ; N_{beam} is the total number of beam particles ; N_{tgt} is the total number of target atoms per unit area ; $\Delta\Omega_c$ is the solid angle of the carbon telescope and $\Delta\Omega_\alpha$ is the solid angle of the alpha detector.

For the C-α correlation at fixed θ_c, the carbon singles events served as a monitor providing relative normalizations from run to run. The total number of carbon particles detected by the carbon telescope, N_c, can be expressed as

$$N_c = N_{beam} \cdot N_{tgt} \cdot (d\sigma/d\Omega_c)^{lab} \cdot \Delta\Omega_c \qquad \text{IV-2}$$

Combining Equation IV-1 and IV-2

$$(d^2\sigma/d\Omega_c d\Omega_\alpha)^{lab} = k \cdot (N_{c-\alpha}/N_c)/\Delta\Omega_\alpha \qquad \text{IV-3}$$

where $k=(d\sigma/d\Omega_c)^{lab}$ is a constant at fixed θ_c. Thus, the relative double differential cross-section was obtained very accurately independent of beam current determination, target uniformity, and solid angle of the carbon telescope which may vary from run to

run.

D. Presentation of Data in the $^{31}P^*$ Center of Mass Frame

In the earlier work of Harris et al (Ha 77a), a pre-equilibrium sequential break-up process was proposed as the major reaction mechanism for the $^{27}Al(^{16}O,^{12}C\alpha)^{27}Al$ reaction. Such a mechanism can be represented as follows:

$$^{27}Al + ^{16}O \rightarrow ^{12}C + ^{31}P^*$$

$$^{31}P^* \rightarrow \alpha + ^{27}Al$$

The carbon singles energy spectra obtained were approximately gaussian in shape with a peak at about 44 MeV for $\theta_c=-30^o$ and at about 38 MeV for $\theta_c=-40^o$. If two body kinematics is assumed, $^{31}P^*$ has an excitation energy of about 14.5 MeV. In order to compare with the earlier work and to further understand this mechanism, all the data taken have been plotted in the $^{31}P^*$ center-of-mass system. The formula for transforming from the laboratory frame to the $^{31}P^*$ center-of-mass frame is derived in Appendix B, and can be written as

$$(d^2\sigma/d\Omega_c^{cm}d\Omega_\alpha^{cm})^{cm} = J_\alpha(\theta_\alpha)\cdot J_c(\theta_c)\cdot(d^2\sigma/d\Omega_c d\Omega_\alpha)^{lab} \qquad \text{IV-4a}$$

where $(d^2\sigma/d\Omega_c^{cm}d\Omega_\alpha^{cm})^{cm}$ is the differential cross-section in the $^{31}P^*$ center of mass frame and J_c and J_α are the Jacobians that transforms the C and α detector solid angles from the laboratory to the $^{31}P^*$ center-of-mass system. Note that J_c is independent of alpha angle.

Experimentally, the differential cross-section in the $^{31}P^*$ center of mass frame is a little more complicated than equation IV-4a indicates. One reason is due to the fact that the coincident carbon energy spectrum has a finite width. The full width at half maximum is about 7.5 MeV. The excitation energy and the lab velocity of the recoiling $^{31}P^*$ depends on the energy of the carbon particles. Events at a fixed θ_α and fixed θ_c but with different energies would correspond to different θ_α^{cm} and J_α. As a consequence there is no single Jacobian or θ_α^{cm} for transformation to the $^{31}P^*$ center of mass frame. One can at best choose an average center of mass frame and transform all events to this frame. With this choice of frame, J_c and J_α become functions of E_c. Equation IV-4a may be written

$$(d^2\sigma/d\Omega_c^{cm}d\Omega_\alpha^{cm})^{cm} = k\int dE_i[J_c(E_i)J_\alpha(E_i)/\Delta\Omega_\alpha][dN_{c-\alpha}/dE_i] \qquad \text{IV-4b}$$

However, the Jacobians $J_\alpha(E_i)$ and $J_c(E_i)$ do not change very much over the carbon energy range of the coincidence events. The value of $J_c(E_i)$ changes by about 10% over a 10 MeV range. The data are plotted in the center of mass frame of $^{31}P^*$ with 14.5 MeV excitation energy. This is justified since the most probable excitation energy of the $^{31}P^*$ remains constant at about 14.5 MeV over most of the alpha lab angles measured.

Data from the present experiment has been analysed with both Equation IV-4a and IV-4b. They agree within experimental uncertainties for most of the angles, especially at the forward angles. Data presented in this dissertation are analysed with

Equation IV-4b.

E. Presentation of Data in Velocity Space

Presenting the C-α correlation function in a certain center-of-mass frame implicitly assumes the reaction proceeds through a particular sequential process. For a truly sequential process, the proper choice of frame for plotting the angular correlation can simplify considerably the understanding of the data. An improper choice of frame, however, can introduce systematic effects that can confuse the interpretation of the data. In order to eliminate this type of model dependence, the data have also been plotted in the Galilean invariant velocity space. This form of data presentation has the advantage that all frames in which the correlation may be plotted are treated in a balanced way. As a result the data may themselves suggest a suitable frame for plotting.

Consider the alpha particles moving with velocity V_{α}^{x} in the X center-of-mass frame which itself is moving at a constant velocity V_x with respect to the laboratory. Since the carbon telescope is fixed at θ_c for the C-α correlation, $(d\sigma/d\Omega_c)^{lab}$ is a constant quantity regardless of the frame in which the alpha particles are emitted. By definition :

$$(d\sigma/d\Omega_c)^{lab} = \iint [d^4\sigma/d\Omega_c d^3V_{\alpha}^{x}] \cdot [V_{\alpha}^{x}]^2 \cdot dV_{\alpha}^{x} d\Omega_{\alpha}^{x} \qquad \text{IV-5}$$

$$(d\sigma/d\Omega_c)^{lab} = \iint [d^3\sigma/d\Omega_c^{lab} d\Omega_{\alpha}^{x} dE_{\alpha}^{x}] d\Omega_{\alpha}^{x} dE_{\alpha}^{x} \qquad \text{IV-6}$$

where V_{α}^{x}, Ω_{α}^{x}, E_{α}^{x} are the alpha velocity, solid angle and energy relative to frame X. Using the identity dE = mVdV and combining Equations IV-5 and IV-6

$$d^4\sigma/d\Omega_c d^3V_{\alpha}^{x} = (m_{\alpha}/V_{\alpha}^{x}) \cdot (d^3\sigma/d\Omega_c^{lab} d\Omega_{\alpha}^{x} dE_{\alpha}^{x}) \qquad \text{IV-7}$$

$(d\sigma/d\Omega)^{lab}$ is a conserved quantity i.e. independent of the choice of frame X, thus the left hand side of IV-7 is independent of choice of frame also. The laboratory frame is chosen to evaluate the quantity $d^4\sigma/d\Omega_c d^3V_{\alpha}$. From equation IV-3

$$d^4\sigma/d\Omega_c d^3V_{\alpha} = [k'/V_{\alpha}^{lab}] \cdot [dN_{c-\alpha}/dE_{\alpha}^{lab}] \cdot [1/(N_c \cdot \Delta\Omega_{\alpha}^{lab})] \qquad \text{IV-8}$$

where $k' = m_{\alpha} \times k$.

The cross-section at different θ_{α} but at fixed θ_c can be presented in a velocity plot as contours corresponding to the quantity $d^4\sigma/d\Omega_c d^3V_{\alpha}$ at various θ_{α} and V_{α}. Examples of velocity contour plots are shown in next chapter. In a velocity contour plot, the beam is defined to be 0^{o} and the origin of the plot is arbitrarily chosen to be the velocity of the lab frame which is zero. If the plot were to be viewed from a different frame X, the origin of the plot would be moved to V_x but the contours would remain the same.

F. DISCUSSION OF ERRORS

1. Error in Determining the Relative Double Differential Cross-Section $W_{rel}(\theta)$:

Using the carbon singles events detected by the carbon telescope as relative normalization for C-α angular correlation data, the dependence of $W_{rel}(\theta)$ on target thickness, beam current and the carbon detector solid angle was eliminated. From Equation IV-3

$$W_{rel}(\theta) = (1/k)\cdot(d^2\sigma/d\Omega_c d\Omega_\alpha)^{lab}$$
$$= (N_{c-\alpha}/N_c)/\Delta\Omega_\alpha \qquad \text{IV-9}$$

$$\delta W_{rel}(\theta)/W_{rel}(\theta) = [(\delta N_{c-\alpha}/N_{c-\alpha})^2+(\delta N_c/N_c)^2+(\delta\Delta\Omega_\alpha/\Delta\Omega_\alpha)^2]^{1/2} \qquad \text{IV-10}$$

where $\delta W_{rel}(\theta)$ is the error in $W_{rel}(\theta)$.

During the analysis both the carbon and alpha PID gates could be clearly defined without any ambiguity. N_c could be determined fairly accurately and since $N_c >> N_{c-\alpha}$, the error introduced by N_c is negligible compared to $N_{c-\alpha}$. On the other hand, Q windows on the total energy plot or two dimensional E_c vs. E_α plots could not be determined with such accuracy. This was a major problem, especially at angles where the accidental rate is high and the peak-to-valley ratio of the Q-value spectrum is poor. Whenever such doubts arose, the sensitivity of $N_{c-\alpha}$ to the Q gate in the E_c vs. E_α plot was determined by varying the Q gate. From this sensitivity the error introduced by the Q gate was estimated and folded into the total experimental error. Where the Q-value peak-to-valley ratio was poor, these errors were on the order of 10%.

The target (1 mg/cm^2 ^{27}Al) will range out alpha particles with energies less than 1 MeV. In addition, the electronic system used in the experiment has a threshold of .5 MeV. Cutoff of low energy alpha particles becomes an important source of error at very backward angles. The low energy portion of the alpha energy spectra rise very rapidly to a peak and then falls off exponentially. If the cutoff occurs at an energy lower than the peak energy, the alpha energy spectrum was assumed to have a similar shape as one at a slightly more forward angle. The error introduced in estimating $N_{c-\alpha}$ at these angles is of the order of 20%. When the cutoff is very severe, the peak of the alpha energy is not recognizable. There is no acceptable way to estimate $N_{c-\alpha}$ at these angles. These data were not included in computing the double differential cross-sections.

Another problem arose from the cutoff of low energy carbon particles in the carbon telescope. This occured when a "new" group of events with lower carbon energy and higher alpha energy appeared at θ_α=-17°,-43°, θ_c=-30°, i.e. when the alpha detector is near the carbon telescope. During the experiment the discriminator on the SCA of the carbon DE detector electronic system is set to exclude elastically scattered oxygen from the carbon telescope system in order to cut down the computer dead time. In so doing, a cutoff of low energy carbon particles is also introduced. The carbon particle cutoff limit is 14 MeV. Generally, this is near the energy that carbon particles would range out in the carbon DE detectors (14.3, 17.3 and 20 μ) used in

the experiment. Such low energy carbon particles are not observed at other angles. The error associated with the cutoff of these low energy carbon particles cannot be estimated and the double differential cross-section obtained at these angles represent an lower limit.

Data taken in the forward angles at positive $\theta_{c.m.}$ are free of the uncertainties discussed above. The error associated in determining $\Delta\Omega$ will be discussed in the next section and was much smaller than the uncertainties in $N_{c-\alpha}$. In conclusion, except for a couple of points at the most backward angles, the error in the relative double differential cross section mainly came from the statistical error in $N_{c-\alpha}$. This fractional statistical error $\delta N_{c-\alpha}/N_{c-\alpha}$ is derived below as follows. The number of true coincidence events $N_{c-\alpha}$ is given by

$$N_{c-\alpha} = N_{c-\alpha}^{real} - N_{c-\alpha}^{rand} \times f \qquad \text{IV-11}$$

$$\delta N_{c-\alpha}/N_{c-\alpha} = \frac{[\ (N_{c-\alpha}^{real})^2 + (N_{c-\alpha}^{rand} \times f)^2\ ]^{1/2}}{[\ N_{c-\alpha}^{real} - N_{c-\alpha}^{rand} \times f]} \qquad \text{IV-12}$$

where $N_{c-\alpha}^{real}$ is the number of real including random C-α coincidence events which are in coincidence with the "real" TAC peak; $N_{c-\alpha}^{rand}$ is the number of random C-α coincidence events and f is the ratio of the area of "real" TAC window to the area of the random TAC window.

2. Error in Determining the Absolute Double Differential Cross-Section $W_{abs}(\theta)$:

From Equation IV-1. $W_{abs}(\theta)$ can be written as

$$W_{abs}(\theta) = (d^2\sigma/d\Omega_c d\Omega_\alpha)^{lab} = N_{c-\alpha}/(N_{beam}N_{tgt}\Delta\Omega_c^{lab}\Delta\Omega_\alpha^{lab})$$

IV-13

$$\delta W_{abs}(\theta)/W_{abs}(\theta) = [(\delta N_{c-\alpha}/N_{c-\alpha})^2 + (\delta N_{tgt}/N_{tgt})^2 + (\delta\Delta\Omega_c/\Delta\Omega_c)^2 + (\delta\Delta\Omega_\alpha/\Delta\Omega_\alpha)^2]^{1/2}$$

IV-14

The uncertainty in $N_{c-\alpha}$ was discussed in the previous section. For the forward angles, $\theta_\alpha < 90^o$ $\delta N_{c-\alpha}/N_{c-\alpha}$ is purely statistical. The solid angle $\Delta\Omega$ is calculated with the following formula

$$\Delta\Omega = \text{area}/(\text{distance})^2 = \pi r^2/d^2$$

IV-15

$$\delta\Delta\Omega/\Delta\Omega = 2[(\delta r/r)^2 + (\delta d/d)^2]^{1/2}$$

IV-16

where r is the radius of the detector aperture and d is the distance of the detector to the center of the target. All the apertures were machined very accurately. δr is about .0025 cm, d is generally measured to an accuracy of .08 cm. In general, d is greater than 7.5 cm and r is greater than .6 cm. Consequently $\delta r/r$ and $\delta d/d$ are both less than 2.5 %. The above discussion is correct only when the aperture's area is much smaller than the active area of the detector. In some of the experimental runs

which were not used to determine the absolute value of the double differential cross section, the aperture sizes were about as big as the active area of the detectors. The alignment of the detector mount will affect the accuracy in determining the active area of the detector being exposed. An uncertainty of 5% is assigned to $\delta r/r$ in these cases. The error contributed by the solid angles of the detectors is negligible at most angles compared to other sources of experimental errors.

The following formulae are used to compute the number of particles in the target per unit area :

$$N_{tgt} = t \times A_o/M_{tgt} \qquad \text{IV-17}$$

$$\delta N_{tgt}/N_{tgt} = N_{tgt} \times \delta t/t \qquad \text{IV-18}$$

where t is the target thickness in mg/cm^2 A_o is Avogradro's number and M_{tgt} is the atomic mass of target in mg. The thickness of the target t can be determined to within 15% by measuring energy loss of 5.48 MeV alpha particles from an ^{241}Am source. The target uniformity is harder to determine. In general, $\delta t/t$ is taken to be about 20%.

The number of beam particles is computed by integrating the beam current on the Faraday cup.

$$N_{beam} = \mu c/(1.6 \times 10^{-19} \times 2) \qquad \text{IV-19}$$

$$\delta N_{beam}/N_{beam} = \delta\mu c/\mu c$$

IV-20

where μc is the total micro-coulomb of charge collected which is accurate to 1% and $\hat{Z}$ is the average charge state of the beam particles after passing through the target. The distribution of charge states of O^{16} after passing through an Al foil has been measured by Martin (Ma 69) at 67 MeV. The value of $\hat{Z}$ is tabulated in Atomic Data Tables (Wit 73) and is equal to 7.6.

The dependence of $W_{abs}(\theta)$ on N_{beam} and N_{tgt} could have been eliminated by monitoring the elastic cross-section of ^{16}O on ^{27}Al at a forward angle. Then

$$W_{abs}(\theta) = (N_{c-\alpha}/N_o) \times [\Delta\Omega_{mon}/\Delta\Omega_c\Delta\Omega_\alpha) \times (d\sigma/\Delta\Omega_{mon})_o^{lab}$$

IV-21

where N_o is the total number of elastically scattered oxygen detected and $(d\sigma/d\Omega_{mon})_o^{lab}$ is the elastic scattering differential cross-section for oxygen on ^{27}Al. Unfortunately when the forward angle data were being taken, it was physically impossible to place the monitor detector at forward angles without the monitor detector being blocked by either the carbon or the alpha detectors. Thus the monitor was usually located out-of-plane at about 30^o. It was used mainly as an indicator for systematic error for a particular run. During one of the runs, however, the monitor was placed at 12^o in-plane. Using optical model parameters (V=15 MeV ; W=9 33 MeV ; r_o=1 263 fm ; a=.64 fm) given by Dauk et al (Da 75) which fit the 65 MeV data of Back et al. (Ba 77), the differential cross-section of ^{16}O on ^{27}Al can be

calculated. $W_{abs}(\theta)$ obtained in this way agrees with $W_{abs}(\theta)$ determined from target thickness to within the experimental uncertainties.

In conclusion, the error associated with the absolute differential cross-section is about 20%. This error comes mainly from the target nonuniformity and the target thickness determination.

3. Error in Determining the Contours in the Velocity Space:

In constructing the velocity contour plot, the quantity $dN_{c-\alpha}/dE_i$ is needed in Equation IV-8. Due to the low coincidence cross-sections, $dN_{c-\alpha}$ has very poor statistics even at forward angles. Each alpha energy channel dE_i corresponds to .5 MeV. Even so, a three channel averaging is necessary to smooth the alpha energy spectrum of $N_{c-\alpha}$. In view of the amount of time involved, it is impossible to measure C-α coincidence events at smaller θ_α steps. Furthermore, the high counting rate from elastic scattering of ^{16}O on ^{27}Al eliminates the possibility of taking data at the very forward angles close to the beam with a reasonable beam current. The finite size of the carbon telescope only permits data to be taken at angles 13^o on either side of the carbon telescope. With all these constraints the contours on the velocity plots are only qualitative indications of the general features.

CHAPTER V

PRESENTATION AND DISCUSSION OF EXPERIMENTAL RESULTS

A. Experimental Results

Fig. V-1 shows a schematic view of the experimental set-up. The reaction plane is defined by the beam and the carbon telescope. The beam direction is defined to be 0^{o} in the laboratory. Angles on the same side as the carbon telescope are defined to be negative. The coordinates used in the center of mass frame of $^{31}P^{*}$ are described in Appendix B. Out of plane angles are in the plane containing the recoil direction of $^{31}P^{*}$. Both in-plane and out-of-plane C-α angular correlation have been taken at $\theta_c=-30^{o}$ and $\theta_c=-40^{o}$. Since the scattering chamber is not equipped with an out-of-plane movable arm, data were taken at 30^{o} intervals for the out-of-plane angular correlation function.

1. In-Plane Data, $\theta_c=-30^{o}$:

The procedure for extracting events of interest has been explained in detail in Chapter III-C-2.3 and Chapter IV-A. Examples of different spectra obtained will be illustrated in this section.

The total energy spectrum (E_c+E_α) obtained is shown in Fig. V-2. Accidental events have not been subtracted. The two dominant peaks observed kinematically correspond to the ground state of carbon with Q=-7.16 MeV and the 4.43 MeV (2^{+}) state of carbon with Q=-11.59 MeV. The valley between these peaks is

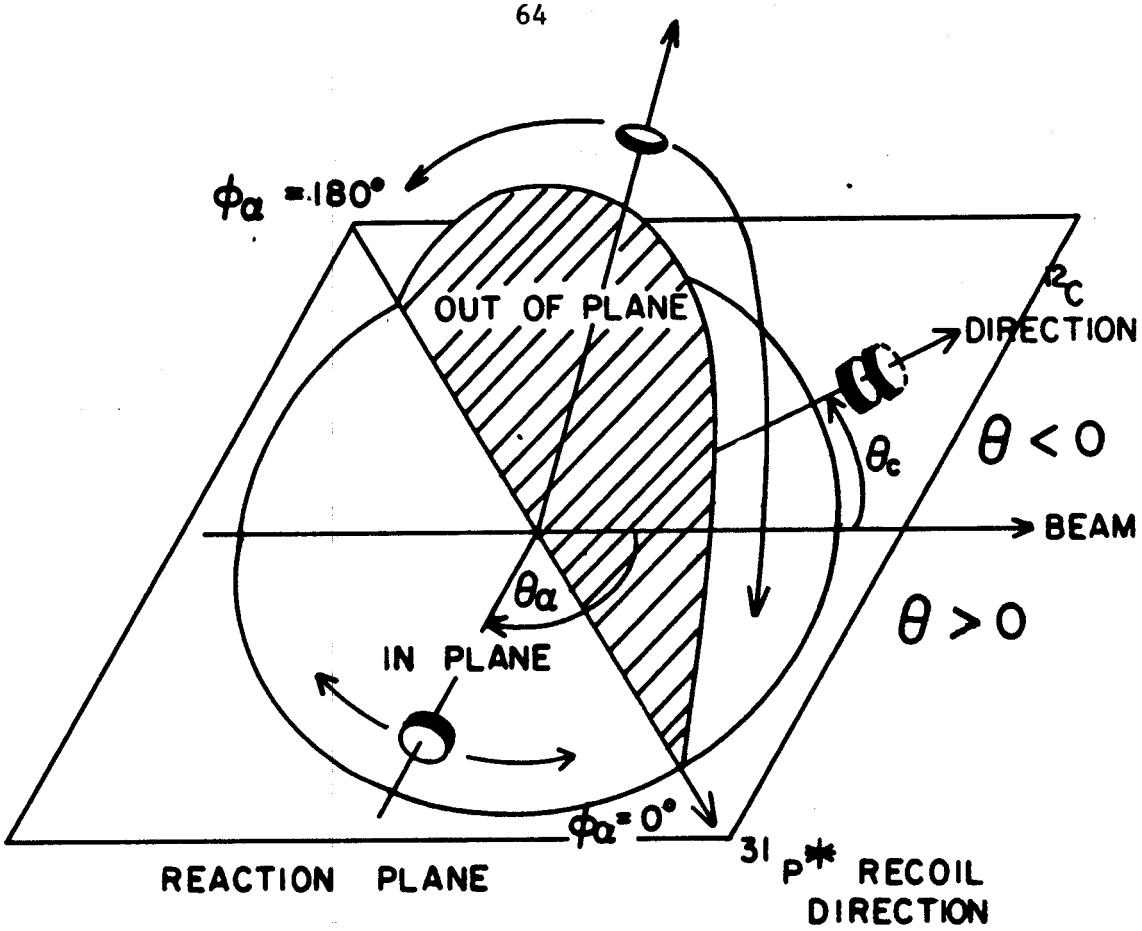

Fig V-1 Schematic diagram of the experimental set up.

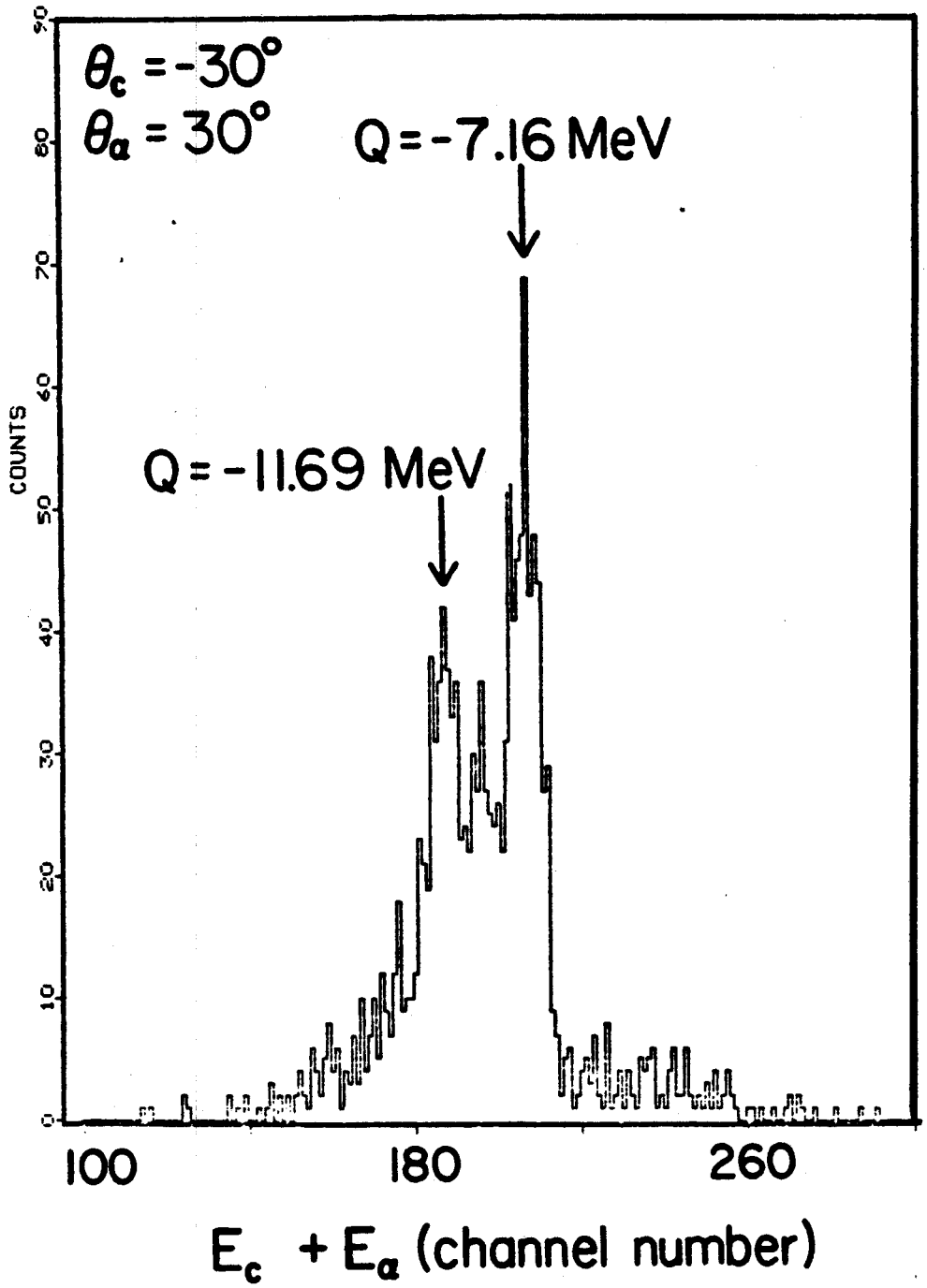

Fig. V-2 Example of total energy (E_c+E_α) spectrum of $^{27}Al(^{16}O,^{12}C\alpha)^{27}Al$ obtained off-line using the program RSORT for θ_c=-30°, θ_α=30°.

probably filled with events that correspond to excited states of ^{27}Al and contributions from $^{12}C(^{16}O\ ^{12}C\alpha)$ and $^{16}O(^{16}O,^{12}C\alpha)$ events. Counts with higher carbon and alpha energy than the events with Q=-7.16 MeV mainly come from accidental coincidences. Due to lack of statistics, channel by channel subtraction is impractical. However, at angles where the accidental rate is high, channel by channel subtraction is feasible for the total energy plot. Fig. V-3 is a corresponding 2D plot, E_C vs. E_α. Similar features as those discussed above are observed.

Figs. V-2 and V-3 are a typical total energy spectrum and a 2D plot for forward angles, $\theta_\alpha < 90^o$ At more backward angles, due to the straggling of low energy alpha particles and higher accidental counting rate, the peak with Q=-7.16 MeV tends to smear out and the peak to valley ratio is not as good as those obtained at the forward angles. Another deviation from the general characteristics mentioned above is the appearance of another group of events with low carbon energy and high alpha energy at θ_α=-17^o and -43^o. The E_C vs. E_α 2D plot for θ_α=-17^o is shown in Fig. V-4. The second group of events was not observed at other angles.

Fig V-5 shows the C-α angular correlation in the lab frame $(d^2\sigma/d\Omega_C d\Omega_\alpha)^{lab}$ of Equation IV-1. It peaks towards the beam to the smallest angle measured. Such strong peaking towards the beam persists even when the data is plotted in the center of mass frame of the recoiling $^{31}P^*$ nucleus in Fig. V-6. Note that the recoil direction of $^{31}P^*$ is defined to be zero degree in the center of mass system of $^{31}P^*$. The C-α angular correlation reaches a

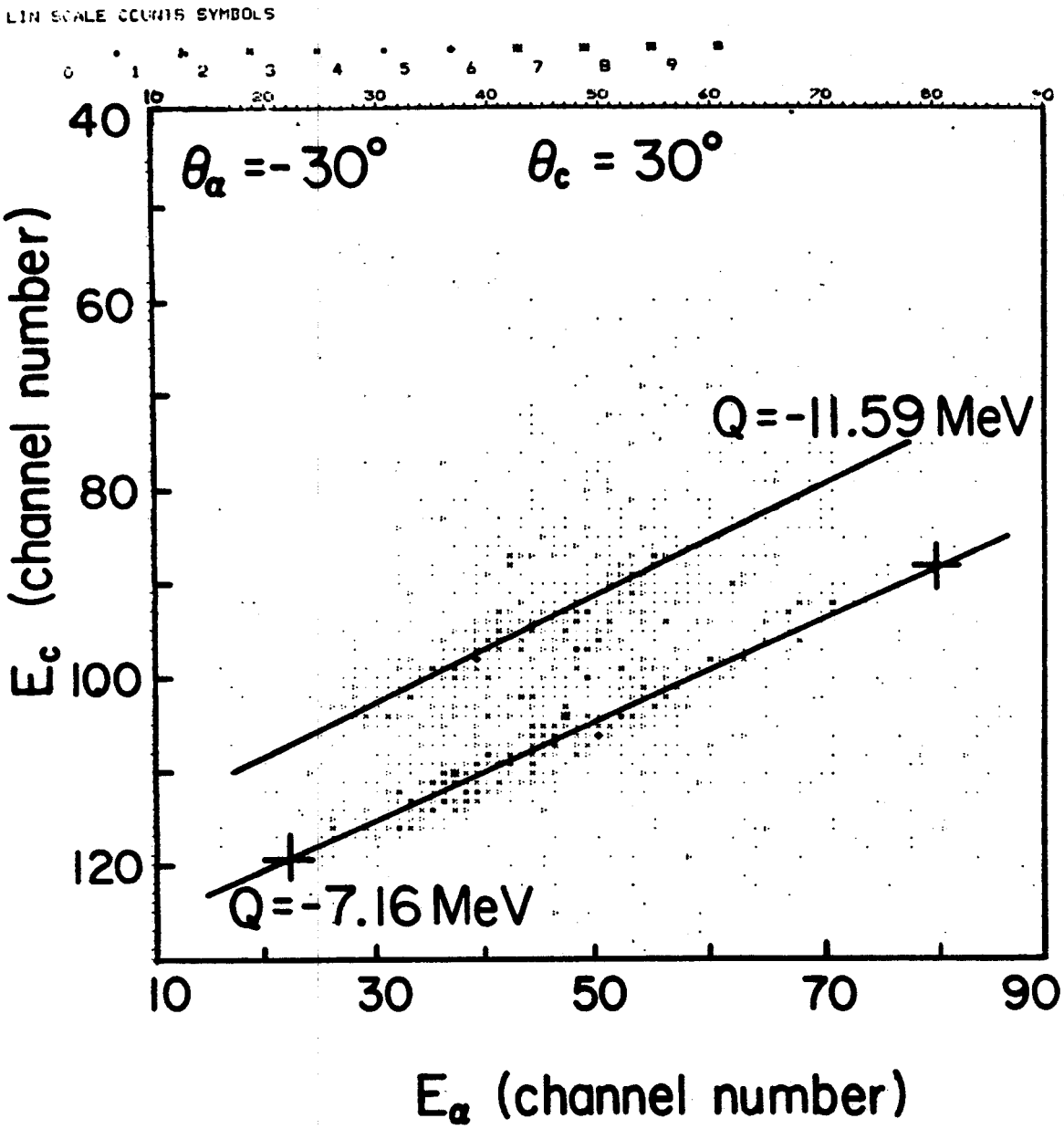

Fig V-3 Corresponding E_c vs. E_α two dimensional plot for Fig. V-2 obtained off-line using the program RSORT for $\theta_c = -30^\circ$, $\theta_\alpha = 30^\circ$

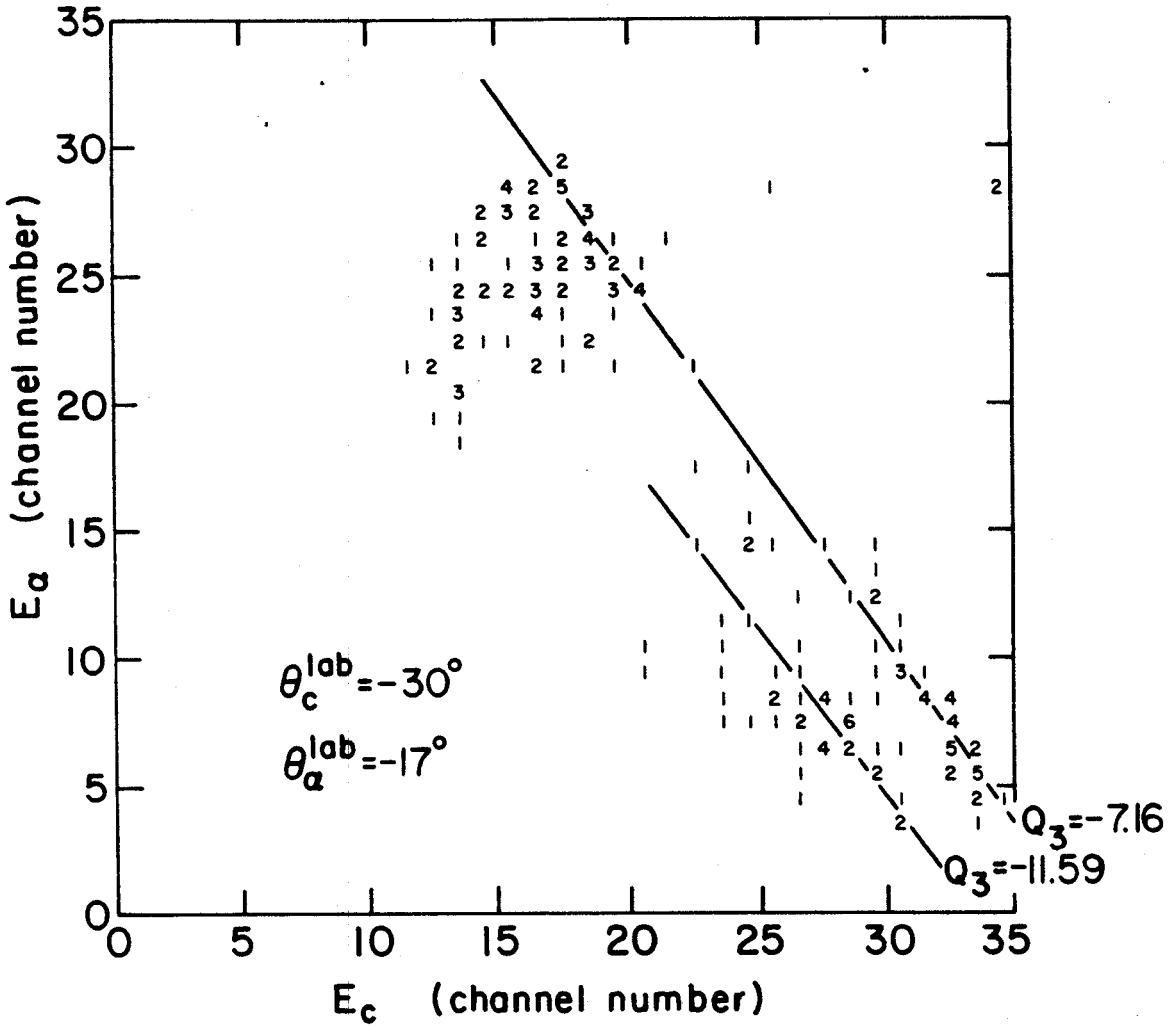

Fig V-4 E_c Vs. E_α two dimensional plot obtained off-line using the program EDNA for θ_c=-30°, θ_α=-17°

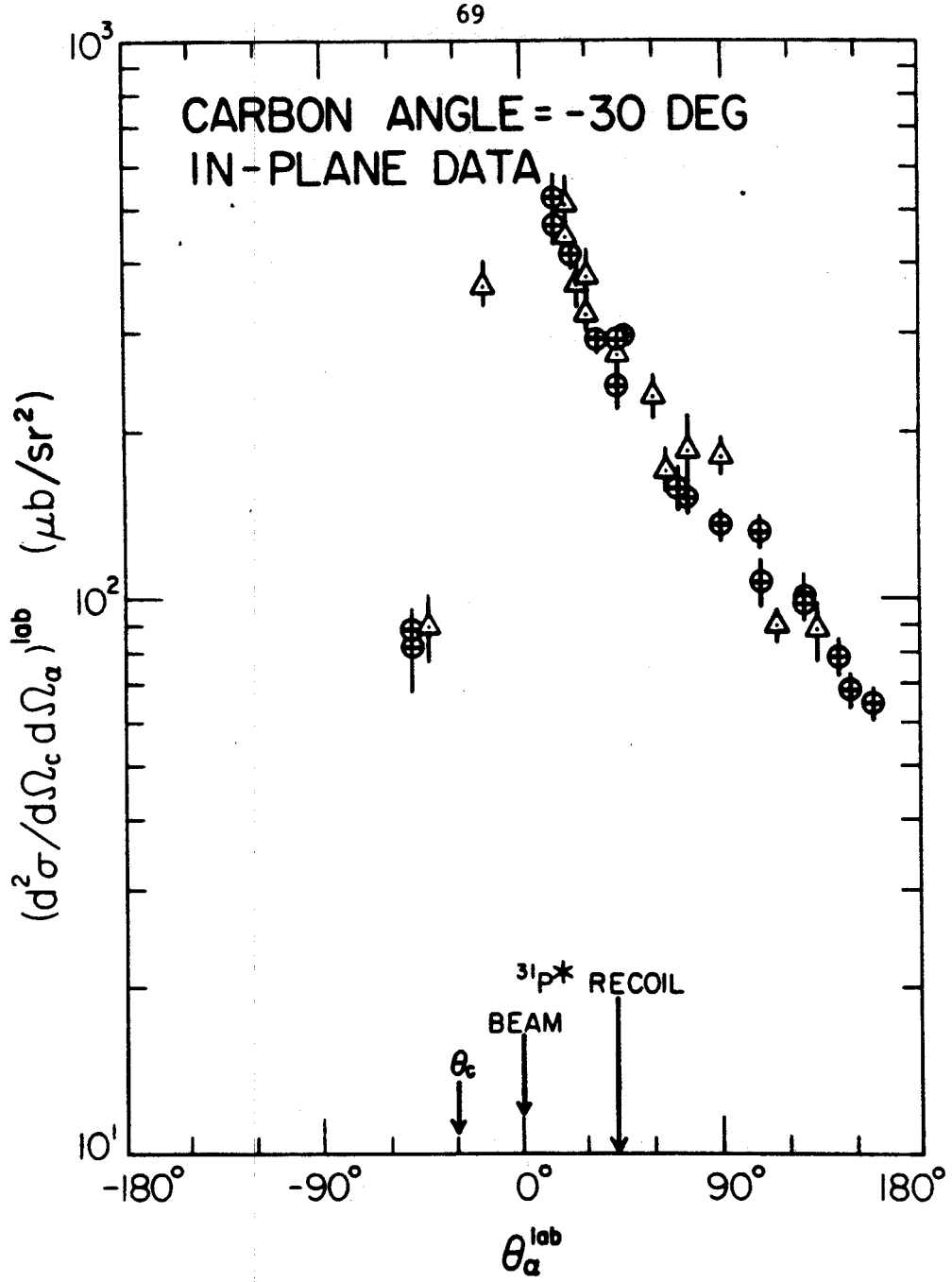

Fig. V-5 In-plane C-α angular correlation function in the lab system, θ_c=-30°. Open triangles are data taken with the two-telescope method and circles are data taken with the time-of-flight method. All the data are normalized with respect to each other using the single events detected by the carbon telescope.

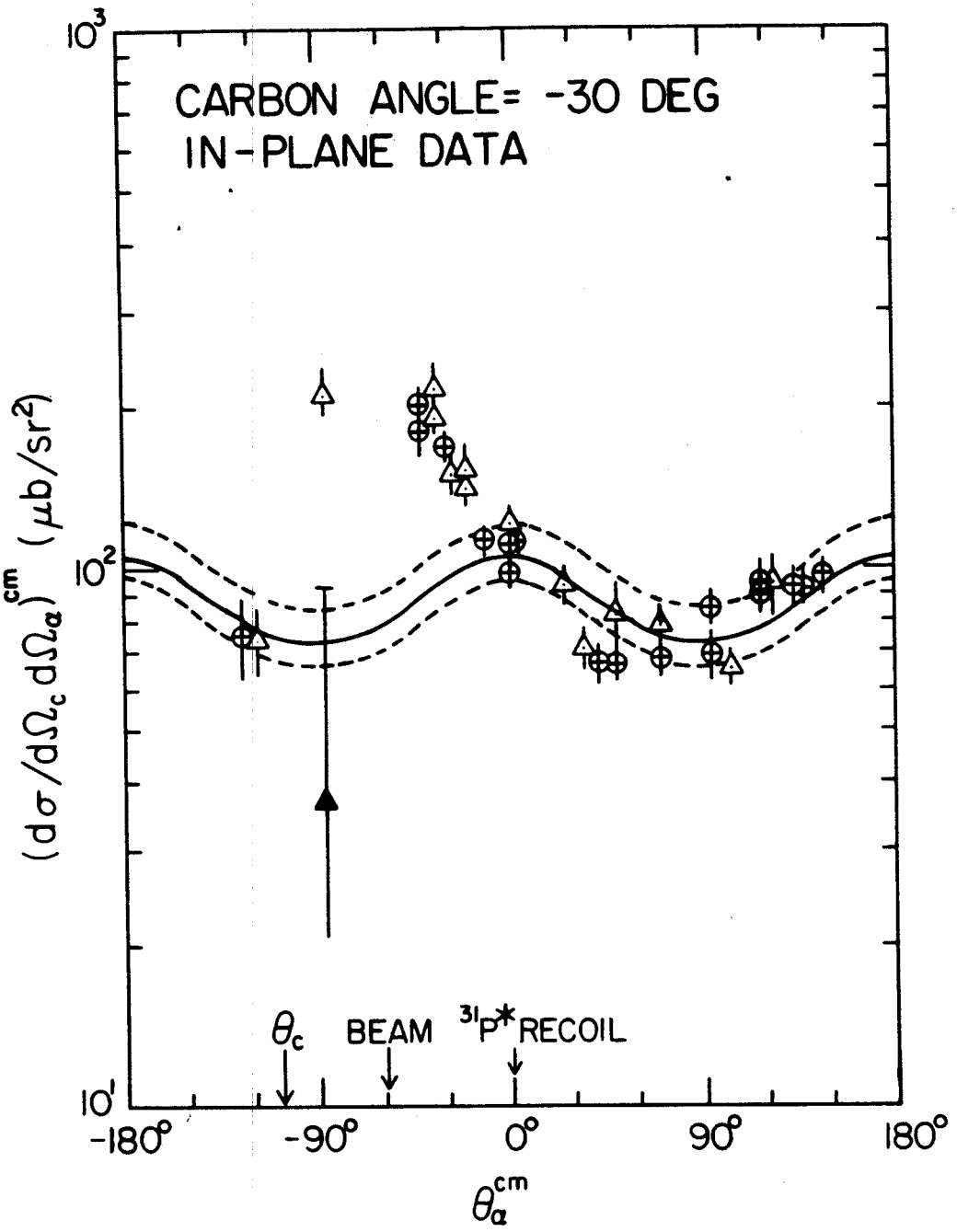

Fig V-6 In-plane C-α angular correlation function in the center of mass system of $^{31}P^*$ (E_x=14.5 MeV), θ_c=-30°. See Fig. V-4 for explanation of symbols for the data points. The solid triangle is obtained when the contribution due to break-up of $^{16}O^*$ is subtracted. the solid curve is the best fit of Equation V-7. The dashed curves indicates the upper and lower limit by adjusting the normalization constant Y_o of Equation V-3.

minimum about 90^{o} and rises at backward angles. Two main features observed, the forward angle peaking and a backward angle rise are in disagreement with the results of Harris et al. (Ha 77a). The earlier results indicated that the C-α angular correlation was peaked along the recoil direction of $^{31}P^{*}$ and continued to decrease at backward angles past 90^{o} in the center of mass systen of $^{31}P^{*}$. For comparison, results from this work and from that of Harris et al. (Ha 77a) are plotted in Fig. V-7. The discrepancy at the backward angles may in part be explained by the fact that the DE detector of the alpha telescope used by Harris et al. was 12μ thick. A 12μ thick DE detector will range out alpha particles with energy less than 3 MeV. The time of flight method used in this work has no such cutoff problem. No satisfactory answer seems to explain the discrepancy which exists at the forward angles. During the course of this work, measurements at these forward angles have been repeated several times with both the two-telescopes method and TOF method with reproducible results. The discrepancy with the earlier work of Harris et al. persists.

The in-plane correlation data have also been plotted in the velocity space. Fig. V-8 is such a plot. The origin O corresponds to the velocity of the laboratory system which is zero. The shaded circle indicates the low alpha energy threshold of the experimental set-up. As will be discussed in more detail later, the most probable excitation energy of $^{31}P^{*}$ is found to be constant at about 14.5 MeV for all the angles measured. From two-body kinematics, the velocity of $^{31}P^{*}$ with 14.5 MeV excitation

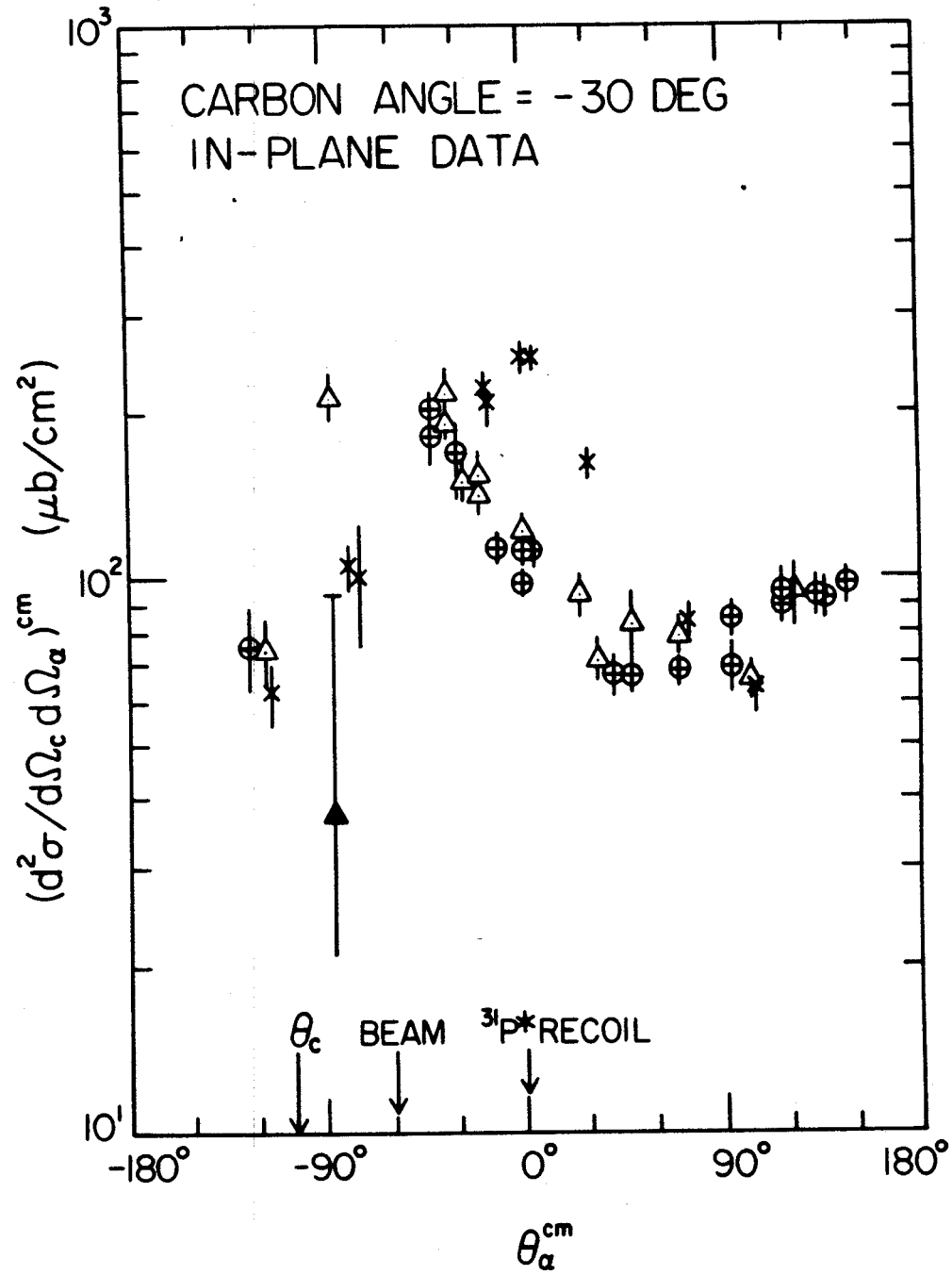

Fig. V-7 Comparison of in-plane C-α angular correlation function in the center of mass system of $^{31}P^*$ (E_x=14.5 MeV) obtained in this work and the work of Harris et al. (Ha 77a) denoted by *.

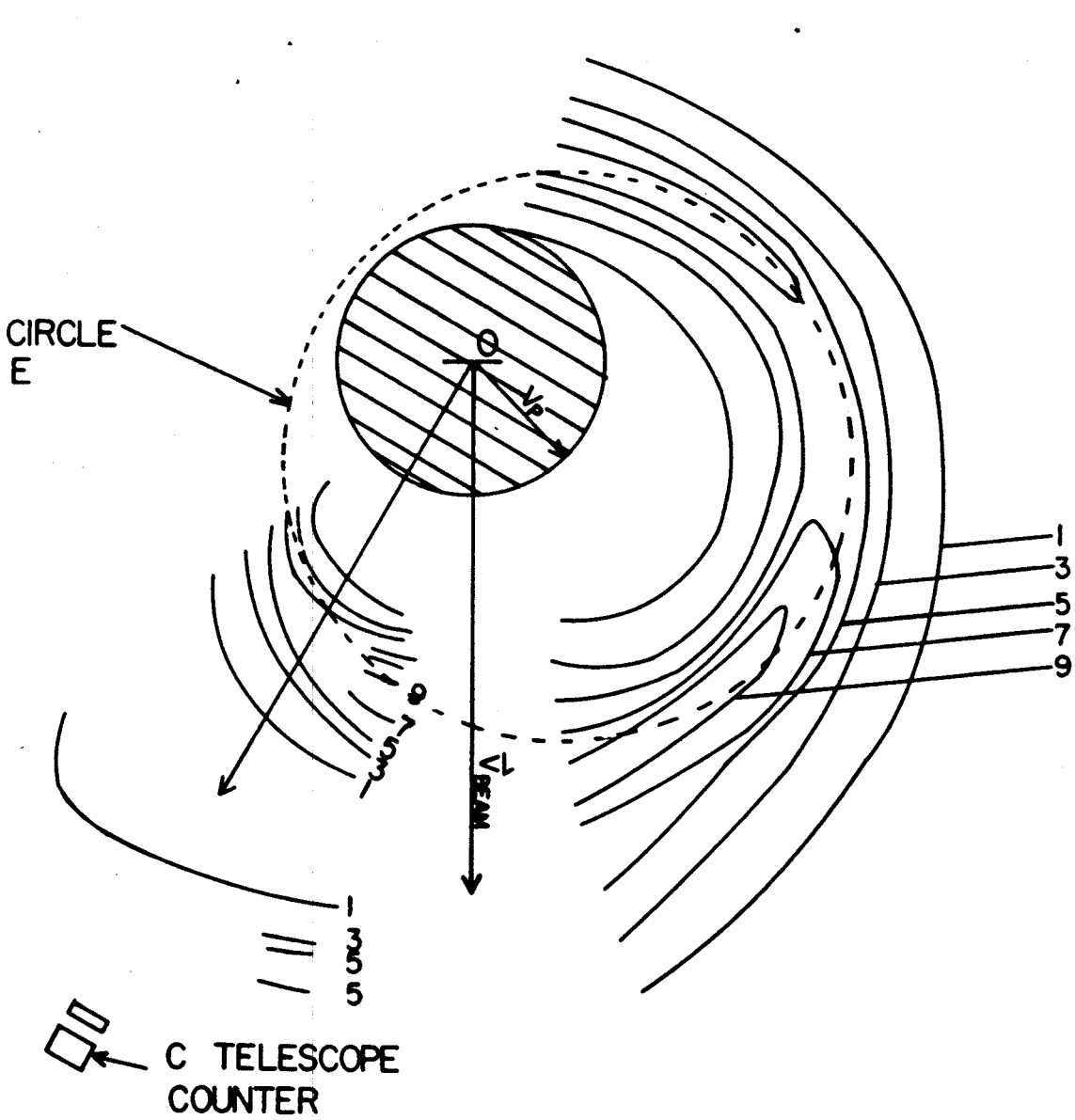

Fig V-8 Velocity contour plot for the in-plane data θ_c=-30°. O is the velocity of the lab system which is at rest. The shaded circle represents the α threshold of the experiment. V_p is the velocity of the recoiling $^{31}P^*$ (E_x=14.5 MeV). The dashed circle (circle E) is centered at V_p with radius equal to the center of mass velocity of the alpha particle, $^{31}P^*$ (14.5 MeV) = α + ^{27}Al. One unit of the contour represents approximately 10 ub/sr(cm/ns)$^{-3}$.

energy can be determined and is shown by the arrow labelled V_p in the velocity plot. Circle E is centered at the recoiling velocity of $^{31}P^*$. The radius of the circle corresponds to the center of mass velocity of the alpha particle if $^{31}P^*(14.5\ MeV) \rightarrow \alpha + ^{27}Al(g.s.)$ is assumed.

As explained in Chapter IV-F-4, the statistical and angular interval limitations of the data set result in considerable uncertainties in the construction of the contour plot. Therefore the velocity plot gives only qualitative information. Nevertheless, the peak cross-section at all angles lies very close to circle E and can be attributed to alpha particles emitted from the recoiling $^{31}P^*$ nucleus. It can be clearly seen on the velocity plot that another distinctive group of events appears at angles around the carbon telescope. This group of events has high alpha energy and correspondingly low carbon energy. Partial experimental cutoff of low energy carbon particles occurred for these groups of events.

The contours at forward angles on the opposite side of the beam from the carbon telescope are more spread out than at backward angles. In order to explore this effect quantitatively, the second moment $\langle\sigma_v^2\rangle$ of the velocity plot are plotted in Fig. V-9 as a function of alpha angles. $\langle\sigma_v^2\rangle$ qualitatively corresponds to the width of the ridge in the velocity plot at a particular alpha lab angle. As can be seen in Fig. V-9, $\langle\sigma_v^2\rangle$ is fairly large at the forward angles and drops by an order of magnitude at the backward angles.

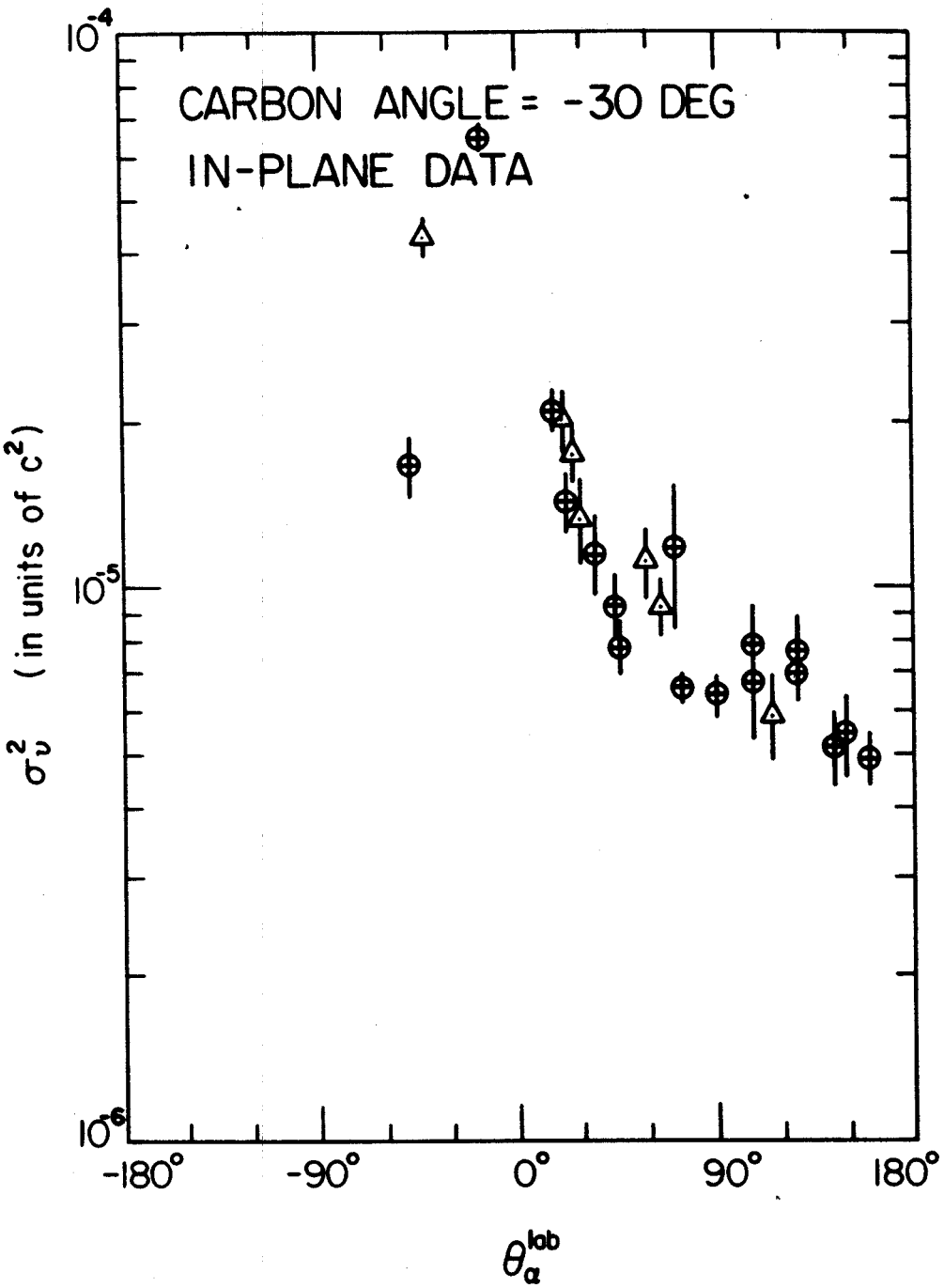

Fig V-9 The second moment of the velocity plot plotted as a function of the alpha lab angle for the in-plane data, θ_c=-30°. See Fig. V-4 for explanation of symbols.

The first moment which would correspond to the mean velocity is not plotted. The mean energy as a function of alpha lab angles will be discussed later. A corresponding quantity, the most probable carbon energy is plotted in Fig.V-10 as a function of alpha angle. At most angles this plot agrees with the observation by Harris el al. (Ha 77a) that the most probable excitation energy of $^{31}P^*$ remains fairly constant at 14.5 MeV over all of the angles measured.

2. Out-of-Plane Data, $\theta_c=-30^o$:

The total energy spectra and E_c vs. E_α 2D plots resemble those of the in-plane data. The data obtained are only reliable for $\phi_\alpha < 120^o$ because of the low alpha energy cut-off in the experimental system. As shown in Figs. V-11 and V-12, the C-α angular correlation function peaks strongly in the reaction plane ($\phi_\alpha=0^o$) in either the lab or $^{31}P^*$ center of mass system. In the $^{31}P^*$ center of mass frame, the C-α correlation drops to a minimum at about 90^o, lower than the minimum of the in-plane C-α correlation in Fig. V-6. Past $\phi_\alpha=90^o$ the C-α angular correlation rises up again. The contour plot shown in Fig. V-13 is very qualitative. The peak of the contours seems to lie close to the circle E which has the same diameter as the corresponding circle in Fig V-8 . Note that the $^{31}P^*$ velocity vector lies along $\phi_\alpha=0^o$ in this plot.

3. In-Plane Data, $\theta_c=-40^o$:

The energy spectra and 2D plots obtained from off-line analysis for this group of data are very similar to those at

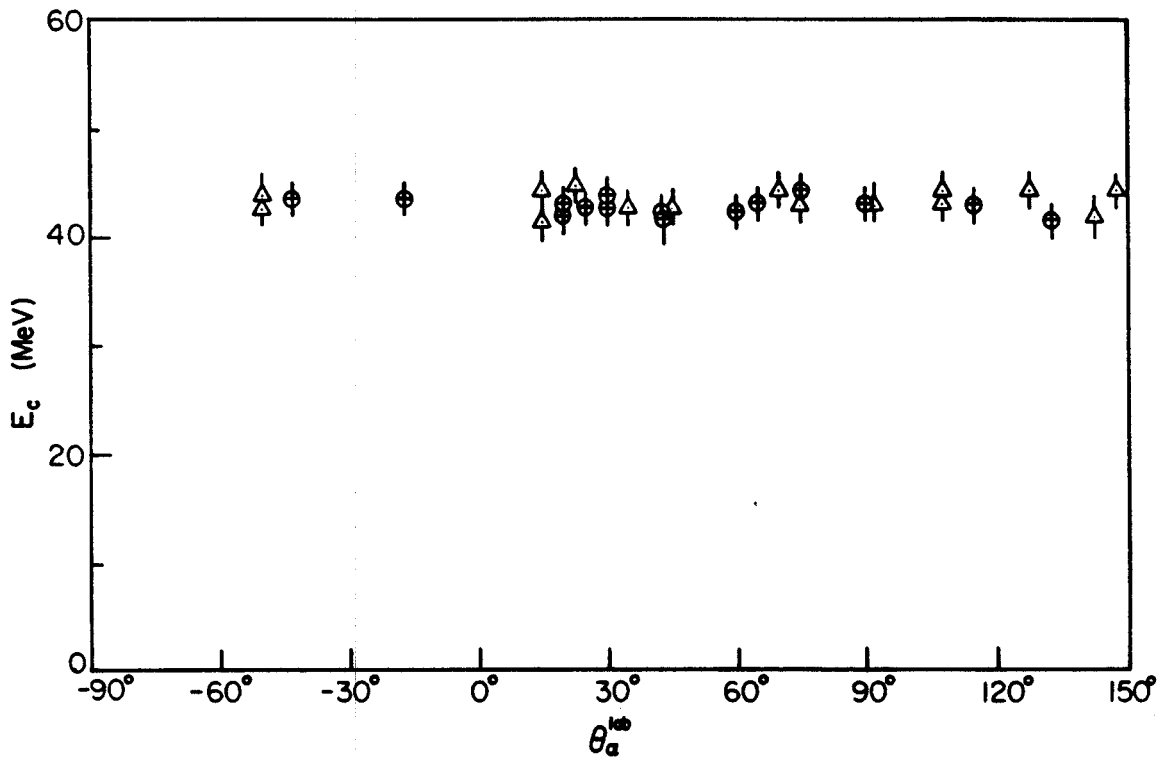

Fig V-10 The most probable carbon energy plotted as a function of alpha angles, θ_c=-30°, in-plane data.

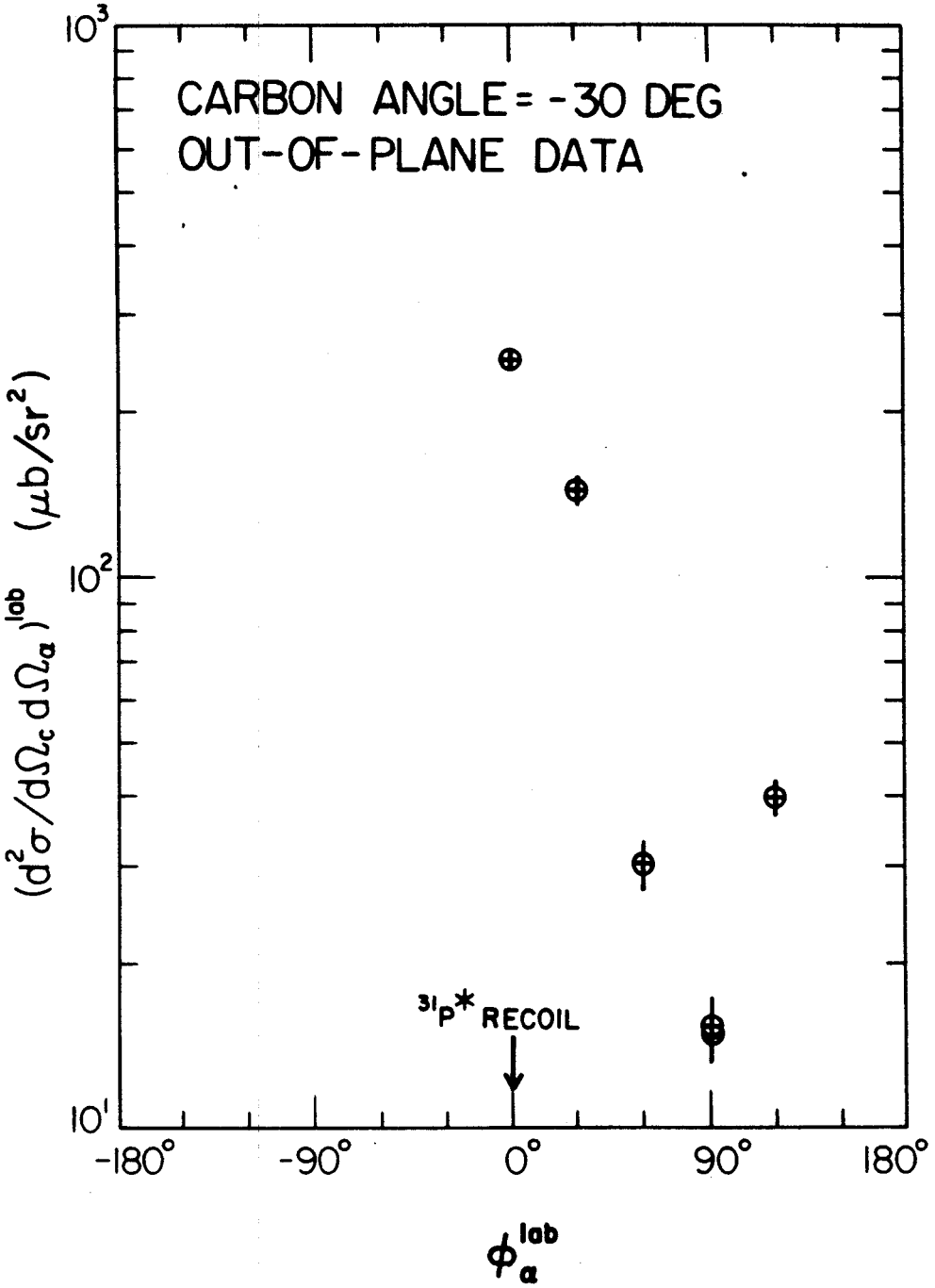

Fig V-11 Out-of-plane C-α angular correlation function in the lab system, θ_c=-30°, θ_{α}=43°. ϕ_{α} is defined to be 0° is the reaction plane.

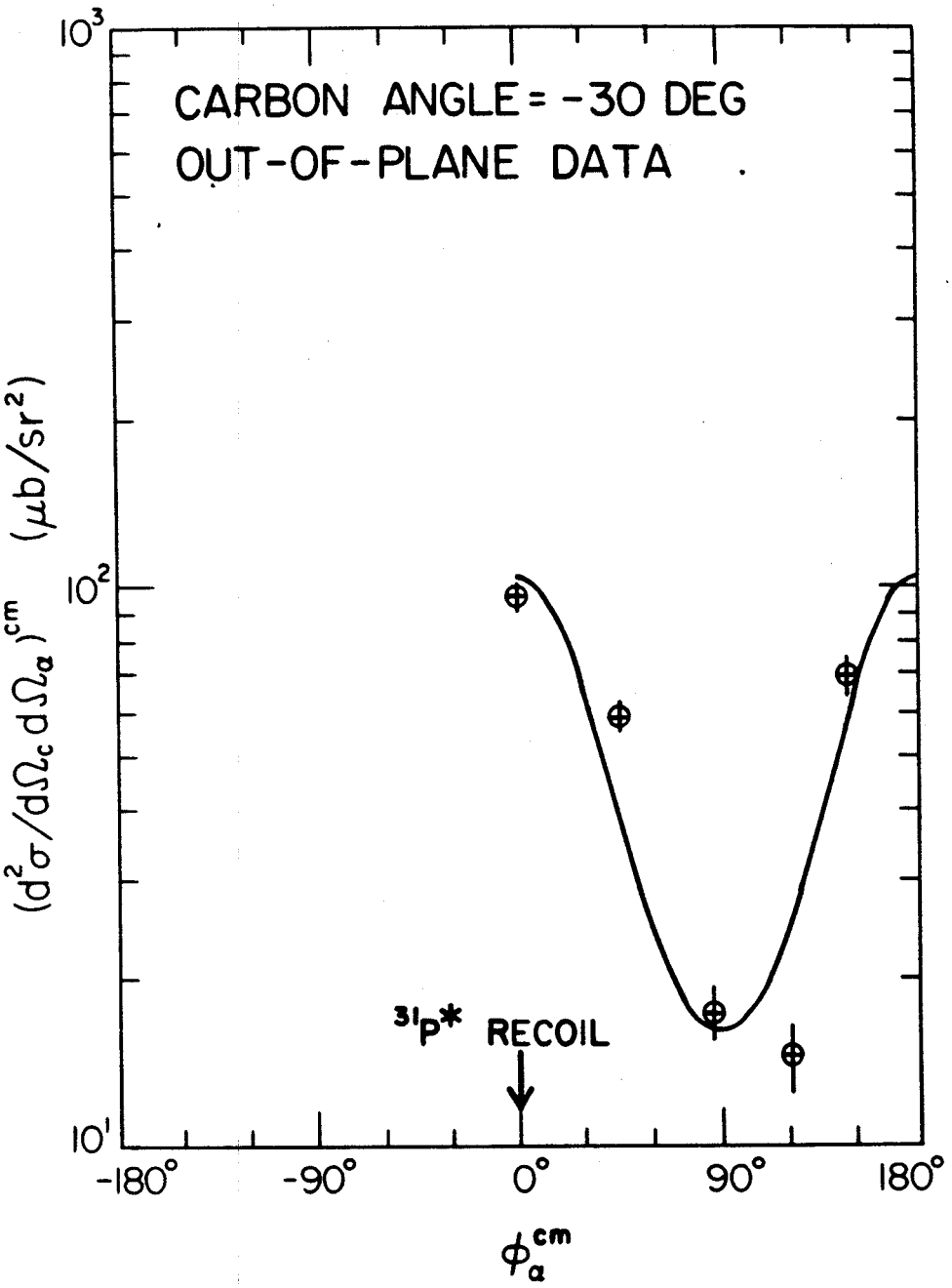

Fig. V-12 Out-of-plane C-α angular correlation function in the center of mass system of $^{31}P^*$, θ_c=-30°, θ_{α}=43°. The $^{31}P^*$ recoil direction in the reaction plane is defined to be ϕ_{α}=0°. The solid line is the best fit of Equation V-7.

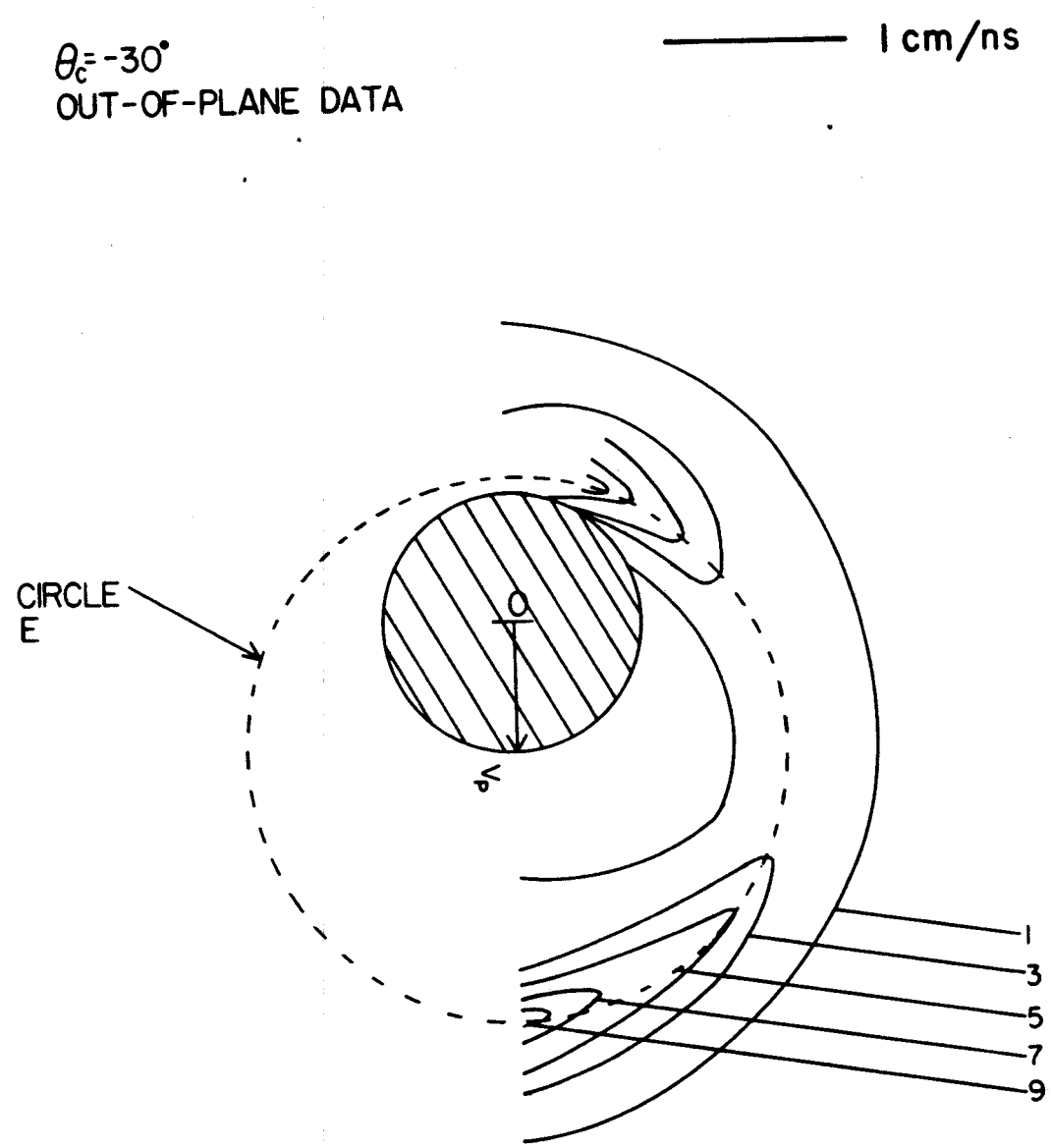

Fig V-13 Velocity contour plot for the out-of-plane data, θ_c=-30°. See Fig V-8 for explanation of symbols.

θ_c=-30°. Two groups of events corresponding to the Q=-7.16 MeV and Q=-11.59 MeV could be distinguished in an E_c vs. E_α plot. The most probable carbon energy for the C-α coincidence events with Q=-7.16 MeV remains constant at about 38 MeV for all of the angles measured. The corresponding $^{31}P^*$ excitation energy is about 14.5 MeV. Figs. V-14 and V-15 show the C-α angular correlation for the in-plane data at θ_c=-40°. The C-α angular correlation functions are very different from the ones obtained at θ_c=-30° shown in Fig. V-5 and Fig. V-6. The cross-section is a factor of two lower. The striking forward peaking towards the beam is absent. Instead, the C-α angular correlation exhibits only a slight peaking along the recoil direction of $^{31}P^*$. The most surprising feature in the C-α angular correlation plot in the center of mass system of $^{31}P^*$ is the strong rise at the backward angles on either sides of 0° The Jacobian as a function of alpha laboratory angles as shown in Fig. B.6 in Appendix B rises very steeply at angles greater than 120°. The strong backward angle rise of the correlation function in the center of mass system of $^{31}P^*$ may have been caused artificially by the Jacobian. However, the velocity contour plot shown on Fig. V-16 shows similar features with two strong peaks at the backward angles and at angles on the same side as the carbon telescope. The small peak in the recoil direction of $^{31}P^*$ remains.

4. Out-of-Plane data, θ_c=-40°:

The out-of-plane data at θ_c=-40° are plagued by the alpha particle low energy cutoff of the experimental system and the

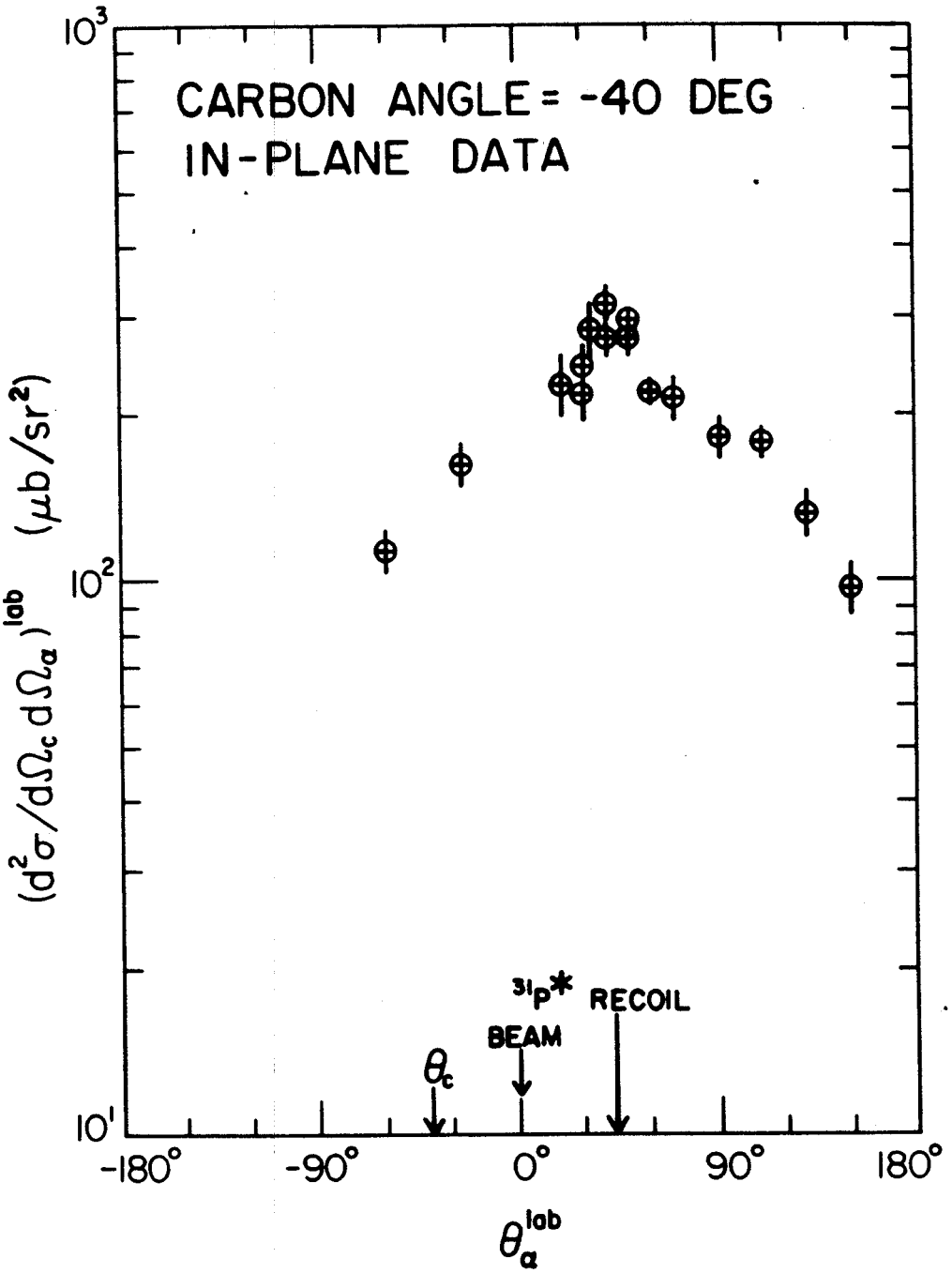

Fig. V-14 In-plane C-α angular correlation function in the lab system, θ_{α}=-40°.

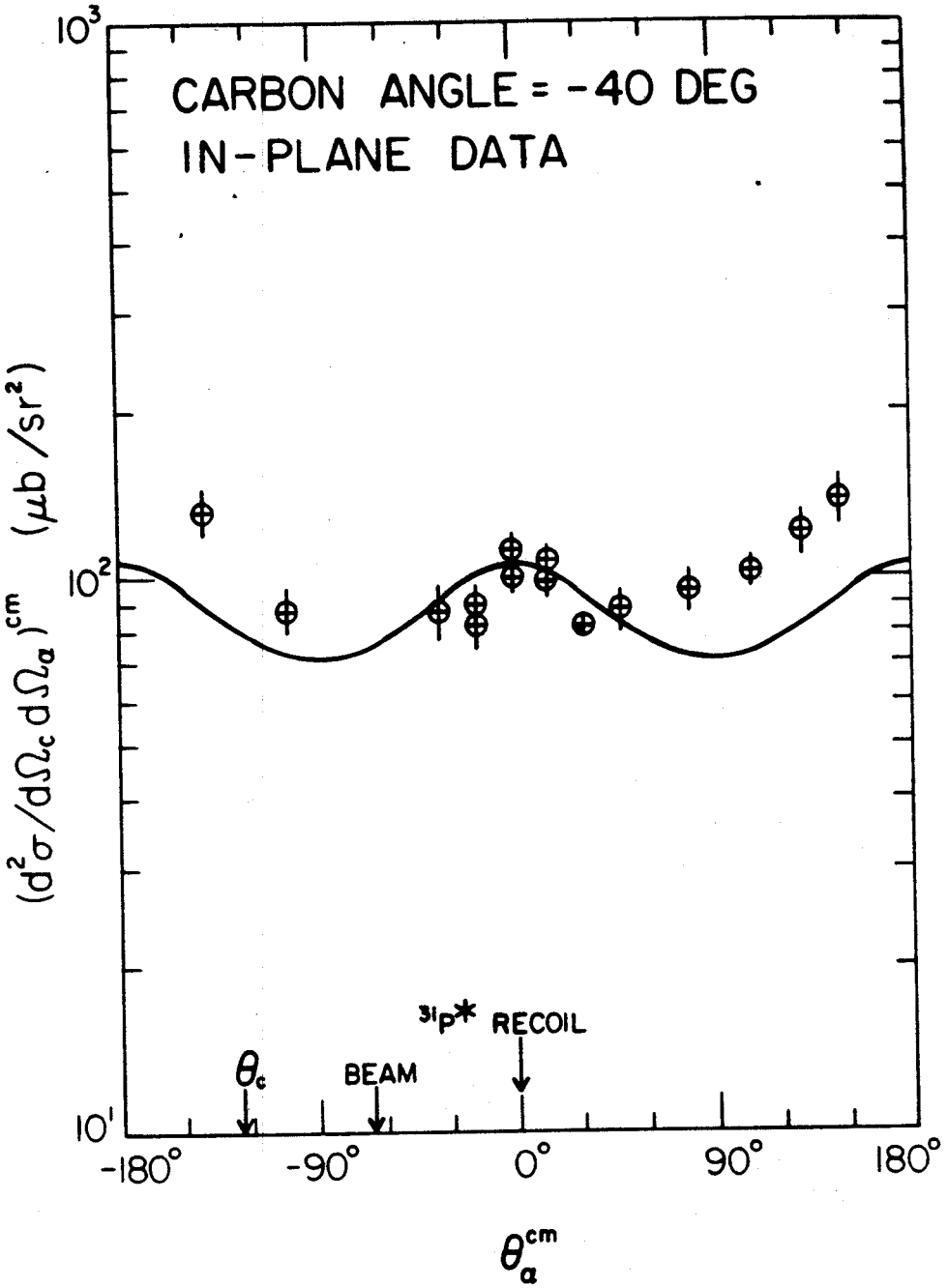

Fig. V-15 In-plane C–α angular correlation function in the ^{31}P* center of mass system, θ_c=-40° The solid line is the best fit of Equation V-7.

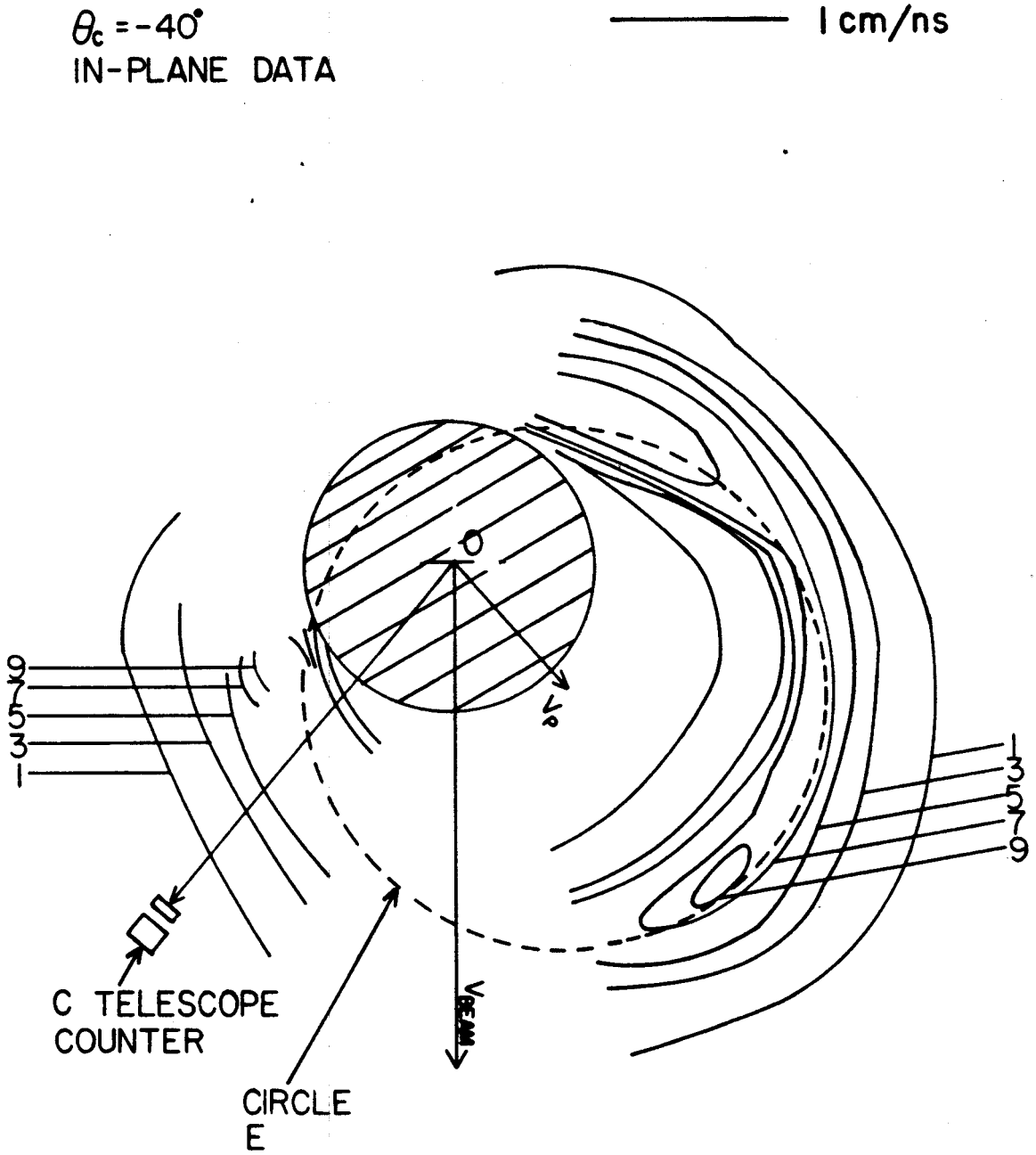

Fig. V-16 Velocity contour plot for the in-plane data, $\theta_c = -40^\circ$

See Fig. V-8 for explanation of symbols.

apparently very low cross-section away from the reaction plane. Reliable data were obtained only for four angles. Nevertheless, the C-α angular correlation both in the lab and in center of mass system peaks strongly towards the reaction plane as shown in Figs V-17 and V-18. Fig V-19 is the velocity contour plot. Aside from the cutoff, the general features of the velocity contour plot resemble those for the out-of-plane data at θ_c=-30^o.

B. Discussion

One of the goals of this dissertation is to understand the nature of the pre-equilibrium alpha emission process. In order to extract the pre-equilibrium component, all other processes that contribute to the alpha emission should be identified and subtracted.

1. Break Up Events from $^{16}O^*$:

The in-plane velocity contour plots of θ_c=-30^o data shown in Fig V-8 suggests that there are at least two groups of events, one that lies near the circle E which is centered on the velocity of the recoiling nucleus $^{31}P^*$ and another group with high alpha energy and low carbon energy. This latter group is observed only at θ_α=-17^o and -43^o. Since the second group of events seem to occur only around the carbon detector, this leads to the conclusion that these events probably arise from the break up of the inelastic scattered $^{16}O^*$. Such a mechanism can be represented as follows :

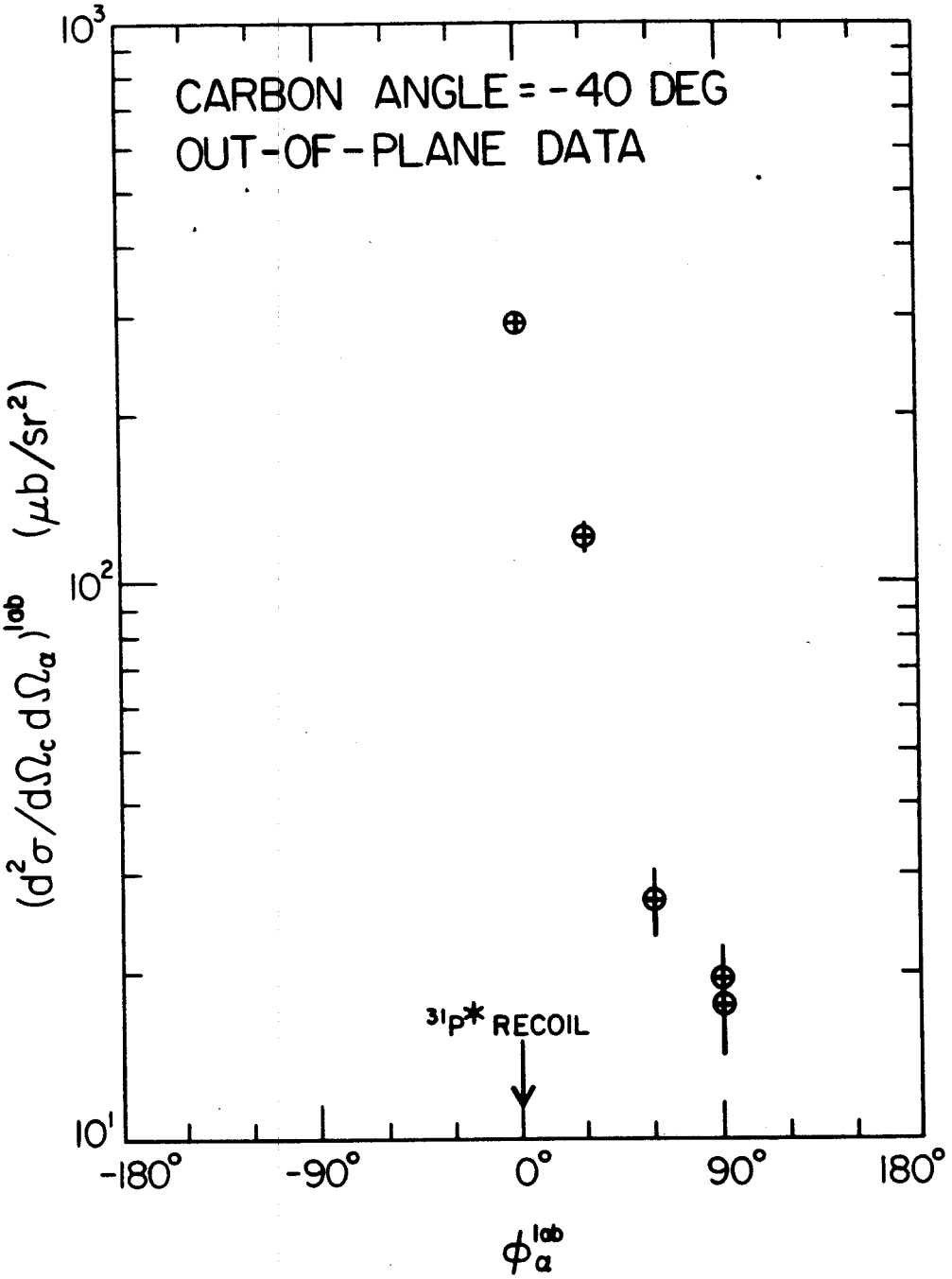

Fig V-17 Out-of-plane C-α angular correlation function in the lab system, $\theta_{\alpha x}$=-40°.

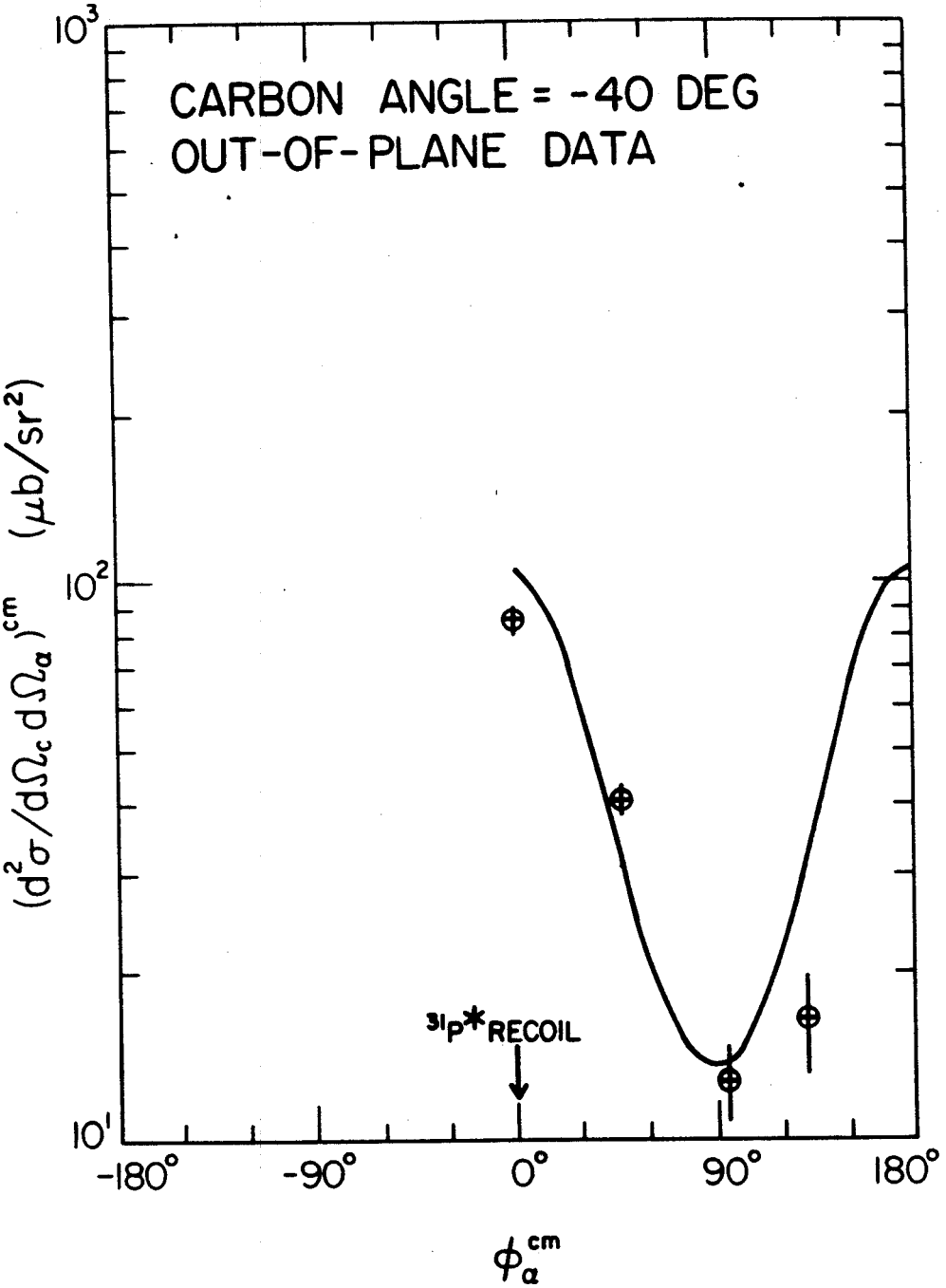

Fig. V-18 Out-of-plane C-α angular correlation function in the $^{31}P^*$ center of mass system, θ_c=-40°. The solid line is the best fit of Equation V-7.

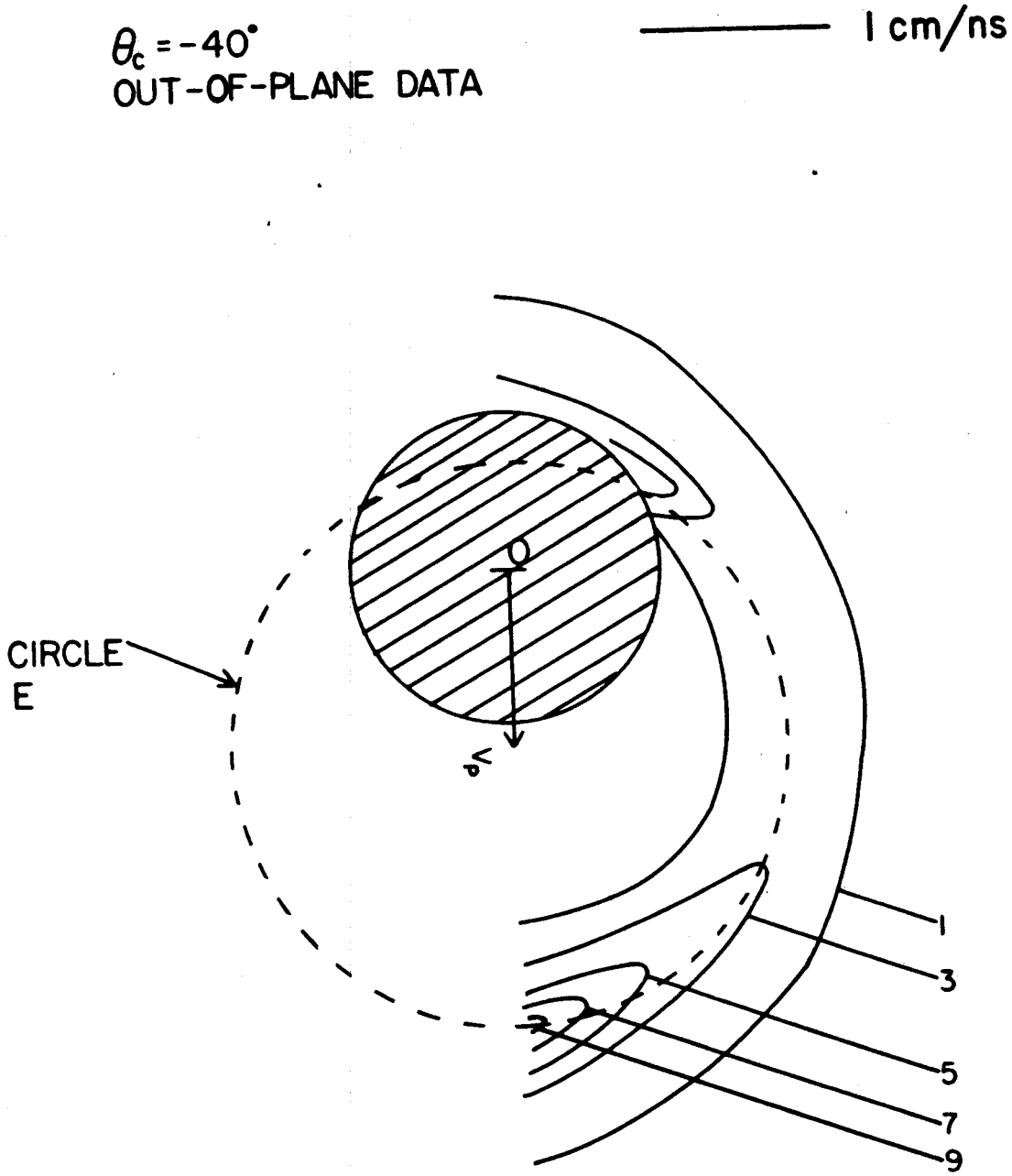

Fig V-19 Velocity contour plot for the out-of-plane data θ_c=-40° See Fig V-8 for explanation of the plot.

$$^{16}O + ^{27}Al \rightarrow ^{27}Al + ^{16}O^* \qquad V\text{-}1$$

$$^{16}O^* \rightarrow \alpha + ^{12}C \qquad V\text{-}2$$

The ^{16}O break up process has been observed by Ho et al (Ho 77) and more recently by Sasagase et al. (Sa 79).

If $^{16}O^*$ break up is an important process, two groups of C-α coincidence events will be detected at alpha angles close to the carbon detector. This can mostly easily be understood in the simple way described below. Suppose ^{16}O particles with a fixed excitation energy E_o are scattered to lab angle θ_o=-30°. Suppose that both the carbon and alpha particles are detected at the same angle -30°. In the $^{16}O^*$ center of mass frame, the carbon particles can be emitted either in the forward or backward direction along the ^{16}O trajectory. By conservation of energy and momentum, the carbon particles that are emitted forward which have high carbon energy (E_c) will be accompanied by alpha particles that are scattered in the backward direction with low alpha energy (E_α). Similarly, the other group will have low E_c and high E_α.

When the carbon and the alpha particles are detected at different angles, the situation is much more complicated. The two different kinematic groups discussed earlier correspond to break up of $^{16}O^*$ scattered at two different but unique angles. The velocity diagram for θ_c=-30° and θ_α=-17° with a fixed ^{16}O excitation energy E_o is shown in Fig. V-20. B is the origin of the lab frame. The beam direction is defined to be 0 degree. The two dashed lines at θ_c and θ_α correspond to the directions where the carbon and the alpha particles are detected respectively. The

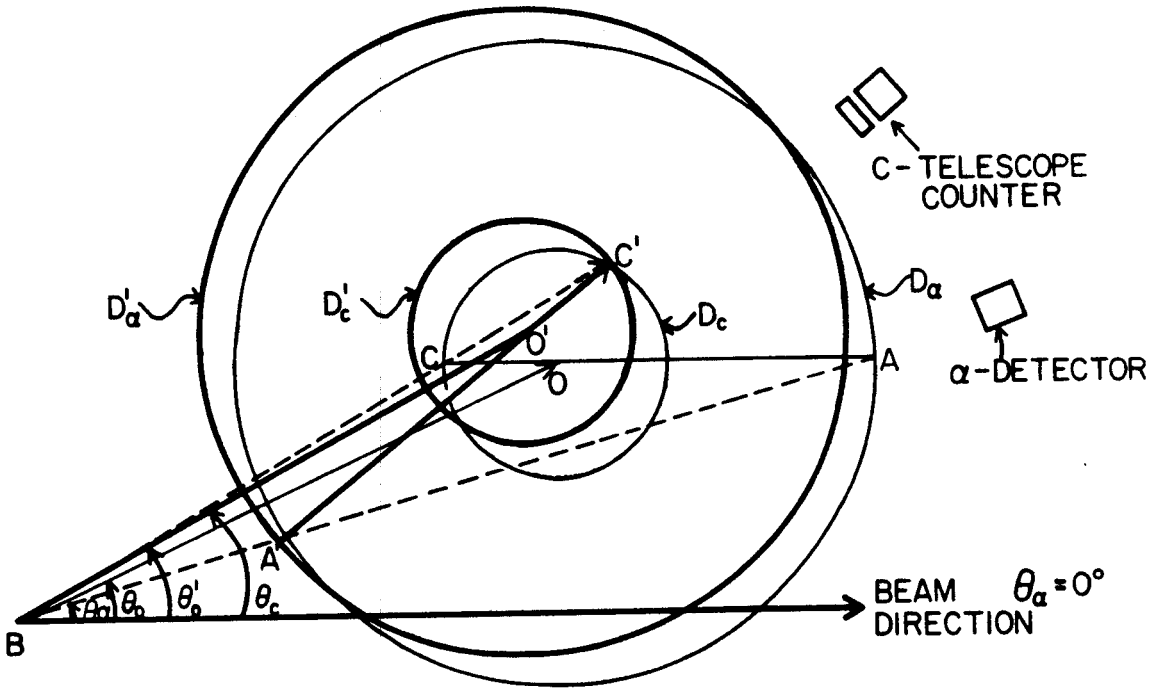

Fig V-20 Velocity diagram for $^{16}O^* \rightarrow {}^{12}C + \alpha$, $\theta_c = -30°$, $\theta_{\alpha'} = -17°$. See text for more detail explanation.

^{16}O nuclei with fixed excitation energy E_o must be scattered either to θ_o or to θ_o' determined from kinematics so that the carbon and alpha particles coming from the break up of the ^{16}O nuclei are detected at θ_c and θ_α. The kinematic group with high E_α and low E_c is represented by the unprimed system while the other group with low E_α and high E_c is given by the primed system. The velocity diagram for the unprimed group includes the two concentric circles D_c and D_α and the lines BO. OC and OA. These are drawn in light solid lines and circles. BO corresponds to the velocity of the oxygen scattered to the angle θ_o. O is the origin for the concentric circles D_c and D_α. The radii of D_c and D_α correspond to the center of mass velocity of the carbon and alpha respectively. By conservation of momentum, the carbon and alpha particles are emitted in opposite directions in the center of mass system of the $^{16}O^*$. This is indicated by the vectors OC and OA. In the lab system, the velocities of carbon and alpha are given by the vectors BC and BA.

If the ^{16}O is emitted at the other contributing angle θ_o' instead of θ_o, an exact analogue to the velocity diagram discussed in the preceeding paragraph can be applied with the center O displaced to O'. The circles D_c' and D_α' and the velocity vectors of ^{12}C and α in the ^{16}O center of mass system are shown as heavy circles and lines in Fig. V-20. The corresponding carbon and alpha velocities in the lab frame are given by the vectors BC' and BA'. From this analysis, if ^{16}O break up is a dominant process, then at a fixed oxygen excitation energy E_o and fixed θ_c and θ_α,

$$Y(\Psi)=Y_o \exp(X*\sin^2\Psi) \qquad \text{V-3}$$

where Y_o is the normalization factor and X is the ratio of rotational kinetic energy to the thermal nuclear energy.

$$X = .5\mu R^2 w^2/(2T) \qquad \text{V-4}$$

where μ is the reduced mass; w is the angular velocity and T is the nuclear temperature and R is the radius of the rotating nucleus.

$$R = 1.25(A_{\alpha}^{1/3} + A_{Al}^{1/3})$$

where A_i is the mass number for particle i.

X can also be expressed in terms of the spin (J) of the rotating nucleus.

$$X = .5(J+1/2)^2/(2IT) \qquad \text{V-5}$$

where $I=\mu R^2$ is the moment of inertia.

From the excitation energy of $^{31}P^*$ one can estimate the temperature with an empirical formula (Ro 67).

$$E = AT^2/11 - T + (A^{2/3}T^{7/3})/8 \qquad \text{V-6}$$

For the most probable excitation energy of $^{31}P^*$ of 14.5 MeV, the corresponding temperature is found to be 1.9 MeV.

Suppose the z axis is defined to be normal to the reaction

plane. Perfect alignment of the rotational axis along the z axis is expected only if the ^{16}O projectile and ^{27}Al target are point objects. In this case, the alpha particle that was transferred from ^{16}O to ^{27}Al is in the equatorial plane. Since both $\vec{r}_{\alpha}$ and $\vec{p}_{\alpha}$ lie in the equatorial plane, then the angular momentum transferred $\vec{\ell}_{\alpha}=\vec{r}_{\alpha} \times \vec{p}_{\alpha}$ is normal to the reaction plane.

In reality, the oxygen and aluminum nuclei have finite sizes, thus the alpha particle can be transferred slightly above and below the equatorial plane. However the average momentum transferred by the alpha particle is expected to lie in the reaction plane near the recoil direction of the composite nucleus $^{31}P^*$. The angular momentum of the $^{31}P^*$ then lies in the plane perpendicular to the momentum transfer direction. The angle between the rotational axis and the z axis is defined to be γ. The coordinate system used is shown in Fig. V-23. It is chosen to simplify the evaporation analysis and differs from that often used.

From the argument described above, the recoil direction is taken to be the momentum transfer direction. Experimentally, for sequential decay the momentum transfer direction has been found to lie very close to the recoil direction of the intermediate nucleus (Ei 73). Furthermore, the peak of the angular correlation cannot be determined to an accuracy of better than 30^{o} from the present data. Thus the above assumption would not greatly affect the contribution from equilibrium evaporation obtained using the formalism described.

In order to estimate the contribution of evaporation component in a simple way, γ is assumed to be gaussian distributed. A similar formalism has been employed by Dyer et al. to describe the in-plane and out-of-plane angular correlation of fission fragments from heavy product nuclei (Dy 79).

From Equation V-3, the angular distribution is

$$W(\theta,\phi) = \int d\gamma \exp[-\gamma^2/2\gamma_o^2] Y(\Psi) \qquad \text{V-7}$$

where Ψ is related to the angles γ, θ, and ϕ as shown in Fig V-22 by the cosine law:

$$\cos\Psi = \cos\gamma\cos\phi + \sin\gamma\sin\phi\sin\theta \qquad \text{V-7b}$$

The angular distribution $W(\theta,\phi)$ used in Equation V-7 is the same as the experimental quantity $(d^2\sigma/d\Omega_c d\Omega_\alpha)^{cm}$ of Equation IV-4a In order to emphasize the θ and ϕ dependence of this quantity, the more convenient notation $W(\theta,\phi)$ is adopted.

Both the out-of-plane data and the in-plane data are used to fit the two parameters γ_o and X. The dependence of Y_o, the normalization constant of Equation V-3 is eliminated by actually fitting the calculated ratio

$$\frac{W(\theta,\phi)}{W(0,90)} = \frac{\int_0^{2\pi} d\gamma \exp[-\gamma^2/2\gamma_o^2]\exp[X*\sin^2\Psi]}{\exp(X)\int_0^{2\pi} d\gamma \exp[-\gamma/2\gamma_o^2]} \qquad \text{V-8}$$

to the same ratio obtained experimentally.

Thus Y_o is an arbitrary normalization constant and cannot be obtained from the model described here. In this work, Y_o is

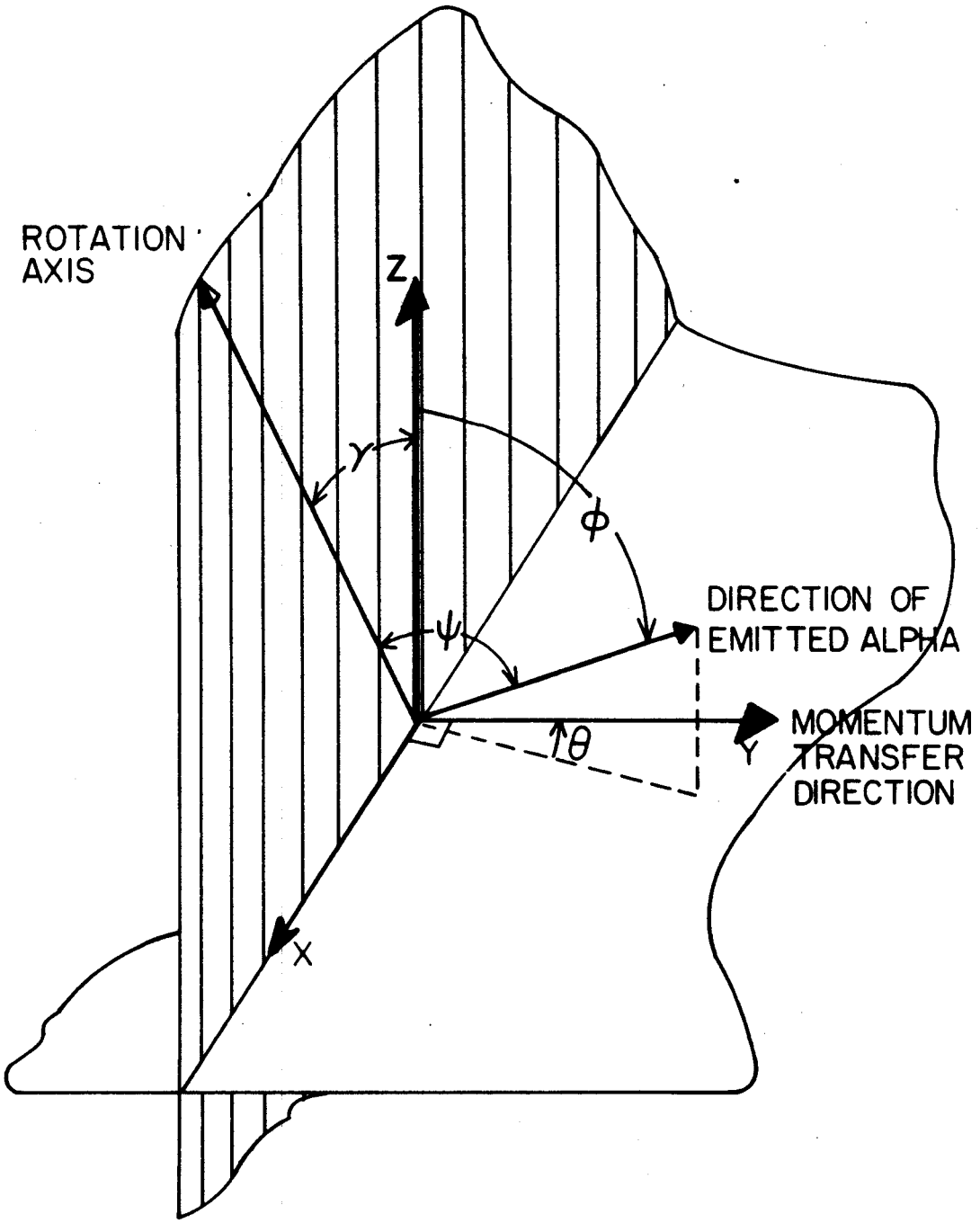

Fig. V-22 Coordinate system used in describing a rotating $^{31}P^{*}$ nucleus emitting an alpha particle. See text for more detail explanation.

obtained by adjusting $W(\theta,\phi)$ of Equation V-7 to the C-α angular correlation function plotted in the $^{31}P^*$ center-of-mass frame. Since the data has an uncertainty of 10% thus the calculated angular correlation function can lie between the two dashed curves shown in Fig. V-6. In Fig. V-6, Y_o for the solid curve is 110 $\mu b/sr^2$. Note that the quantity $\exp(X\sin^2\Psi)$ of equation V-3 is dimensionless.

The solid lines in Fig. V-15 and V-18 are the best fit of the in-plane and out-of-plane data for $\theta_c=-40^o$. Best χ^2 values for γ_o and X are found to be 28^o and 3.1 respectively The in-plane data is relatively featureless and would have been consistent with an evaporative origin if not for the rise at backward angles. The Jacobian at these angles rises very sharply as shown in Fig. B.2 in Appendix B. It is believed that the upward rise in yield at the backward angle may have been caused partly by this. It is unfortunate that more data is not available at these angles.

The solid lines in Figs. V-6 and V-12 are the best fit for the in-plane and out-of-plane data at $\theta_c=-30^o$. The best fit was obtained by using only backward angles ($\theta_\alpha^{cm} > 90^o$) in-plane data along with the out-of-plane data since the evaporative component is expected to dominate at backward angles. The γ_o and X values obtained are very close to those obtained for $\theta_c=-40^o$ data, $\gamma_o=28^o$ and X=2.6 Only the in-plane data from $-30^o < \theta_\alpha^{cm} < 0^o$ are not fitted by this purely evaporative model. All other angles are seen to be fitted very well by the simple evaporative angular

correlation.

Since γ_0 is a measure of dealignment of the rotational axis along the z axis normal to the reaction plane, thus $\gamma_0=28^o$ means that the dealignment is small. The rotational axis lies very close to the z axis. Following the argument on the angular momentum transfer by the alpha particle described above, one can obtain a very rough estimate of the maximum value of γ_0 by taking the inverse tangent of the ratio $R_{c-\alpha}/R_{c-Al}$. γ_{max} is found to be around 36^o. Thus the value of γ_0 obtained from fitting the experimental data closely resembles what one expects from a simple geometric argument. It is also interesting to note that γ_0 obtained in the present work is very close in value to the dealignment factor obtained by Dyer et al. (Dy 79) in describing the fission fragments from heavy product nuclei.

From the value obtained for X, one can estimate the mean spin of the rotating nucleus to be $\langle J \rangle \sim 7\hbar$ using Equations V-5 and V-6. The $\langle J \rangle$ value is large enough that one should be able to describe this system classically. However, since the measured alpha decay from the $^{31}P^*$ nucleus leaves the ^{27}Al in the ground state, the final ^{27}Al level density is too low for strict application of the statistical model. One should be cautioned against taking these statistical parameters $\langle J \rangle$ and T too seriously.

In addition, the equilibrium differential cross-section can be calculated with following equation :

$$(d\sigma/d\Omega_c)_{eq} = \int_o^{\pi} \sin\phi d\phi \int_o^{2\pi} d\theta W(\theta,\phi) \qquad \cdot V\text{-}9$$

$(d\sigma/d\Omega_c)_{eq}$ is found to be $790\ ^{+125}_{-75}$ ub/sr. From Equation IV-3, one can compute $(d\sigma/d\Omega_c)$ from the experimental data. This is found to be 6.5 mb/sr. Thus the ratio $(d\sigma/d\Omega_c)_{eq}/(d\sigma/d\Omega)$ is about .012. If one makes a comparison of this measured branching ratio to a crude statistical calculation, the results agree to within a factor of three.

3. Pre-equilibrium Contribution

Since the in-plane and out-of-plane C-α angular correlation at θ_c=-40° are consistent with evaporation, it can be assumed that the data discussed in this section was taken at θ_c=-30° unless otherwise specified.

As explained in the last section, the evaporative component was extracted by fitting Equation V-5 to the back angle data. The best fit is shown as a solid line in Fig. V-6. The dotted lines above and below the solid line represent upper and lower limits for the evaporative component by adjusting the normalization factor Y_o in Equation V-3. The pre-equilibrium alpha emission contribution is operationally defined here to be the experimental yield minus the yield from evaporation and the break up of $^{16}O^*$. It is plotted in the center of mass frame of $^{31}P^*$ in Fig. V-23. The corresponding lab angles are given on the top axis. Since the value of the Jacobian does not change very much over this range, the pre-equilibrium component would show very similar features in

the lab frame.

a. Differential Cross-Section:

The pre-equilibrium differential cross-section can be obtained by integrating the in-plane and out-of-plane angular correlation of the pre-equilibrium component. However, only one set of out-of-plane angular correlation was measured. This set of data indicates that the total alpha emission cross-section concentrate in the reaction plane. There is no quantitative out-of-plane information for the pre-equilibrium component. Nevertheless, one can make a rough estimate of pre-equilibrium component contribution to C-α coincident events with the available experimental information. The following assumption is made: The ϕ i.e. out-of-plane dependence of the pre-equilibrium angular distribution is the same as the ϕ dependence of the equilibrium angular distribution.

$$W_{pre}(\theta,\phi) = [W_{pre}(\theta,90^{o})/W_{eq}(\theta,90_{o})]\cdot W_{eq}(\theta,\phi) \qquad \text{V-10}$$

where $W_{pre}(\theta,90)$ is the extracted in-plane correlation function for the pre-equilibrium component as shown in Fig. V-23 and $W_{eq}(\theta,90)$ is given by the best-fit solid curve shown in Fig. V-6. The assumption used probably overestimates the contribution of the pre-equilibrium differential cross-section. Experimentally, the average alpha energy for the pre-equilibrium component is higher than the equilibrium component. Thus one would expect the angular momentum for pre-equilibrium alphas to be higher than the

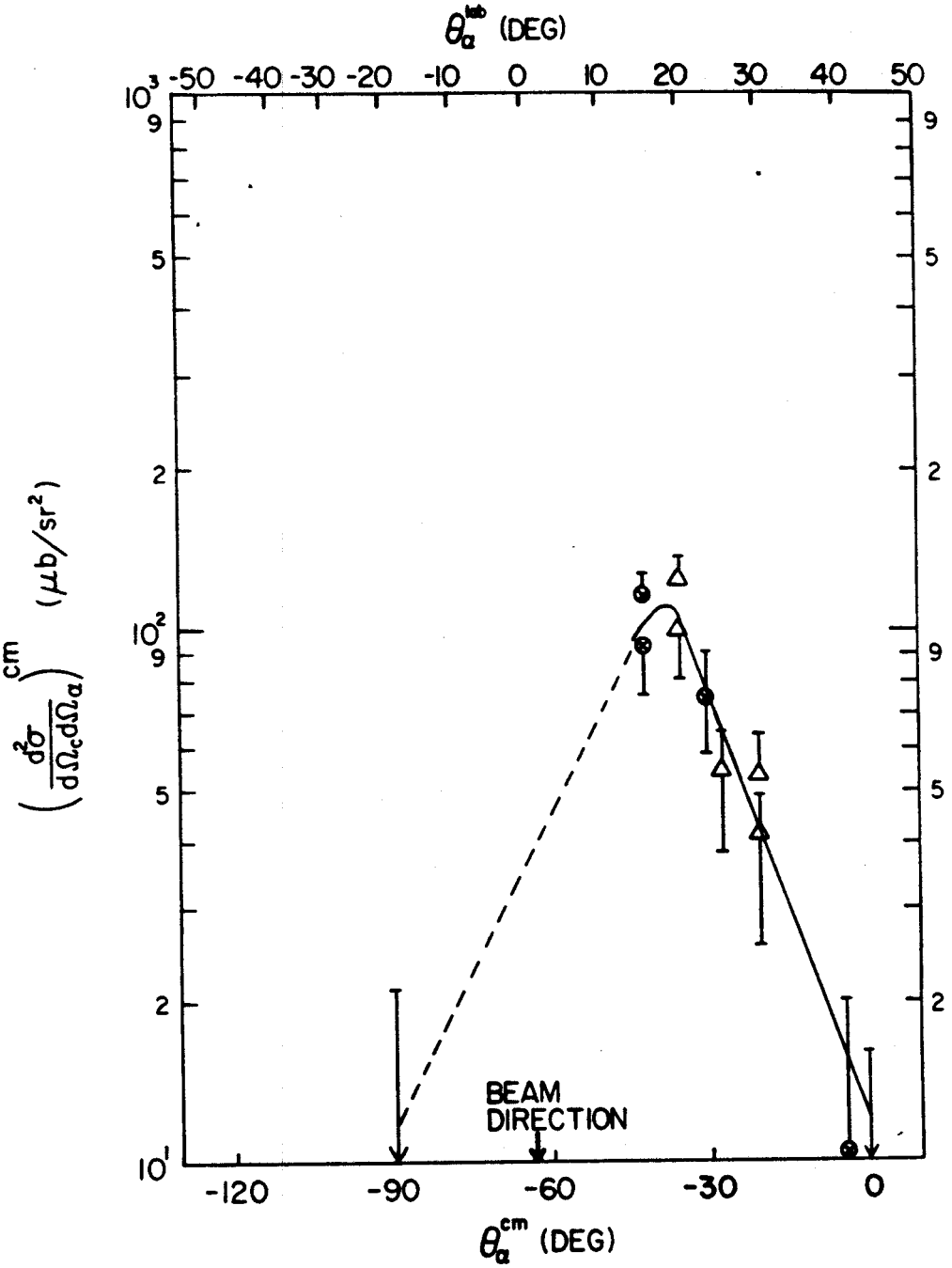

Fig V-23 Extracted pre-equilibrium alpha double differential cross-section plotted as a function of alpha angles in the $^{31}P^*$ center of mass system. The corresponding lab angles are also given.

equilibrium alphas and the ϕ dependence of the pre-equilibrium angular distribution might be steeper than that of the equilibrium component.

With the above assumption, one then obtains the ratio of pre-equilibrium contribution to the equilibrium contribution from the in-plane angular distribution.

$$\frac{(d\sigma/d\Omega_c)_{pre}}{(d\sigma/d\Omega_c)_{eq}} = \frac{\int d\Omega W_{pre}(\theta,\phi)}{\int d\Omega W_{eq}(\theta,\phi)} \simeq .1 \qquad \text{V-11}$$

The exact value of $(d\sigma/d\Omega_c)_{pre}$ depends on the exact ϕ dependence of $W_{pre}(\theta,\phi)$ and the exact shape of the dashed line shown in Fig. V-23 where no experimental data is available. The exact value of $(d\sigma/d\Omega_c)_{pre}$ is not important. It is used qualitatively to show that the pre-equilibrium component is small compared to the equilibrium one.

The break-up of $^{16}O^*$ contributes a very small fraction to the total C-α coincidence events detected experimentally and can be neglected. From the above analysis, the pre-equilibrium component contributes about 10% of the total C-α coincidence events detected experimentally. For the system of $^{27}Al + {}^{16}O$ at 65 MeV pre-equilibrium alpha emission is not the dominant mechanism for producing C-coincidence alpha particles as suggested by Harris et al. (Ha 77a).

b. Mean Alpha Energy:

The mean alpha energy in the center of mass frame of $^{31}P^*$

$\langle E_{\alpha}^{cm} \rangle$ is plotted as a function of alpha angle in Fig. V-24. The data points at the most backward alpha angles were excluded since they suffer from the low alpha energy cutoff problem as discussed in Chapter IV-F. Over most angles, $\langle E_{\alpha}^{cm} \rangle$ is constant as expected if the alpha particles come from the evaporation of $^{31}P^{*}$. For the forward angles where the pre-equilibrium alpha emission is important, $\langle E_{\alpha}^{cm} \rangle$ is much higher at these angles than the $\langle E_{\alpha}^{cm} \rangle$ obtained at the back angles. The mean alpha energy of the pre-equilibrium component for each alpha angle can be estimated in the following way :

$$\langle E_{\alpha}^{cm} \rangle = f \times \langle E_{\alpha}^{cm} \rangle_{pre} + (1-f) \times \langle E_{\alpha}^{cm} \rangle_{eq} \qquad \text{V-12}$$

where f is the fraction of pre-equilibrium alpha particles emitted. $\langle E_{\alpha}^{cm} \rangle_{eq}$ is the average energy for the equilibrium component and can be determined from Fig. V-24 to be $5.2 \pm .5$ MeV. This value can be compared to the calculated alpha energy of 4.2 MeV in the center of mass system if the alpha particle is emitted from $^{31}P^{*}$ nucleus with 14.5 MeV excitation energy. $\langle E_{\alpha}^{cm} \rangle_{pre}$ is the average energy for the pre-equilibrium alpha and can be determined from Equation V-9 and is found to be 8 ± 2 MeV. $\langle E_{\alpha}^{cm} \rangle_{pre}$ is found within the uncertainties to be angle independent at all alpha angles ($\theta_{\alpha}^{cm} = 15^{o}, 20^{o}, 25^{o}, 30^{o}$) where the pre-equilibrium component is present. The large error in $\langle E_{\alpha}^{cm} \rangle_{pre}$ is mainly due to the uncertainty in determining f.

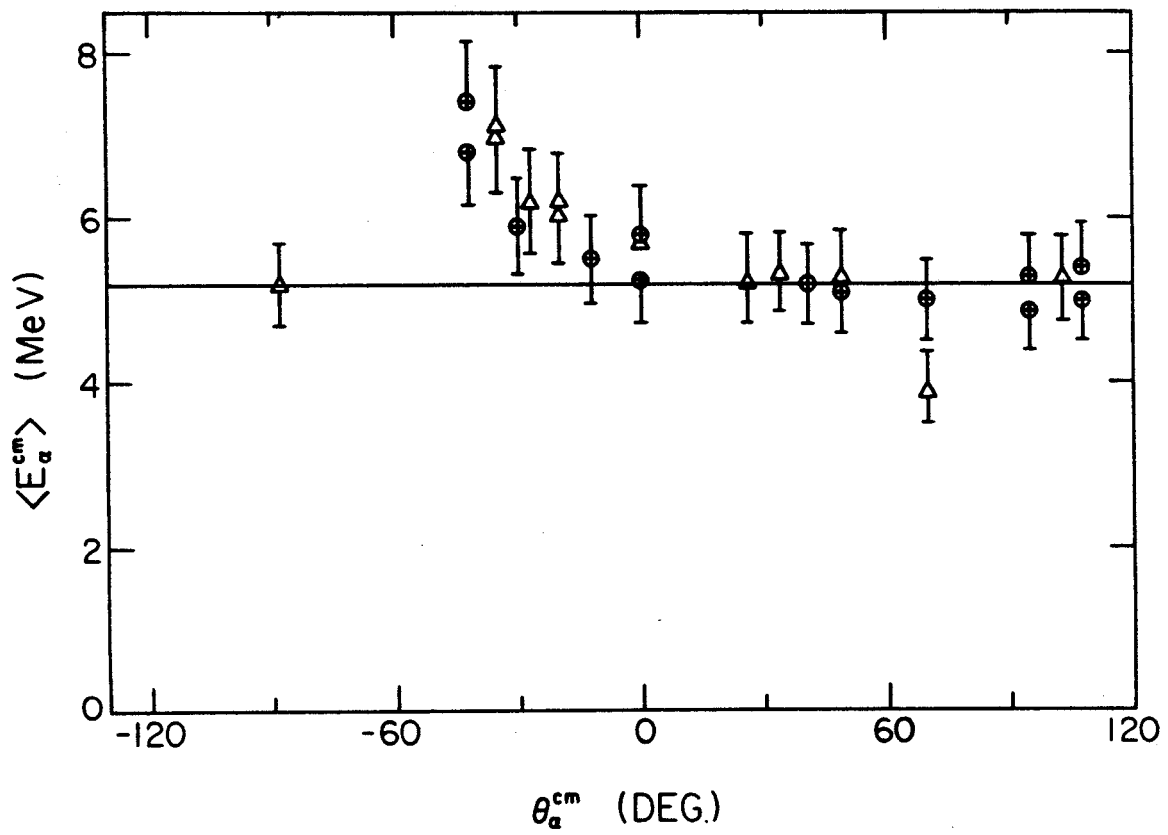

Fig. V-24 Mean α energy plotted as function of α angles in the $^{31}P^*$ center of mass system The straight line denotes $\langle E_{\alpha x}^{cm} \rangle$=5.2 MeV

c. Alpha Energy Spectrum:

Another way to extract the equilibrium component is shown below. Since the data at forward angles consists of events from pre-equilibrium alpha emission as well as events from evaporation of $^{31}P^*$, the properties of the pre-equilibrium component can be examined if the equilibrium component can be subtracted using the evaporation model developed in Section B of this chapter. In this model, the recoil direction of the $^{31}P^*$ is assumed to be the symmetry axis of the evaporative angular distribution. Both the yield and the energy spectra of the evaporated alpha particles should be symmetric with respect to the recoil direction of the $^{31}P^*$. This symmetry property can be used to subtract the evaporative component from the spectra at $\theta_{\alpha}=15^{\circ}$ 20°, 25° where the pre-equilibrium component is large. The alpha energy spectra shown in Fig. V-25a b c are plotted in the center of mass frame of $^{31}P^*$. The histograms composed of heavy solid lines are the measured alpha energy spectrum at alpha lab angles, 15°, 20°, 25° ($\theta_{\alpha}^{cm}=-42^{\circ}$, -35°, -27°). The energy spectra for the evaporative component are assumed to be the same as those measured at $\theta_{\alpha}=70^{\circ}$ 65° and 60° (θ_{α}^{cm} = 42°, 34°, 26°) respectively. These are plotted as light solid curve. Due to the poor statistics, all the alpha energy spectra are averaged over three channels. The error bars shown are purely statistical.

The dashed-dot curves are the pre-equilibrium energy spectra extracted by subtracting the equilibrium component from the total energy spectra. There is no a priori reason to plot the

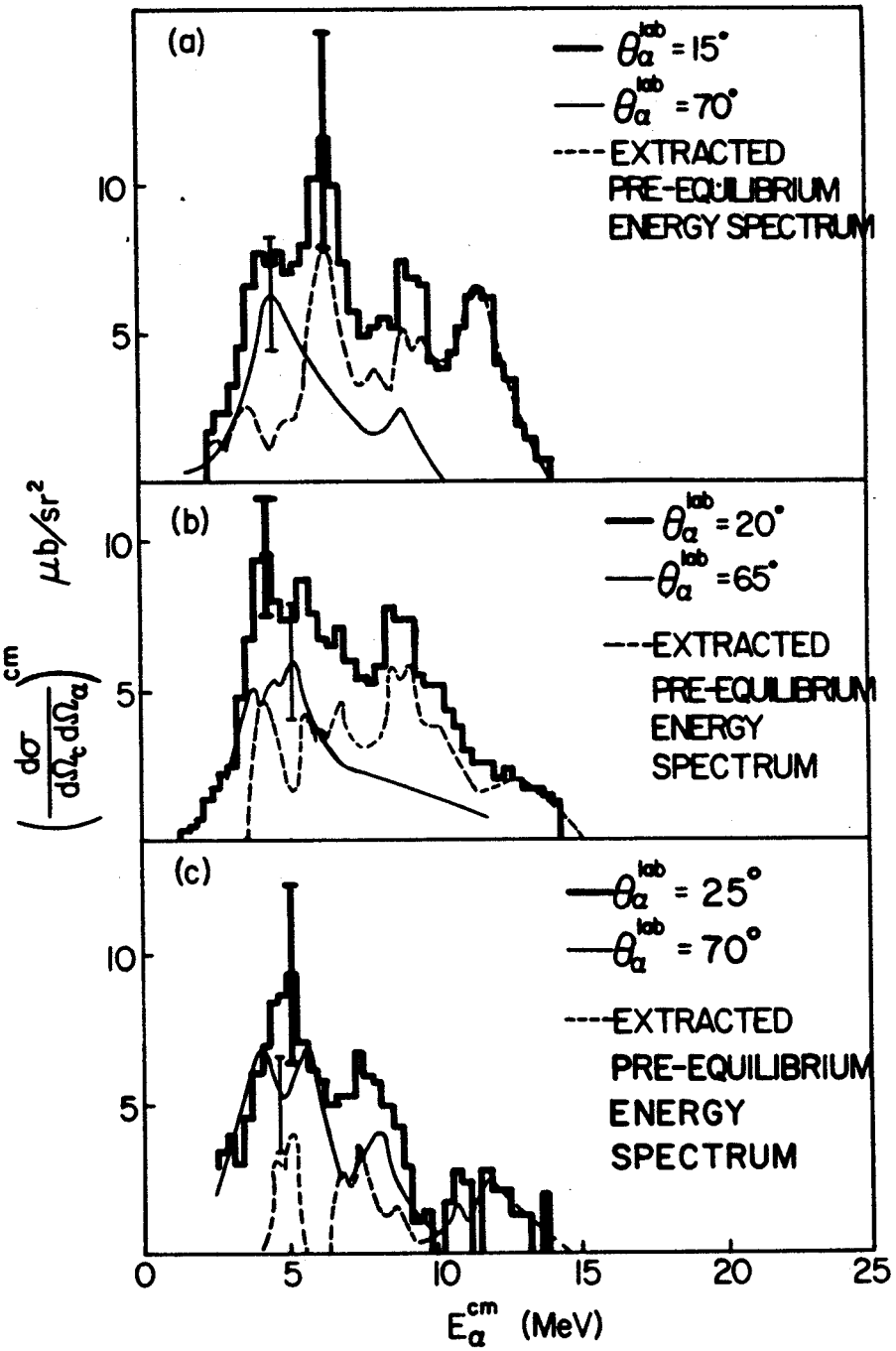

Fig. V-25 The raw alpha energy spectrum at forward angle denoted by the histogram its corresponding equilibrium α energy spectrum given by the thin curve and the extracted pre-equilibrium α energy spectrum indicated by the dashed curve. The corresponding error bars for each of the alpha energy spectrum is denoted by the vertical bars. a.) $\theta_{\alpha x}$=15°, b.) $\theta_{\alpha x}$=20° and c.) $\theta_{\alpha x}$=25°.

energy spectra of the pre-equilibrium events in the center of mass system of $^{31}P^*$. They have been transformed back to the lab system in Fig. V-26a,b,c The statistical error bars are very large, about 50% as a result of subtraction. Thus, one cannot say whether the structures these energy spectra exhibit is significant. The average alpha lab energy for the pre-equilibrium component is estimated to be 15 $\pm$ 3 MeV. Thus the corresponding velocity of the pre-equilibrium alpha particles is comparable to the beam velocity. However, it is much higher than the average alpha energy obtained from a three-body trajectory calculation described in Chapter VI. The calculated average alpha energy is found to be about 11 MeV.

The pre-equilibrium alpha energy for these forward angles are broadly distributed from 7 to 24 MeV in the lab reflecting the broadening of the velocity contour plots at the forward angles as shown in Fig. V-8. In Section A.1 of this chapter, it was shown that the most probable excitation energy of $^{31}P^*$ remained constant for most angles measured. This merely reflects the fact that the contribution from the evaporation of $^{31}P^*$ (E_x=14.5 MeV) is very important even at forward angles. There is no strong experimental evidence to support the assumption that the pre-equilibrium component comes from sequential decay of $^{31}P^*$ as suggested by Harris et al. (Ha 77a)

C. Comparison with Theoretical Models:

It is interesting to note that the pre-equilibrium

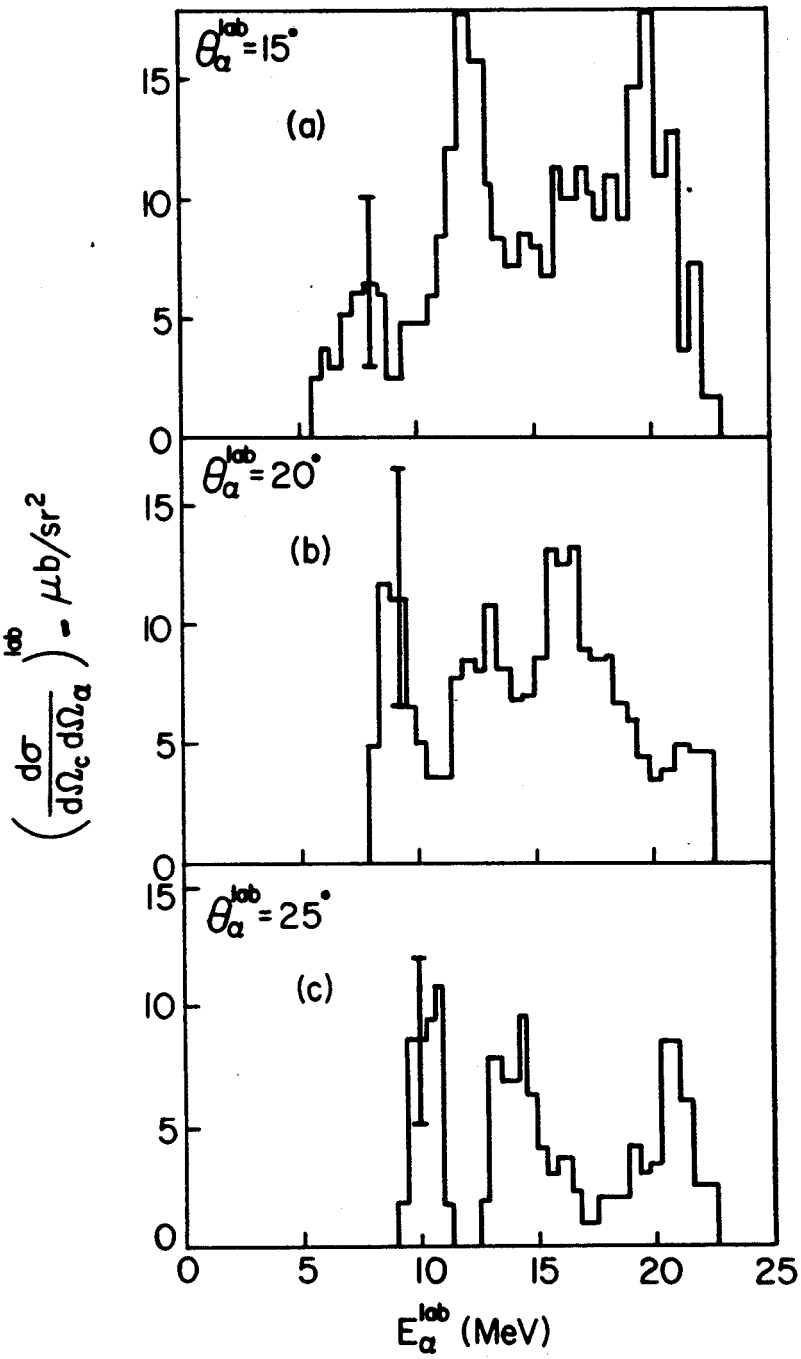

Fig. V-26 The extracted pre-equilibrium energy spectrum transformed to the lab frame a.) $\theta_{\alpha x}$=15°, b.) $\theta_{\alpha x}$=20° and c.) $\theta_{\alpha x}$=25°.

component is concentrated on the opposite side of the beam direction from the heavy ion detector. This qualitative feature of the experimental data can be compared to the "piston" or "hot spot" model briefly discussed in Chapter I-B-3.

In the "piston" model, the radial component plays an important role and the alpha particle is emitted from the opposite side from the point of impact. Thus, for quasi-elastic scattering i.e. when the heavy fragment particle follows a non-orbiting trajectory, the angular correlation of alpha particles and heavy fragment should peak on opposite sides of the beam as shown in Fig. I-1a. Up till now, this model still remains as a "theorist's speculation" and no careful calculation has been carried out. In the present experiment, if the carbon particles are assumed to be quasi-elastically scattered, then the experimental result seems to agree with the "piston" model. However, such identification of ^{12}C as quasi-elastically scattered is quite tentative and may easily be wrong.

Similarly the present experiment is not able to seriously test the "hot spot" model as described in Chapter I. Due to the low beam energy, nearly all events have either Q=-7.16 MeV or Q=-11.56 MeV. Contrary to the $^{58}Ni + ^{16}O$ experiment (Ho 77) which has a sizable cross-sections for events with large continuous negative Q values, very few events with $Q < -11.6$ MeV are observed in the present system. It is doubtful that any meaningful nuclear temperature of the $^{31}P^*$ intermediate component can be obtained from the alpha energy spectrum.

A trajectory calculation based on the "hot spot" model will be discussed in more detail in the next chapter. The model predicts that the projectile-like fragment will cast a shadow in the path of the alpha particles emitted from the "hot spot" formed in the target-like fragment. Thus, differential cross-sections for the alpha particles emitted are enhanced on either side of the direction of the projectile-like fragment with a deep valley, called the shadow region, around the projectile-like fragment. Ironically, this shadow region was not verified in the original experimental $^{58}Ni + ^{16}O$ since no data was taken in the shadow region. For the present experiment, enhancement of cross-section on one side of the carbon detector i.e. $-17^{o} < \theta_{\alpha} < 43^{o}$ has been established. A few data points are also available on the other side of the carbon detector with $\theta_{\alpha} < -43^{o}$. The differential cross-sections at $\theta_{\alpha}=-43^{o}$ and -50^{o} agree with those predicted by equilibrium evaporation within experimental uncertainties. Data were also taken at more backward angles, $\theta_{\alpha}=-65^{o}$ and -70^{o}. However, at these two angles, the group of events with Q=-7.16 MeV cannot be resolved from the group of events with Q=-11.59 MeV in a E_c vs E_{α} 2D plot. This problem is unique to these two angles and they are not included in the data presented in this dissertation since the events with Q=-7.16 MeV cannot be extracted unambiguously.

Even though the original "hot spot" calculation was done based on the assumption of a sequential process with the "hot spot" on the target like fragment, there is no a priori reason for

this assumption. A "hot spot" can be formed on the projectile just as well. The corresponding shadow region will be around the recoiling target-like fragment. Available experimental data only shows that the pre-equilibrium data are detected at forward lab angles $15^{o} < \theta_{\alpha} < 40^{o}$. The assumption that the correlation angular distribution should be symmetric about the shadow region would rule out a "hot spot" on the projectile since no pre-equilibrium alphas were observed for $56^{o} < \theta_{\alpha}^{cm} < 70^{o}$. However, if one relaxes this requirement, the "hot spot" model cannot be ruled out.

D. Summary

The result from the present work can be summarized as follow :

1. Very few if any pre-equilibrium alpha particles are detected in coincidence with carbon detected at $\theta_{c}=-40^{o}$. The C-α angular correlation function is consistent with that of alpha evaporation from $^{31}P^{*}$.

2. At $\theta_{c}=-30^{o}$, majority of C-α coincidence events come from evaporation of $^{31}P^{*}$. A small amount of alpha particles from the break up of $^{16}O^{*}$ are detected at angles around the carbon detector. Less than 10% of the alpha particles detected are of pre-equilibrium origin.

3. The pre-equilibrium alpha particle distribution extracted is forward-peaked on the opposite side of the beam

direction as the carbon detector.

4. The average velocity of the pre-equilibrium alpha particles is about the same as the beam velocity and the energy is much higher than the equilibrium alpha energy.

5. The present work does not give enough information to establish the mechanism for producing pre-equilibrium alphas.

CHAPTER VI

THREE-BODY TRAJECTORY CALCULATION

A. Introduction

The exit channel for coincidence experiments like the present work consists of an alpha particle and two other heavier residual fragments. The dynamics for these three particles in the combined Coulomb and nuclear field will be important to verify various alpha production mechanisms proposed. Thus simple classical three-body trajectory calculations have been performed by various groups (Go 78, Ga 78, Ha 78).

In general, the calculation is divided into three parts:

i. At t=0, i.e. when the calculation starts, two heavy fragments are assumed to interact in a pure two-body force field.

ii. At $t=t_o$, an alpha particle with kinetic energy E_α is emitted at some angle θ_α.

iii. For $t > t_o$, the trajectories of all three particles are calculated by numerically integrating Newton's equations of motions.

This type of calculation has had varying degrees of success in accounting for the data and three examples will be discussed below :

1. Hot Spot Model Calculation:

Gottschalk and Westrom proposed the "hot spot" model in connection with the coincidence experiment $^{58}Ni + ^{16}O$ at 96 MeV

(Go 78, Ho 78). In their calculation, the following sequential process is assumed. A hot spot is created on the surface of the target-like fragment which lies in the combined nuclear and Coulomb field of the target and projectile during the interaction. This hot spot can either decay by internal diffusion or by pre-equilibrium alpha emission with a certain probability $P(E_{\alpha},\theta_{\alpha},t)$ where E_{α} is the kinetic energy of the alpha particle and θ_{α} is the emitted angle. After the emission, the trajectories of the three particles are calculated by treating them as point charges. The presence of the nuclei is taken into account by assuming that the alpha particle is absorbed if it passes through the central density region of either one of the residual nuclei.

The alpha particle emission probability $P(E_{\alpha},\theta_{\alpha},t)$ is related to the surface temperature (T) of the excited target.

$$P(E_{\alpha},\theta_{\alpha},t) = E_{\alpha}\exp[(-E_{\alpha} + E_b)/T] \qquad \text{VI-1}$$

where E_b is the binding energy of the emitted particle. The difference in surface temperature between the initial localized hot spot and the rest of the target nucleus leads to two modes of alpha emission, the "fast" and "slow" mode. This agrees with experimental observation if one identifies the slow mode with the equilibrium evaporation from the target-like fragment and the fast mode with the pre-equilibrium alpha emission. The calculated angular distribution of the fast mode exhibits strong peaking on both sides of the heavy ion detector. The valley between these two peaks is termed the "shadow region". It arises from the fact

that the alpha particle is absorbed whenever it comes close to the heavy ion. Another way to understand the origin of the "shadow region" is that the heavy ion casts a "shadow" in its path.

2. Pure Coulomb Three-Body Trajectory Calculation:

Gamp et al. performed a three-body model calculation to understand the origin of the pre-equilibrium alpha emission from the system $^{197}Au + ^{32}S$ at 373 MeV (Ga 78). The ^{32}S particle is assumed to move along the Rutherford trajectory until the distance of closest approach is reached. At this point, an alpha particle is supposed to be emitted from the ^{32}S nucleus at an emission angle θ_{cm} in the center of mass system of ^{32}S with kinetic energy E_{α}. The final trajectories of the three bodies, α, ^{28}Si and ^{197}Au are computed for all possible in-plane emission angle by taking into account of Coulomb forces only. The impact parameter was chosen such that the heavy fragment (^{28}Si) is scattered to 35^{o} (experimental heavy ion lab angle). An initial kinetic energy E_{α} of 0 MeV gave the best final results. By calculating trajectories with various θ_{cm}, the alpha particles were found to peak at lab angles $\theta_{\alpha}=15^{o}$ and 60^{o}: i.e. on either side of the heavy ion detector due to Coulomb focusing. Experimentally, only the more forward peak ($\theta_{\alpha}=15^{o}$) close to the beam is observed. This leads to the conclusion that the pre-equilibrium alpha particles originate in the region of the projectile which is facing the target nucleus during the collision.

3. Three-Body Classical Friction Model:

In his thesis (Ha 78), Harris developed a two-body

classical friction model to fit the inelastic data in various light heavy ion systems such as $^{27}Al + ^{16}O$ at 100 MeV and $^{58}Ni + ^{16}O$ at 92 MeV. This model was extended to perform a three-body calculation in the reaction $^{27}Al(^{16}O,^{12}C\alpha)^{27}Al$ at 65 and 100 MeV (Ha 78). In the two-body classical friction model, in addition to the Coulomb and nuclear forces, a frictional force is also present. The frictional force takes into account the energy loss observed in deeply inelastic scattering and is assumed to be proportional to the instantaneous relative velocity ($\dot{r}$),

$$F_{frict}(r) = K\int \rho_1(\tau)\rho_2(\tau-r)\dot{r}d^3\tau \qquad \text{VI-2}$$

where ρ_1 and ρ_2 are the densities of the target and projectile. K is a friction coefficient and is obtained by fitting inelastic scattering data.

In the three-body trajectory calculation, the target and projectile are first assumed to move along the trajectory prescribed by the classical friction model until the two nuclei reach the distance of closest approach. Then the alpha particle is emitted from the overlapping region of the two fragments with a velocity equal to the fragment velocity. The two heavier residual fragments follow trajectories prescribed by the friction model and are assumed not to be disturbed by the existence of the alpha particle. On the other hand, the alpha particles moves in the nuclear and Coulomb force field of the remaining fragments. The results of the calculation is very sensitive to the choice of the initial conditions.

This calculation has been performed on various systems. An impact parameter is chosen so that the heavy ion is scattered to the experimental heavy ion angle dictated by the two-body friction model. Various values of E_{α} and θ_{α} are used as input conditions. For a few systems especially the heavy systems, this model reproduces the most likely angle and energy of the alpha particles observed experimentally for some input values of E_{α} and θ_{α}.

In these three previous calculations, simplifications have been introduced which lead to serious gaps in an overall explanation of the pre-equilibrium alpha decay mechanism. Except for the "hot spot" model, they all fail to explain the origin of alpha particle. In the case of the hot spot model, no attempt is made to understand the exact mechanism of the formation of the hot spot in the target. Only the Coulomb force is considered in most cases. In the case of the classical friction model, only the alpha particle experiences three-body forces. The trajectories of the other fragments are calculated using the two-body friction model ignoring the presence of the alpha particle. In order to reproduce the heavy ion detection angle, the presence of the alpha particle is ignored in most of the calculations so that an impact parameter can be obtained by considering the two-body force only. The initial alpha energy and emitted angle are artificially input into the calculation at $t=t_o$ when the alpha particle is created. The results obtained cannot be taken too seriously since not all possible initial conditions are taken into account. The nuclear force may not be very important for very heavy systems like

$^{197}Au + ^{32}S$. However, for the lighter systems, $^{27}Al + ^{16}O$ and $^{58}Ni + ^{16}O$, the nuclear force will play an important role in determining the final results.

In the present experiment, only the alpha particles associated with a total 3-body reaction with Q=-7.16 MeV are considered: i.e. the final reaction products ^{27}Al, ^{12}C, and α are in their ground states. To simplify the calculation, the following assumption is made: The reaction is assumed to proceed without any internal excitation of the fragments at any stage of the reaction. This has a very nice feature that no residual excitation or other energy loss mechanism has to be explained by inclusion of a frictional force as in the case of the classical friction model. In addition, the most probable velocities of both the carbon and alpha particles for the non-evaporative component are very close to the projectile velocity. This leads to the assumption that the alpha particle originates in the projectile and thus the oxygen is represented as a classical bound system of a ^{12}C and an alpha particle. Even though the ^{16}O is known to have a high parentage of its configuration with ^{12}C in the 2^+ (4.43 MeV) excited state (De 73b), this configuration of ^{16}O is neglected for the present calculation. Both Woods-Saxon and proximity potentials have been used as nuclear potentials in the calculation. The impact parameter for the oxygen projectile and parameters describing the relative orientation of the C-α bound system are chosen by a Monte Carlo routine. Within the constraints of the previous assumptions, the present calculation

is thus a complete and consistent classical description of the break up process. In the next two sections, the program that performs the present calculation will be described in detail.

B. Description of the Present Three Body calculation

In this calculation, it is assumed that before the nuclear collision the ^{16}O projectile moves along the Rutherford trajectory until a relative distance between ^{16}O and ^{27}Al of 15 fm is reached. At 15 fm the three body calculation is started with the ^{16}O nucleus described as a bound system consisting a ^{12}C and an alpha particle. The motion for the three nuclei ^{12}C, α and ^{27}Al under the influence of both Coulomb and nuclear two-body forces is calculated numerically. The three-body calculation is terminated when the carbon particle has moved more than 100 fm from the point where the ^{16}O was first described as a ^{12}C, α bound system.

Newton's Equations of motions are :

$$dX_{ij}/dt = V_{ij} \qquad \text{VI-3}$$

$$m_i dV_{ij}/dt = F_{ij} \qquad \text{VI-4}$$

where the subscript i denotes the i^{th} particle and the subscript j is the j^{th} coordinate. X_{ij}, V_{ij}, and F_{ij} denote the j^{th} component of position, velocity and force vector for the i^{th} particle with mass m_i and t is the time.

The force field F between two particles i and k includes

both the Coulomb and nuclear force which are central forces. For convenience in the discussion, the force term will be expressed in terms of polar coordinates.

$$F(r) = -d/dr[U^{c}(r) + U^{nucl}(r)] \qquad \text{VI-5}$$

$$F_{ij} = -\nabla_{j}\sum_{k} U_{ik}(|\vec{r}_i - \vec{r}_k|) \qquad \text{VI-6}$$

where $r=|r|=|r_i-r_k|$ is the relative distance between two particles. U^{c} is the Coulomb potential and U^{nucl} is the nuclear potential.

If n denotes the n^{th} time interval in the calculation, the position and velocity for the particles at the $(n+1)^{th}$ time interval can be computed by the Newtonian law of motion.

$$X_{ij}^{n+1} = X_{ij}^{n}\Delta t + F_{ij}^{n}(\Delta t)^{2}/2m_i \qquad \text{VI-7}$$

$$V_{ij}^{n+1} = V_{ij}^{n} + F_{ij}(\Delta t)/2m_i \qquad \text{VI-8}$$

where $t_{n+1} = t_n + \Delta t$

The Coulomb potential used has the following form

$$U_{ik}^{c}(r) = \begin{cases} Z_i Z_k e^{2}/r & r > R \\ Z_i Z_k e^{2}[(R^{2}-r^{2})/2R^{3} + 1/R] & r < R \end{cases} \qquad \text{VI-9}$$

where Z_i and Z_k are charges of the nuclei i and k respectively; R

denotes the the radius before the two nuclei just touch.

Two different forms of nuclear potential have been used : the Woods-Saxon potential and the proximity potential.

1. Woods-Saxon Potential :

The Woods-Saxon Potential has the following form

$$U_{ik}^{nucl}(r) = -U_{ik}/[1 + \exp((r-R_{ik})/a_{ik})] \qquad \text{VI-10}$$

where U_{ik}, R_{ik}, and a_{ik} are the real potential depth, radius and diffuseness respectively for the nuclear potential between particles i and k. Three different sets of parameters of U_{ik}, R_{ik} and a_{ik} have been tried. They are described below and tabulated in Table VI-1.

i. For the C-α nuclear potential, $R_{c-\alpha}=1.25*(12^{1/3}+4^{1/3})$, $a_{c-\alpha}=.65$ are used as the Woods-Saxon radius and diffuseness. This same set of parameters has been used by DeVries to describe "pre-formed" alpha cluster states in (^{16}O,^{12}C) alpha transfer reactions (De 73a). The remaining parameter, $U_{c-\alpha}$, is obtained by setting the calculated root mean square radius for C-α, $\langle r_{c-\alpha}^2\rangle^{1/2}$, with $\langle r_{c-\alpha}^2\rangle = \int r^2 dt/dt$ to be the same as $\langle r_{c-\alpha}^2\rangle^{1/2}$ obtained from the experimental charge radii of ^{16}O, ^{12}C and α. The formalism is derived in Appendix C.

ii. R_{Al-C}, a_{Al-C} and U_{Al-C} are obtained from Da Silverira et al. (Ds 75) by fitting the elastic and inelastic scattering data of $^{27}Al + ^{12}C$ at 46.5 MeV.

iii. For the case of Al-α, various different sets of optical potential parameters all of which fit the experimental

scattering data at different incident energies can be found in the Atomic Data and Nuclear Data Table (Pe 76). Three different parameter sets with very different $R_{Al-\alpha}$, $a_{Al-\alpha}$ and $U_{Al-\alpha}$ values were used (Br 67, Ke 72).

These three sets of Woods-Saxon potential parameters are only three of many sets of Woods-Saxon parameters that fit some elastic data and could be used in the three-body calculation. This is an undesirable feature since the results of the calculation will be seen to be very sensitive to the choice of R_{ik}, a_{ik} and U_{ik}. Thus it is advantageous to use a universal potential with a minimum of adjustable parameters, an example of which is the proximity potential discussed below.

2. The Proximity Potential :

The proximity potential has been used successfully to describe heavy ion elastic scattering. Only a brief description and the recipe for obtaining this potential is given below. A detailed discussion of the proximity potential and references for the semi-empirical formulae used to obtain different variables (Eqs. VI-12 to VI-15) can be found in an article by Blocki et al. (Bl 77).

For systems with large mass and thin skin region the proximity force theorem derived by Blocki et al. states that the force between two rigid gently-curved surfaces separated at a distance s is proportional to the interaction energy per unit area e(s) between two parallel surfaces. The proximity force is given by

$$F_{ik}(s) = 2\pi[C_iC_k/(C_i+C_k)]e(s)$$

VI-11

where C_i is the central radius of particle i and is given by the following equation :

$$C_i = R_i[1 - (b/R_i)^2 + \ldots]$$

VI-12

where Ri is the equivalent sharp radii and is related to the mass number A_i by the following expression

$$R_i = 1.28A^{1/3} - 0.76 + 0.8A^{1/3}$$

VI-13

b is the skin width and is related to the "10-90" fall-off distance by:

$$b = [\pi/2(3)^{1/2}\ln 9]t_{10-90} \text{ fm}$$

VI-14

For most cases, b is very close to unity and is set to be 1 fm in the present calculation. e(s) is dependent on the surface energy coefficient γ and the degree of diffuseness of the surface. The semi-empirical formula for the surface energy coefficient γ is given by:

$$\gamma = 0.9517[1 - 1.7826I^2] \text{ MeV/fm}$$

VI-15

where I=(N-Z)/A ; N, Z and A are the neutron, proton and mass numbers for the combined system of the two interacting nuclei.

One may get some insight into the proximity potential from

the properties of e(s). For large value of s, e(s) goes rapidly to zero. When the two bodies are in contact, s=0, the surfaces disappear and the gain in energy is about twice the surface energy $e(0)=-2\gamma$. For negative s, e(s) increases and become positive. The latter reflects the fact that compression takes place when rigid bodies overlap. One may view the repulsive part of the proximity potential at small distance as arising from the Pauli exclusive principle.

From Equation VI-11, the interactive potential U(s) is given by :

$$U_{ik}(s) = 2\pi[C_iC_k/(C_i+C_k)]\int_s^\infty e(s')ds' \qquad \text{VI-16}$$

The proximity potential can be expressed in terms of a dimensionless quantity $\eta=s/b$ and a dimensionless proximity function $\Psi(\eta)$

$$U_{ik}(\eta) = 4\pi\gamma[C_iC_k/(C_i+C_k)]b\Psi(\eta) \qquad \text{VI-17}$$

$$\Psi(\eta) = \int\phi(\eta')d\eta' \qquad \text{VI-18}$$

The value of Ψ as a function of η for $-3.5 \leq \eta \leq 3.5$ has been tabulated by Blocki et al. (Bl 77)

The proximity potential was originally derived to describe nuclei with thin skin width (leptodermous), large mass and large radius of curvature. These assumptions are not valid for light ions such as p, d, t, and α. In order to use the proximity

potential to describe light ion system, the central radius has been adjusted to fit the experimental data (Ta 78). For alpha particles, the central radius, C_{α} is found to be 1.35 fm.

Both linear and angular momentum are conserved in the calculation independent of integration step size. However, total energy conservation is strongly dependent on the integration step size. Energy conservation is very important in this type of calculation since energy non-conservation often leads to dissociation of the alpha particles from the original bound C-α cluster of the ^{16}O or any Al-α bound system produced during the calculation. Thus optimizing the integration step size is a necessity in this type of calculation. If Δt is too large, the numerical calculation of the trajectory is not accurate. Furthermore, energy is not conserved and bound states can dissociate. If Δt is too small, the amount of computer time needed to complete one trajectory calculation will be too long.

The following feature is incorporated into the program in order to speed up the computation. Before the computation for the motion of three particles starts, a potential table is created as a function of distance r for each pair of nuclei in the region where the nuclear potential is important. This table is constructed in such a way that the step size Δr is small when the nuclear force changes rapidly. In the case of the Woods-Saxon potential, no computation of exponentials are needed in the calculation during the trajectory calculation.

At any distance r_{ik} within the range of table, the force

term F_{ik} can be computed by the following equation:

$$F_{ik}(r) = -[U_{ik}(n+1) - U_{ik}(n)]/[r_{ik}(n+1) - r_{ik}(n)] \qquad \text{VI-19}$$

where i and k denote particles i and k, n is the index of the table and $r_{ik}(n+1) \leq r_{ik} \leq r_{ik}(n)$

Computing the force term with the procedure described above is analogous to representing the force function with a step-like function. If Δt can be so chosen such that the trajectory is always computed from $r_{ik}(n)$ to $r_{ik}(n+1)$ then energy would be conserved rigorously. However, this requirement cannot be satisfied. When three particles are involved, the exact value of Δt_{ik} for any two particles i and k such that the trajectory is computed from $r_{ik}(n)$ to $r_{ik}(n+1)$ in a three body problem cannot be computed easily. Instead the program estimates Δt_{ik} by the following formula

$$\Delta r_{ik} = U_{ik}\Delta t_{ik} + F_{ik}\Delta t_{ik}^2/m_{ik} \qquad \text{VI-20}$$

At any instant, three different Δt_{ik} are derived. Since each of the Δt_{ik} is computed approximately, there is no guarantee that the trajectory is computed within one step, $r_{ik}(n)$ to $r_{ik}(n+1)$. Whenever a step is skipped, slight energy non-conservation is introduced. In order to minimize energy non-conservation and at the same time keep the integration step at a reasonable size, Δt is always chosen to be the minimum of the three Δ_{ik}'s and that no more than one step is skipped at any given

time i.e. $r_{ik}(n-1) < r_{ik}' < r_{ik}(n)$ or $r_{ik}(n+1) < r_{ik}' < r_{ik}(n+2)$ where r_{ik}' is the new position computed from the Δt obtained. For the region where the nuclear force is important, Δt is of the order of 10^{-24} to 10^{-26} sec.

When the force considered is outside the range of the table, only the Coulomb force contributes. In this region, a different criterion is used to determine Δt used in the calculation. Since the Coulomb force F_c is inversely proportional to r^2, Δt can be chosen to be proportional to r, the relative distance between the two interacting nuclei. Thus, once the nuclei are far apart so that nuclear potential is no longer important, the calculation for the asymptotic trajectories is accomplished very rapidly.

C. Simulation using Monte Carlo Method

To completely specify the initial conditions of the ^{16}O nucleus in any trajectory, it is necessary to know both the impact parameter b for the ^{16}O and ^{27}Al system and the internal coordinates of C-α bound states. These internal coordinates can be described by the sign of relative velocity and by three spatial parameters; $r_{c-\alpha}$, the relative distance between carbon and alpha particles, the angular orientation of the C-α with respect to the lab, specified by the polar angle and the axial angle.

The Monte Carlo method is used to generate an ensemble of N trajectories. This ensemble samples all allowed initial conditions with corresponding probabilities. Initial values are

assigned to each of the input parameters using the random number generator such that the probability distribution for each of these parameters with a large sample size (N) is the same as expected within statistical errors. The probability density function for each of the parameters will be discussed below.

1. The impact parameter b :

One way of describing the initial condition of the ^{16}O and ^{27}Al system is to specify the impact parameter b. b is defined to be the perpendicular distance from the target to the beam direction as shown in the Fig. VI-1.

Classically, if there is a process such that all impact parameters less than or equal to a maximum impact parameter b_{max} contribute to that process, then the cross-section for that process is related to the maximum impact parameter b_{max} by

$$\sigma = \pi b_{max}^2 \qquad \text{VI-21}$$

The probability of finding a trajectory at a distance between b and b+db, f(b)db, is proportional to the area of the annulus, $2\pi bdb$. Thus the probability density function f(b) increases linearly with b. Since 2π is a constant, it is incorporated into the normalization constant N_b

$$f(b) = N_b * b \qquad \text{VI-22}$$

The significance of the normalization constant N_b will be discussed in Appendix D.

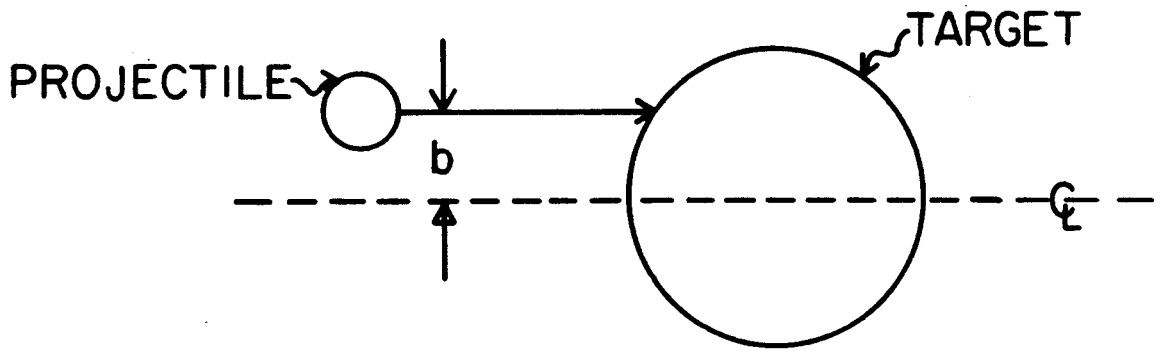

Fig VI-1 Definition of impact parameter b

f(b) increases linearly with b, $b_{fu} \leq b < b_{max}$. b_{fu} and b_{max} are the lower and upper limits of the impact parameters used in the Monte Carlo calculation. The values of b_{fu} and b_{max} can be estimated in the following way.

Fig. VI-2 shows a highly pictorial diagram of three main types of nuclear reactions. For very small impact parameters, the head on collision leads to fusion. For large impact parameters, the nuclear force is not important. The projectile only experiences the Coulomb force and suffers elastic scattering without loss of energy. In the intermediate range of impact parameters, the projectile approaches within the range of the nuclear force between the target and projectile. This may cause inelastic excitation of one or both of the nuclei. Mass and energy transfer may occur. This type of collision is known as a grazing collision. Pre-equilibrium alpha emissions are expected to occur in this last region. The contribution to the cross-sections by the various types of reactions as a function of impact parameter b is shown in Fig. VI-3. With a sharp cut-off model and the unitarity of cross-section, both b_{max} and b_{fu} can be obtained from Equation VI-21.

Using the optical model parameters which fit the $^{27}Al + ^{16}O$ elastic scattering data as described in Chapter IV-F, the total reaction cross-section is found to be 1426 mb giving b_{max}=6.7 fm. To obtain b_{fu}, the experimental value for the fusion cross-section is used (Ba 77) σ_{fu} =1185 mb thus b_{fu}=6.1 fm. The values of b that lead to non-fusion, non-elastic reactions occur in a very

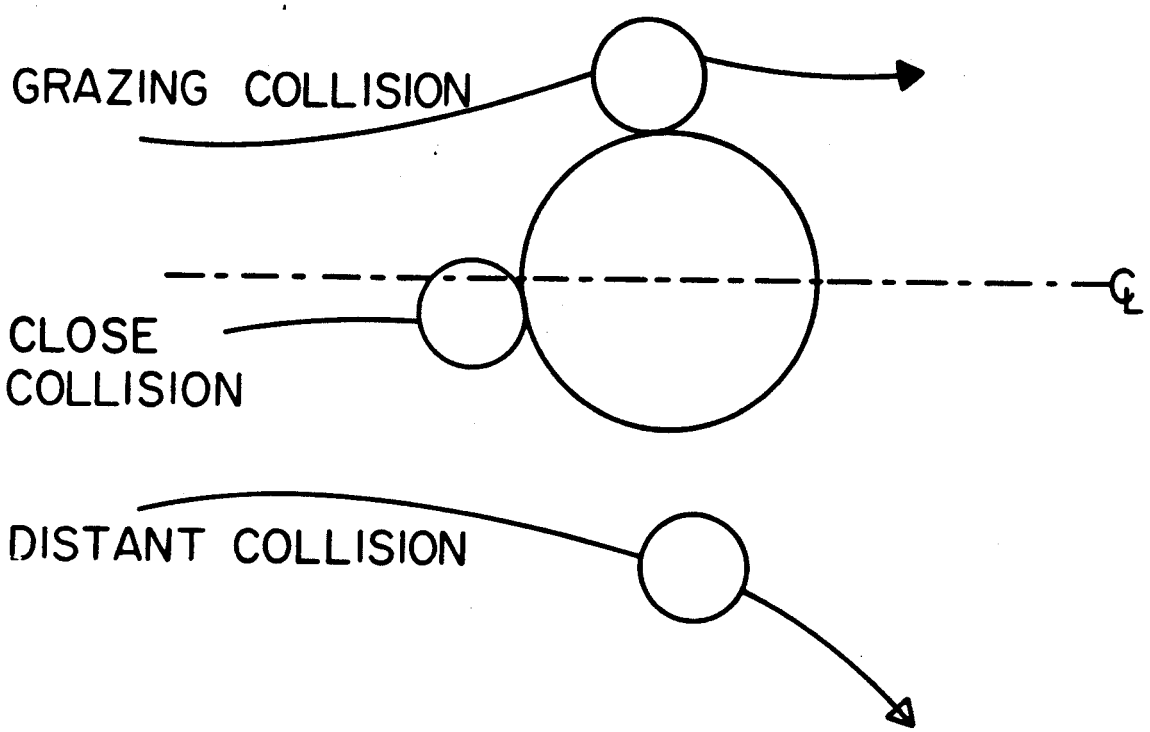

Fig VI-2 Schematic diagram of three main types of reaction a.) close collision, b.) grazing collision and c.) distant collision

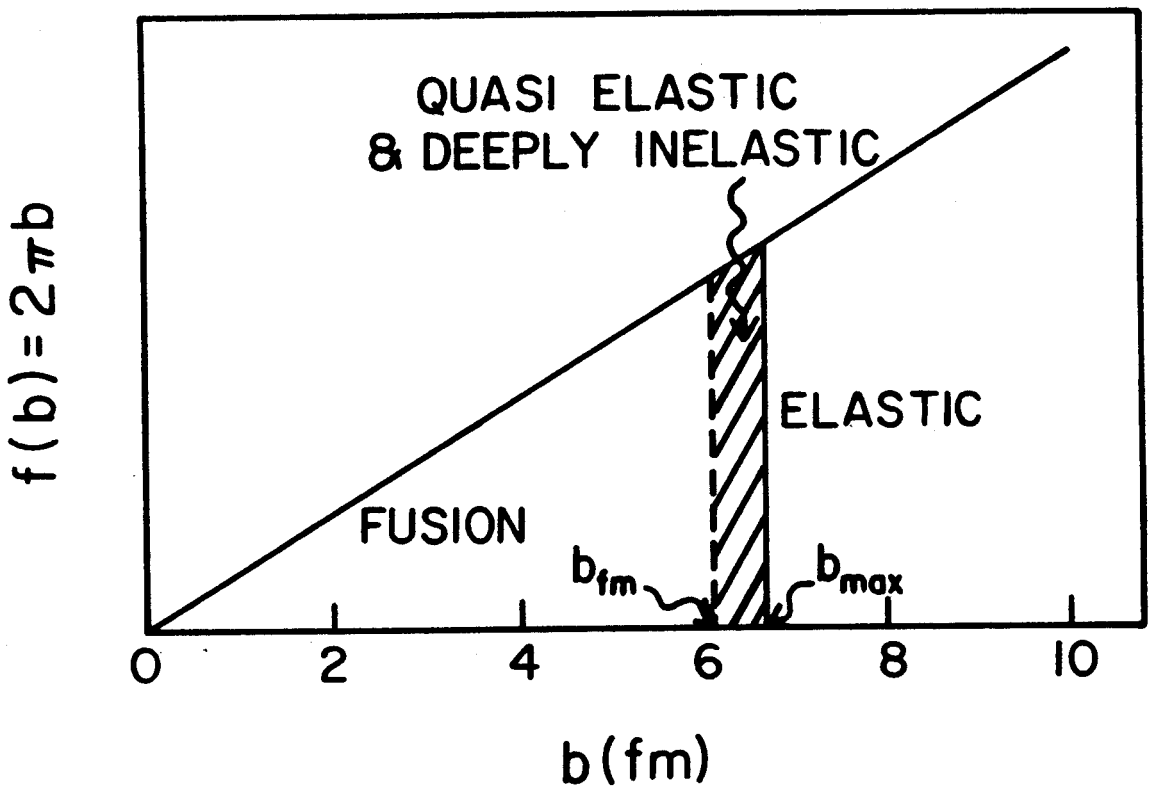

Fig VI-3 Schematic diagram showing three main types of reaction, fusion, quasi-elastic and deeply inelastic and elastic reaction, plotted as a function of impact parameter b.

small range , 6.1 fm < b < 6.7 fm. Since the sharp cut-off model was used and no knowledge of the exact shape of the distribution of partial waves contributing to a given process are known the values obtained above only provide a rough guideline. As a matter of fact, when the calculation is scanned through 4 fm < b < 7 fm most of the events of interest generally occur between 5.0 and 6.5 fm. Thus in the present calculation, the value of b is chosen to be $4.5 \leq b < 7.0$ fm.

2. The relative distance between carbon and alpha particles in the center of mass system of ^{16}O :

The probability of finding the C-α system at $r_{c-\alpha}$, $f(r_{c-\alpha})$, is proportional to the time that the C-α particles spend at that relative distance, $r_{c-\alpha}$. Thus $f(r_{c-\alpha})$ is inversely proportional to the C-α velocity at $r_{c-\alpha}$.

$$f(r_{c-\alpha}) = N_r/v(r_{c-\alpha}) \qquad \text{VI-23}$$

$$v_{c-\alpha}(r_{c-\alpha}) = 2[E - U(r_{c-\alpha})]/\mu \qquad \text{VI-24}$$

where N_r is normalization constant and $r1 < r_{c-\alpha} < r2$. where ri are the turning points for the C-α system when the kinetic energy is zero and the total potential energy of C-α equals to the binding energy, E_b. For the Woods-Saxon potential, there is only one turning point and r1=0.

At any given $r_{c-\alpha}$, the C-α particles can be travelling either towards or away from each other i.e. $v_{c-\alpha}$ can be positive

or negative. To take care of this, the sign of $v_{c-\alpha}$ is varied from trajectory to trajectory.

The previously mentioned assumption that the ^{16}O is represented by a bound state consisting of a ^{12}C and an alpha particle leads to the requirement that the alpha and ^{12}C are in a relative S state. Then the only remaining unspecified parameters describe the orientation of $r_{c-\alpha}$ with respect to the laboratory frame.

3. Relative C-α angle in the ^{16}O center of mass system :

The relative spatial orientation of C-α in the ^{16}O center of mass system is completely specified by the relative distance $r_{c-\alpha}$, the polar and axial angles, $\theta_{c-\alpha}$ and $\phi_{c-\alpha}$. The probability distribution functions for these angles are

$$f(\theta_{c-\alpha}) = \sin(\theta_{c-\alpha}) \qquad 0 < \theta_{c-\alpha} < \pi \qquad \text{VI-25}$$

$$f(\phi_{c-\alpha}) = 1/2\pi \qquad 0 < \phi_{c-\alpha} < 2\pi \qquad \text{VI-26}$$

The calculation using Woods-Saxon potentials was carried out by sampling through all possible $r_{c-\alpha}$, $\theta_{c-\alpha}$ and $\phi_{c-\alpha}$ in describing the ^{16}O as the composite nucleus of ^{12}C and α. These two variables were reduced to one in the calculation using the proximity potentials.

As described in Chapter V-B-3, the pre-equilibrium alpha emission data from the present work is extracted in the reaction plane defined by the beam and the carbon detector. In order to

compare with the available experimental data, only trajectories that lead to scattering of both carbon and alpha particles in the reaction plane are of interest. In the calculation, the reaction plane is defined to be the plane that contains all three particles ^{12}C, α and ^{27}Al and the beam direction. Both the ^{12}C and alpha particles must lie in the plane defined by the ^{16}O and ^{27}Al if they are to be scattered into this plane due to conservation of momentum. With this restriction on the trajectories, only one angle, $\phi_{c-\alpha}$, is needed to describe the relative C-α orientation in the reaction plane. The probability density function of $\phi_{c-\alpha}$ is constant as given by Equation VI-26 i.e. the alpha particle can lie in any angle with respect to the carbon particle, there is no preferred direction.

Random numbers are obtained from the DEC Subroutine RAN which generates uniformly distributed random numbers in the interval [0,1], $0 < r < 1$. In order to generate the correct ensemble of trajectories, the random numbers generated by RAN are manipulated to create initial trajectory parameters which follow the probability density functions discussed above. The formalism used to create these parameters is derived in Appendix D.

A modern computer VAX/VMS was used in this calculation. Even with this high speed digital computer and modification in computing the force term, it takes one and a half minutes of computer CPU time to process one trajectory. It therefore takes about one day of CPU time to perform 1000 trajectories!

Table VI-1 Three Woods-Saxon Potential Parameter Sets used in the 3-Body Trajectory Calculation

	C-α			Al-C			Al-α		
	U(MeV)	a(fm)	R(fm)	U(MeV)	a(fm)	R(fm)	U(MeV)	a(fm)	R(fm)
I	24.9	0.65	4.85*	35	0.55	6.08**	80	0.31	7.5@
II	24.9	0.65	4.85	35	0.55	6.08	34	0.31	7.5@
III	24.9	0.65	4.85	35	0.55	6.08	218	0.68	4.72@@

* See text

** Da 75

@ Ba 67

@@ Ke 72

D. Results of Calculations

1. Woods-Saxon Potential :

Three different sets of Woods-Saxon parameters listed in Table VI-1 were used in the calculation. The results from parameter set I will be discussed first. In this calculation, both in-plane and out-of-plane C-α angles were varied to get all possible C-α orientations in ^{16}O. 198 out of 5000 trajectories processed yielded three final particles, ^{27}Al, ^{12}C and α at the end of the three-body calculation. The remainder of the trajectories are events that yield Al-C, C-α or Al-α bound states as final products. Of these 198 trajectories, 41 trajectories have the asymptotic outgoing angle of the ^{12}C particle between 25^{o} to 35^{o}. Fig. VI-4 shows the in-plane alpha angular correlation in the laboratory system of the events with the ^{12}C angle between 25^{o} to 35^{o}. This figure can be compared to the pre-equilibrium angular correlation plotted in the lab frame obtained experimentally as shown in Fig. V-23. The angle convention used in Fig. VI.4 is the same as that used previously with angles on the same side of the beam as the ^{12}C detector defined to be negative. The angular correlation is broken up into bins of 10 degree width. Each event in the histogram is indicated by a + sign for positive angle (non-orbiting) scattering and a - sign for negative angle (orbiting) scattering of the carbon particle. About twice as many events are scattered to the opposite side of the beam axis from the carbon detector. Most of the trajectories with the alpha particles scattered to the same side of the beam as

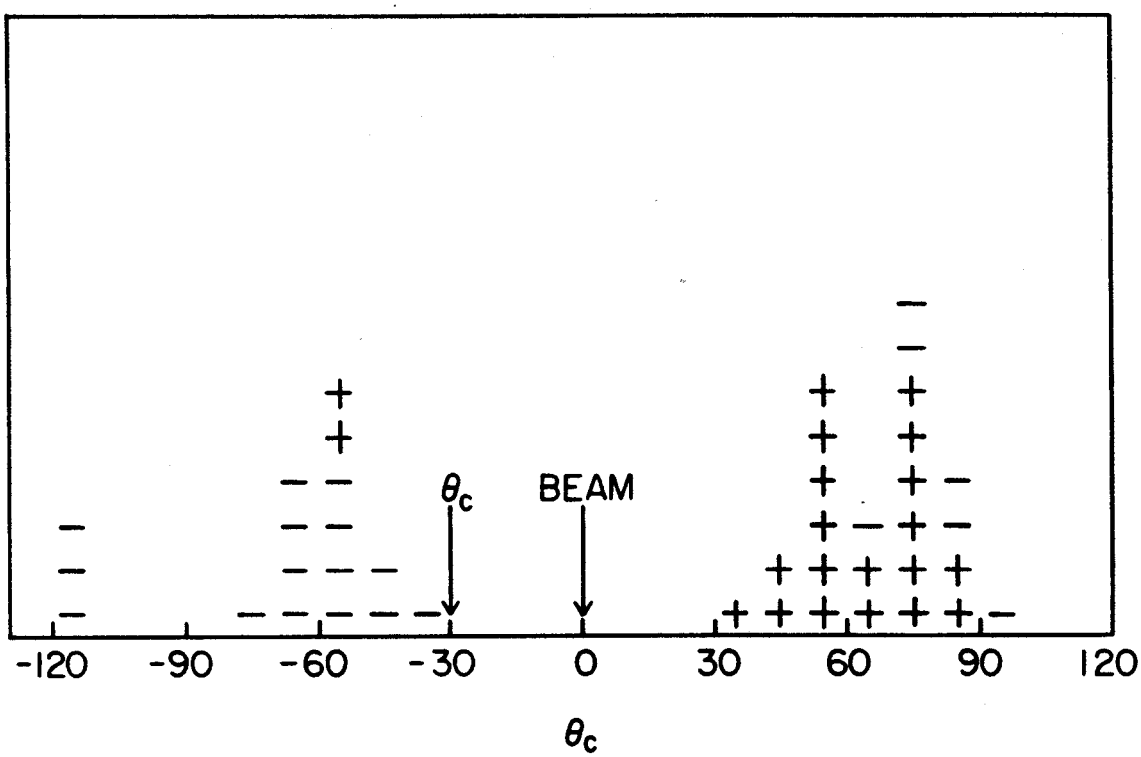

Fig. VI-4 C–α angular distribution at θ_c=-30° using the Woods-Saxon potential parameter set I as listed in Table VI-1

the carbon particles correspond to events where the C particles orbit around the ^{27}Al nucleus. The angular correlation peaks around 70^{o} on either side of the beam. It is interesting to see that a "shadow region" similar to the one obtained in the "hot spot" model calculation is obtained along the beam axis.

The average energies of the alpha particles of interests is about 11 MeV, much less than the energy of the pre-equilibrium alpha particles observed experimentally.

In order to gain insight into the results of the trajectory calculation, a program called 3BODYPLT was written to plot out the projections onto the reaction plane of the positions of the three particles as a function of time. Fig. VI-5 is an example of such a plot. In this plot, the positions of the three particles are plotted once about every 200 integration steps. ▷ , ⊕ and ⌒ are the symbols for ^{27}Al, α and ^{12}C respectively. The ^{16}O beam moves from left to right in the plot. The XY plane is the reaction plane containing the beam axis and the carbon detector. The time interval on the figure is the elapsed time between the first and last plotted positions. For this particular trajectory, the C-α bound system oscillates until the alpha particle feels the nuclear potential of the Al nucleus. The circle is centered approximately at the initial position of the Al nucleus. The radius of the circle equals $R_{Al-\alpha}$. When the alpha particle reaches the edge of the Al-α nuclear potential, its direction changes and it is scattered to a more backward angle. The alpha particle then moves in the combined potential fields of Al-α and

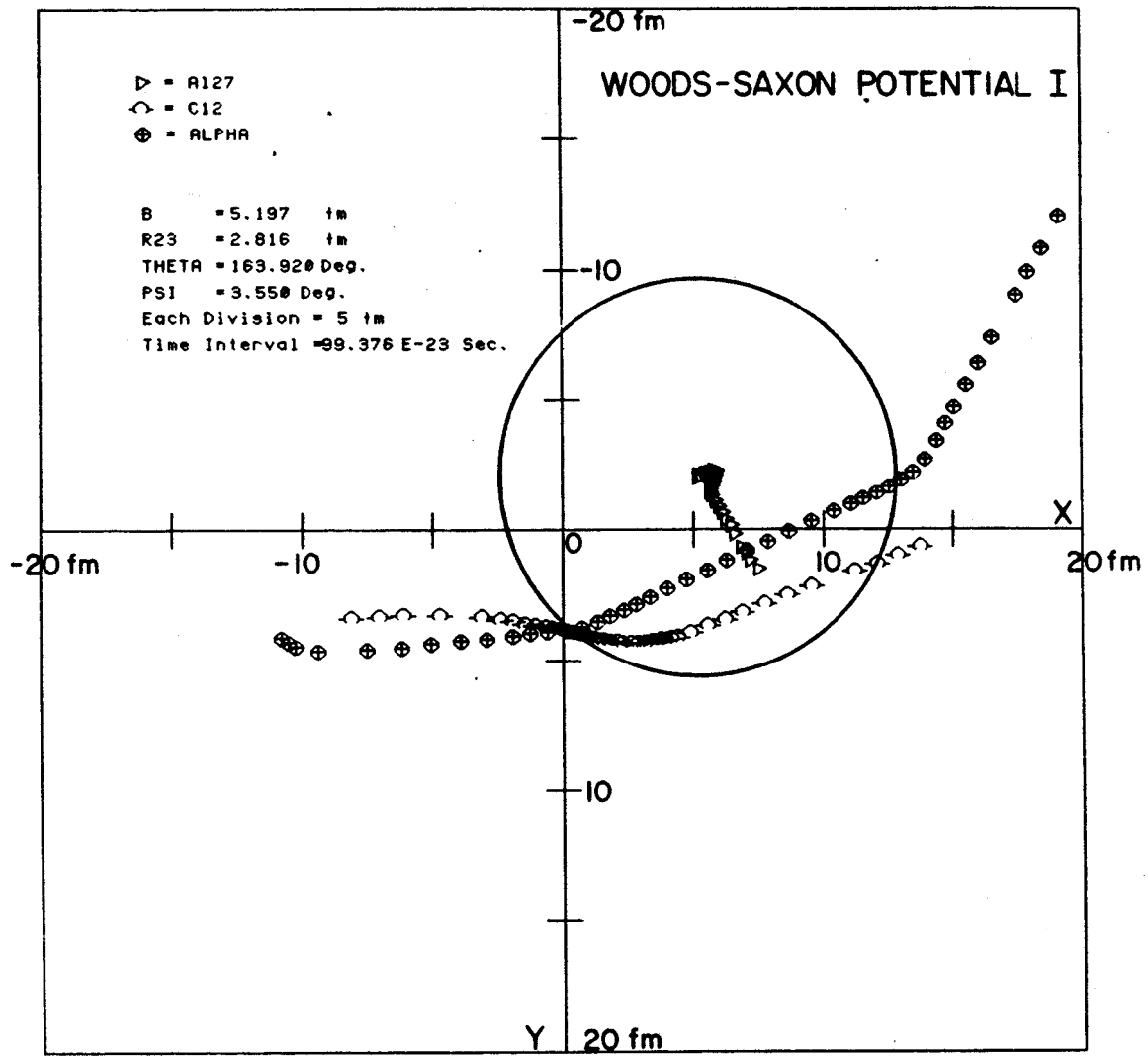

Fig. VI-5 The trajectories of the three particles ^{27}Al, α, and ^{12}C projected onto the reaction plane as a function of time. Parameter set I listed in Table VI-1 was used.

C-α along a fairly straight line. The alpha particle suffers another more abrupt backward angle scattering when it leaves the nuclear field of Al-α. At this point, the carbon and alpha particles are so far apart that the carbon particle exerts little influence on the alpha trajectory. This is analogous to an object that moves in a medium and suffers deflection when it crosses from one medium to another one with a different index of refraction. The trajectory shown is a typical one using parameter set I.

From the above observation, it becomes clear that the Al-α potential is very important in determining the final results of the three-body trajectory calculation. In order to study this, parameter set II which fits the same $^{27}Al + \alpha$ elastic scattering data but with a smaller $U_{Al-\alpha}$ was used. In 3000 trajectories, however, no three body final states were observed i.e. all trajectories ended up with two of the nuclei in a bound state. This can be understood since the Al-α potential of set II is not deep enough to break the alpha particle away from the carbon particle in the oxygen nucleus.

Another completely different Woods-Saxon potential (set III of Table VI-1) that fits high energy $\alpha + {}^{27}Al$ elastic scattering data was also used. As was the case for set II, no three-body final states were obtained after 3000 trajectories were processed. In this case, the $^{27}Al-\alpha$ potential is so deep that once the alpha particle is attracted by the ^{27}Al, the ^{27}Al and α form a bound entity. From these calculations with Woods-Saxon potentials, it is very clear that the results of these calculations are certainly

very sensitive to the Al-α potential. Since no single unambiguous Woods-Saxon potentials can be obtained from the experimental data on elastic scattering of alpha particles on ^{27}Al, a different form of nuclear potential, the proximity potential, with minimum adjustable parameters is used.

2. Proximity Potential:

In the case of the proximity potential, in order to optimize the calculation as explained in Section C-3 of this chapter, the initial positions and velocities of all three particles lie in the reaction plane. Of 3200 trajectories processed, only two trajectories yielded a three-body final state with the asymptotic carbon angle between 25^{o} to 35^{o}. One trajectory with an asymptotic alpha angle of 90^{o} is shown in Fig. VI-6. The other trajectory yields a more forward alpha scattering angle of 25^{o}. One common feature of trajectories calculated using the proximity potential is that the carbon and alpha particle cannot pass through each other due to the presence of the repulsive core. This repulsive core can be seen in Fig. VI-7 where the C-α proximity potential together with the three Al-α Woods-Saxon parameter sets listed in Table VI-1 are plotted. The shape of all these potentials are very different. The internal shape of the proximity potential is responsible in generating the more complicated trajectory as seen in Fig. VI-6.

E. Conclusion

None of the four different potentials used in the three-body trajectory calculation reproduce the experimental

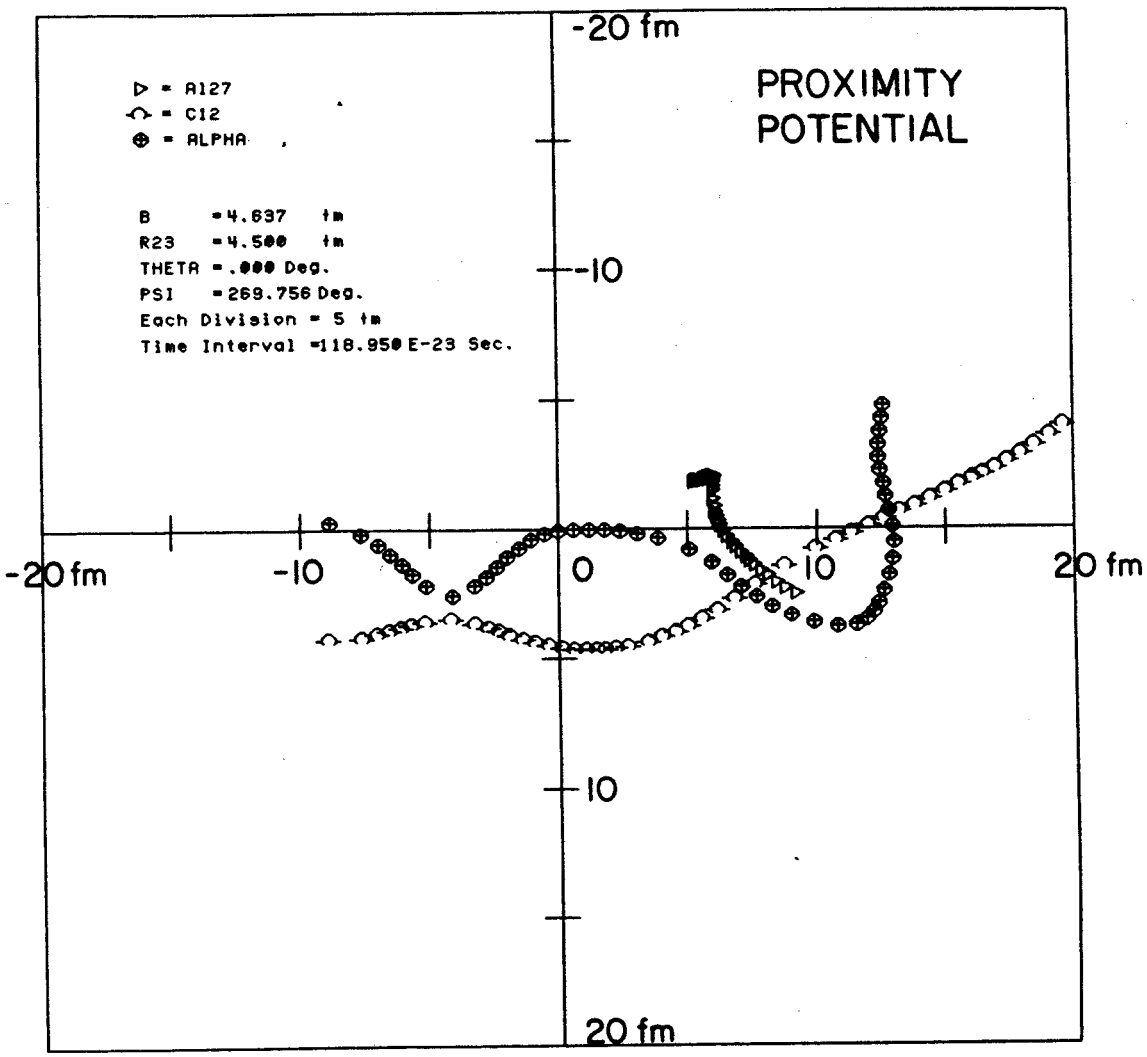

Fig. VI-6 The trajectories of the three particles ^{27}Al, α, and ^{12}C on the reaction plane. The proximity potentials were used.

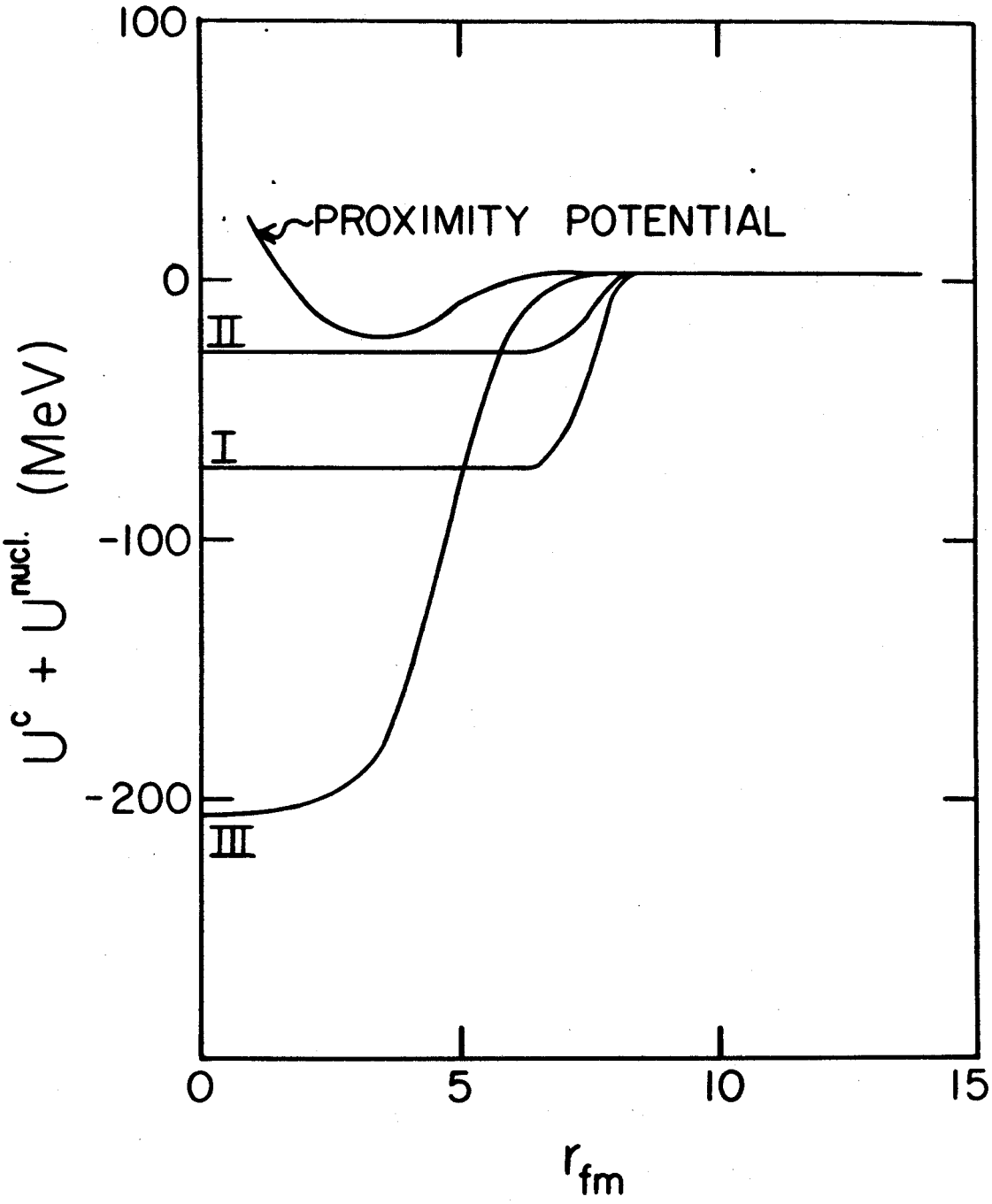

Fig. VI-7 Different ^{27}Al-α potentials plotted as a function of distance. I, II and III refer to the Woods-Saxon potentials listed in Table VI-1.

results. Furthermore, the results of the calculation are very sensitive to the detailed internal structure of the potentials. The slope of the Woods-Saxon Al-α potential causes deflection of the α particles to the more backward angles. It is not clear that other choices of Woods-Saxon potentials would cause the deflection to be in the forward direction. In light of this fact, it is not surprising that the calculation of Gamp et al. gives forward peaking since no nuclear potentials were included in that calculation. On the other hand, it is very interesting that the celebrated "shadow region" of the "hot spot" model is also reproduced without inclusion of absorption.

The particle trajectories from the proximity potentials are very complicated and cannot be understood in a simple way. In addition, too few trajectories break up into ^{12}C, α and ^{27}Al with the asymptotic ^{12}C scattered to the desired angle. This prohibits collection of a statistically significant sample to examine the angular distribution of the alpha particles.

The main disadvantage of the calculation described in this chapter is the amount of computer time needed to sample through a large number of trajectories. This greatly restricts the freedom of testing different potential parameters. None of the four potentials used reproduces the experimental angular correlation function as shown in Fig. V-23. This may be attributed to the wrong choice of potentials. It can also be that the assumptions used in the calculation as described in Section A of this chapter may not be right. For example, the $^{12}C(2^+)$-α contribution to the

^{16}O configuration may be important or some form of energy dissipation mechanism may need to be incorporated into the calculation to account for core excitation.

CHAPTER VII

CONCLUDING REMARKS

A. Summary of Present work and comparison with other work

The results obtained from the present experiment and the earlier results obtained by Harris et al. (Ha 77a) differ significantly. The earlier result supported the hypothesis that pre-equilibrium sequential alpha decay from an intermediate nucleus $^{31}P^{*}(E_x=14.5$ MeV) was the dominant mode of alpha emission. The result from the present work, especially the experimental evidence from the out-of-plane angular correlation and in-plane back angle data, indicate that the C-α coincident events observed mainly come from equilibrium alpha evaporation from the intermediate nucleus $^{31}P^{*}(E_x=14.5$ MeV). More recent results from other systems (Na 80, Bh 78) also indicate that contributions due to alpha evaporation, either from the projectile-like or target-like particles, are very important and in most cases account for nearly all of the heavy-ion, alpha coincidence events observed. The presence of these equilibrium components renders difficult the extraction of the small pre-equilibrium component observed.

Another interesting result from this work is the strong dependence of pre-equilibrium alpha emission as a function of the carbon detector angle. At $\theta_c=-40^{o}$, the C-α angular correlation function is consistent with that of evaporation from $^{31}P^{*}$. At

θ_c=-30°, the pre-equilibrium alpha emission constitutes about 10% of the total C-α yield. Owing to the high counting rate coming from elastic scattered ^{16}O particles, it is very difficult to obtain an angular correlation data at θ_c more forward than 30° in the present system even though such information would be desirable for comparison with results obtained up to date. Thus the result obtained in coincidence experiments is very sensitive to the choice of the heavy ion detector angle. This fact was probably not recognized when particle-particle coincidence experiments were first employed as a tool to study heavy ion reaction mechanisms.

The current approach of particle-particle coincidence experiments on various different systems to look for systematics in the experimental data is probably not the best way to understand the nature of pre-equilibrium alpha emission. Instead, a very careful and in-depth study should be conducted on a few selected systems. These systems should be completely understood before broad scale investigations with many different projectiles and targets should be carried out. For example, in order to compare pre-equilibrium alpha emission with the "piston model", the angular correlations of three-body events as a function of the two-body Q values of the reaction are needed. This requires a system with higher bombarding energy where the deeply inelastic cross-section is more substantial than in the present work and also data with good statistics. Another example where more data would be valuable is the $^{58}Ni + ^{16}O$ system. ^{16}O-α coincidence data are needed at very forward angles close to the beam axis to

identify the shadow region predicted by the original "hot spot" calculation.

B. Future Experiments

Based on knowledge obtained from the present work, numerous experiments can be designed to gain further understanding of the nature of pre-equilibrium alpha emission. However, most of the experiments will involve detecting the carbon or alpha particles at forward angles. Unfortunately, elastic scattering cross-section increases as the inverse fourth power of the angle (θ^4) at small angles. Elastic scattered projectile particles have to be removed before coincidence data with small cross-section can be taken at these angles. The following techniques are usually employed to achieve this goal.

1. Mass Spectrometer :

Spectrometers are often used to select out particles of the desired mass to charge ratio e.g. α particles with charge state 2^+, from the other reaction products such as elastically scattered projectile particles. If a spectrometer with a large solid angle is available, this technique is very reliable and does not suffer from the low alpha energy cutoff problem.

2. Stopping Foil:

A thick Au or Pt foil can be mounted in front of the alpha detector at forward angles to range out the elastically scattered beam particles. The thickness of the foil is so chosen that the desired particle will be able to pass through the foil into the detector behind it. This technique has been used by Gamp

et. al. (Ga 78) in the Si-α coincidence measurement using $^{197}Au + ^{32}S$ reaction. One disadvantage of this method comes from the low energy cutoff due to low energy alpha or carbon particles ranging out in the foil. Assumptions on the low energy portion of the alpha or carbon particle spectrum have to be made in the data analysis to obtain total coincidence yield.

If a reliable technique can be developed to obtain data at forward angles, three main types of experiments should be studied systematically.

1. Data with alpha detector at angles less than 15^{o} on either side of the beam are certainly desirable as a direct extension of the present work. Based on the forward angle data now available from the present work, one may be able to obtain these forward angle data using a Au cover foil. In this case, one can assume that all the low energy (less than 10 MeV) alpha particles that will range out in the cover foil arise from the equilibrium component. One can then investigate the presence or absence of a "shadow region" and give the exact shape of the pre-equilibrium C-α angular correlation function in this interesting forward angle region.

2. An Out-of-plane C-α angular correlation function at forward angles where the pre-equilibrium component is large is necessary to better determine the nature of the pre-equilibrium alpha contribution.

3. A C-α angular correlation should be determined with the carbon detector fixed at an angle more forward than 30^{o}

studied in the present work. Results from the present work indicates that the cross section for the pre-equilibrium alpha particles may be much bigger when the carbon detector is at more forward angles.

All these experiments will lead to further understanding of the pre-equilibrium alpha emissions. Thus the present work is not completed in the sense that the knowledge one gains from this work provides a glimpse of the horizon beyond.

REFERENCES

Aj 77 F. Ajzenberg-Selove, Nucl. Phys. A281, 20 (1977)

Ba 77 B.B. Back, R.R. Betts, C. Gaarde, J.S. Larsen, E. Michelsen and T. Kuang-Hsi, Nucl. Phys. A285, 317 (1977)

Bh 78 R.K. Bhowmik, E.C. Pallocco, N.E. Sanderson, J.B.A. England and G.C. Morrison, Phys. Lett. 80B, 41 (1978)

Bh 79 R.K. Bhowmik, E.C. Pollaco, N.E. Sanderson, J.B.A. England, and G.C. Morrison, Phys. Rev. Lett. 43, 619 (1979)

Bi 79 R. Billerey, C. Cerutti, A. Chevarier, N. Chevarier, B. Cheynis, and A. Demeyer, Z. Phys. A292, 293 (1979)

Bl 77 J. Blocki, J. Randrup, W.J. Swiatecki, and C.F. Tsang, Ann. Phys. 105, 427 (1977)

Br 61 H.C. Britt and A.R. Quinton, Phys. Rev. 124, 877 (1961)

Br 67 F.P. Brady, J.A. Jungerman and J.C. Young, Nucl. Phys. A98 241 (1967)

Ca 66 L.R. Canfield, G. Hass and J.E. Waylonis, Applied Optics 5 45 (1966)

Da 75 J. Dauk, K.P. Lieb, and A.M. Kleinfeld, Nucl. Phys. A241, 170 (1975)

De 73a R.M. deVries, Nucl. Phys. A212, 207 (1973)

De 73b R. deVries, Phys. Rev. Lett. 30, 666 (1973)

Ds 75 R. Da Silveira and Ch. Leclerq-Willain, Le Journal de Physique, Lettres 36, L-117 (1975)

Dy 79 P. Dyer, R.J. Puigh, R. Vandenbosch, T.D. Thomas, M.S. Zisman, and L. Nunnelley, Nucl. Phys. A322, 205 (1979)

Ei 73 H. Eichner, H. Stehle and P. Heiss, Nucl. Phys. A205, 249 (1973)

En 74 J.B.A. England in Techniques in Nuclear Structure Physics, Part I, John Wiley & Sons, Inc., pp. 419-503

Er 58 59 T.E.O. Ericson and V.M. Strutinski, Nucl. Phys. 8, 284 (1958) 9, 689 (1959)

Fr 79 J. Freeman and A.J. Lazzarini, Nuclear Physics Laboratory Annual Report, University of Washington (1979) p. 164

GA 78 A. Gamp, J.C. Jacmart, N. Poffé, H. Doubre, J.C. Roynette, and J. Wilczynski, Phys. Lett. 74B, 215 (1978)

Ge 77 G.K. Gelbke, M. Bini, C. Olmer, D.L. Hendrie, J.L. Laville, M. Mahoney, M.C. Mermaz, D.K. Scott and H.H. Wieman, Phys. Lett. 71B, 83 (1977)

Go 75 F.S. Goulding and B.G. Harvey, Ann. Rev. Nucl. Sci. 25, 167 (1975)

Go 78 P.A. Gottschalk and M. Weström, Nucl. Phys. A314, 232 (1979)

Gr 61 C. Gruhn, Thesis, University of Washington, Seattle, 1961

Gr 77 D.H.E. Gross and J. Wilczynski, Phys. Lett. 67B, 1 (1977)

Ha 60 I. Halpern, Bull. Amer. Phys. Soc. II, 5, 510 (1960) and private communication

Ha 77a J.W. Harris, T.M. Cormier, D.F. Geesaman, L.L. Lee, Jr, R.L. McGrath, and J.P. Wurm, Phys. Rev. Lett. 28, 1460 (1977)

Ha 77b J.W. Harris, P. Braun-Münzinger, T.M. Cormier, D.F. Geesaman, L.L. Lee, Jr., R.L. McGrath and J.P. Wurm, Proc. Internat. Conf. Nucl. Structure, Tokyo, (1977) p. 698

Ha 78 J.W. Harris, Thesis, S.U.N.Y. at Stony Brook, 1978

Ho 77 H. Ho, R. Albrecht, D. Dunnweber, G. Graw, S.G. Steadman, J.P. Wurm, D. Disdier, V. Rauch and F. Scheibling, Z. Phys. A283, 237 (1977)

Ke 72 K.W. Kemper, A.W. Obst and R.L. White, Phys. Rev. C6, 2090 (1972)

Ma 63 R.P. Madden, L.R. Canfield, and G. Hass, J. Opt. Soc. Am. 53, 620 (1963)

Ma 69 F.W. Martin, Phys. Rev. Lett. 22, 329 (1969)

Na 80 M.N. Namboodiri and J.B. Natowitz, private communication on the system $^{20}Ne + ^{27}Al$ at 120 MeV

Pe 76 C.M. Perey and F.G. Perey, Atomic Data and Nuclear Data Tables 17, 1 (1976)

Re 56 C.W. Reich, G.C. Phillips and J.R. Russell, Jr., Phys. Rev. 104, 143 (1956)

Ro 67 R.R. Roy and B.P. Nigam in Nuclear Physics, John Wiley & Sons, Inc., p. 206

Ro 75 76 G. Roth and J. Wiborg, Nuclear Physics Laboratory Annual Report, University of Washington (1975), p. 22; (1976) p. 26.

Sa 77 J. Sanislo, J. Bussoletti, and P. Dickey, Nuclear Physics Laboratory Annual Report, University of Washington (1977) p. 177

Sa 79 M. Sasagase, M. Sato, S. Hanashima, K. Furuno, Y. Tagishi, Y. Nagashima, S.M. Lee and T. Mikumo, Proceedings of International Symposium on Continuum Spectra of Heavy Ion Reactions, San Antonio, Texas (1979) p. 33

Sc 77 W.U. Schröder and J.R. Huizenga, Ann. Rev. Nucl. Sci. 27, 465 (1977)

Sh 51 F.C. Shoemaker, J.E. Faulkner, G.M.B. Bouricius, S.G. Kaufmann, and F.P. Mooring, Phys. Rev. 83, 1011 (1951)

Sh 78 T. Shimoda, M. Ishihara, H. Kamitsubo, T. Motobayashi, and T. Fukuka, Proc. IPCR Symp. on Macroscopic Featurs of Heavy Ion Collisions and Pre-equilibrium Process, Hakone (1977) p. 93

Ta 78 S.L. Tabor, D.A. Goldberg and J.R. Huizenga, Phys. Rev. Lett. 41, 1285 (1978)

Tr 77 W. Trautmann, J. de Boer, W. Dunnweber, G. Graw, R. Kopp, C. Lauterbach, H. Puchta, and U. Lynen, Phys. Rev. Lett. 39, 1062 (1977)

We 74 W.G. Weitkamp and F.H. Schmidt, in Large Electrostatic Accelerators, ed. by D.A. Bromley, North Holland Publishing Co., 1974, p. 65

We 77 M.L. Webb, Thesis, University of Washington, Seattle, 1977

Wil 73 J. Wilczynski, Phys. Lett. 47B, 484 (1973)

Wit 73 A.B. Wittkower and H.D. Betz, Atomic Data 5, 113 (1973)

Appendix A

KINEMATICS OF THREE-BODY FINAL STATES

The three-body reaction can be represented as

$$^{27}Al + ^{16}O \rightarrow ^{12}C + \alpha + ^{27}Al \qquad A.1$$

By conservation of energy

$$E_o = E_c + E_\alpha + E_{Al} + Q \qquad A.2$$

where E_i is the energy of particle i in the lab system.

By conservation of linear momentum

$$\vec{P}_o = \vec{P}_c + \vec{P}_\alpha + \vec{P}_{Al} \qquad A.3$$

where $\vec{P}_i$ is the momentum vector of particle i.

The coordinate system used is shown in Fig. A.1. The beam direction is defined to be along the Z axis, i.e., $\theta = 0°$.

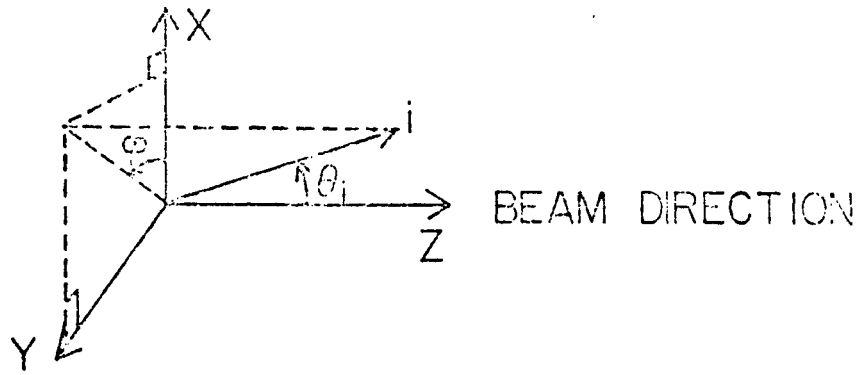

Fig. A.1. Coordinate system used in three-body kinematics

Decomposing the momentum into the X, Y, Z components A.3 becomes:

$$|P_o| = |P_c|\cos\theta_c + |P_\alpha|\cos\theta_\alpha + |P_{Al}|\cos\theta_{Al} \qquad A.4$$

$$0 = |\vec{P}_c| \sin\theta_c \cos\phi_c + |P_\alpha| \sin\theta_\alpha \cos\phi_\alpha + |P_{Al}| \sin\theta_{Al} \cos\phi_{Al} \qquad A.5$$

$$0 = |\vec{P}_c| \sin\theta_c \sin\phi_c + |P_\alpha| \sin\theta_c \sin\phi_\alpha + |P_{Al}| \sin\theta_{Al} \sin\phi_{Al} \qquad A.6$$

Squaring and adding A.4, A.5, and A.6

$$\begin{aligned} |P_{Al}|^2 = {} & |P_o|^2 + |P_c|^2 + |P_\alpha|^2 - 2|P_o|\,|P_\alpha| \cos\theta_\alpha \\ & - 2|P_o|\,|P_c| \cos\theta_c + 2|P_c|\,|P_\alpha| \cos\theta_c \cos\theta_\alpha \\ & + 2|P_c|\,|P_\alpha| \sin\theta_c \sin\theta_\alpha \cos\left(\phi_c - \phi_\alpha\right) \end{aligned} \qquad A.7$$

Substituting the identity $|P|^2 = 2mE$ into A.7

$$\begin{aligned} m_{Al}E_{Al} = {} & m_oE_o + m_cE_c + m_\alpha E_\alpha - 2\sqrt{m_o m_\alpha E_o E_\alpha} \cos\theta_\alpha \\ & - 2\sqrt{m_o m_c E_o E_c} \cos\theta_c + 2\sqrt{m_c m_\alpha E_c E_\alpha} \cos\theta_c \cos\theta_\alpha \\ & + 2\sqrt{m_c m_\alpha E_c E_\alpha} \sin\theta_c \sin\theta_\alpha \cos\left(\phi_c - \phi_\alpha\right) \end{aligned}$$

From A.2 $Q = E_o - E_c - E_\alpha - E_{Ae}$

$$\begin{aligned} Q = {} & \left(1 - \frac{m_o}{m_{Al}}\right) E_o - \left(1 + \frac{m_c}{m_{Al}}\right) E_c - \left(1 + \frac{m_\alpha}{m_{Al}}\right) E_\alpha \\ & + \frac{2}{m_{Al}} \sqrt{m_o m_\alpha E_o E_\alpha} \cos\theta_\alpha + \frac{2}{m_{Al}} \sqrt{m_o m_c E_o E_c} \cos\theta_c \\ & - \frac{2}{m_{Al}} \sqrt{m_c m_\alpha E_c E_\alpha} \left(\cos\theta_c \cos\theta_\alpha + \sin\theta_c \sin\theta_\alpha \cos(\phi_c - \phi_\alpha)\right) \end{aligned} \qquad A.8$$

Equation A.8 relates the Q value of the reaction A.1 to E_o, E_c, E_α, θ_c, θ_α, ϕ_c, and ϕ_α.

Appendix B

THREE-BODY KINEMATICS OF SEQUENTIAL BREAK-UP PROCESS

The three-body reaction is assumed to go through the following sequential break-up process.

$$^{27}Al + ^{16}O \rightarrow ^{12}C + ^{31}P^* \qquad B.1$$

$$^{31}P^* \rightarrow \alpha + ^{27}Al \qquad B.2$$

The formula that transforms energy and angles from the laboratory system to the center-of-mass system of $^{31}P^*$ will be derived in this appendix. In addition, the Jacobian that transforms cross sections in the laboratory system to the $^{31}P^*$ center-of-mass system will also be derived.

For simplicity, only two-dimensional space is considered in the break-up of $^{31}P^*$. The following derivation can be generalized to three dimension. However by utilizing the symmetry of the Jacobian and angle transform as explained later, formulae derived in the two-dimensional space are sufficient to obtain the center-of-mass angle and Jacobian transformation for the out-of-plane set up.

Equation B.1 represents a standard two-body reaction as shown in Fig. B.1. The beam direction is defined to be 0° and θ_c is defined as negative.

By conservation of energy

$$E_o = E_c + E_p + Q_2 \qquad B.3$$

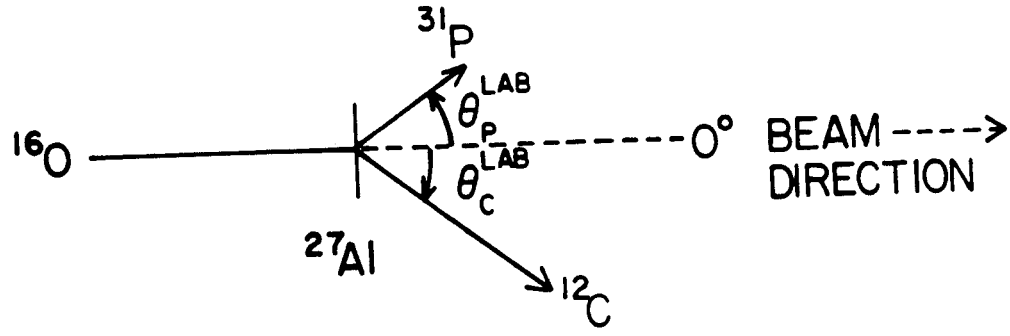

Fig. B.1. Two-body reaction $^{16}O + ^{27}Al \rightarrow ^{31}P + ^{12}C$

where E_i is the energy of particle i in the lab and Q_2 is the Q value of reaction B.1.

By conservation of momentum

$$\vec{P}_o = \vec{P}_c + \vec{P}_p \qquad \text{B.4}$$

where $\vec{P}_i$ is the momentum vector of particle i.

Decomposing B.4 into X and Y components:

$$|P_o| = |P_c|\cos\theta_c^{lab} + |P_p|\cos\theta_p^{lab} \qquad \text{B.5}$$

$$0 = |P_c|\sin\theta_c^{lab} + |P_p|\sin\theta_p^{lab} \qquad \text{B.6}$$

Squaring B.5 and B.6

$$|P_p|^2 = |P_o|^2 + |P_c|^2 - 2|P_o|\,|P_c|\cos\theta_c \qquad \text{B.7}$$

Using the relationship between energy and momentum $P^2 = 2mE$, B.7 becomes

$$m_pE_p = m_oE_o + m_cE_c - 2\sqrt{m_om_c\,E_oE_c}\cos\theta_c \qquad \text{B.8}$$

Rearranging Equation B.3

$$E_p = E_o - E_c - Q_2 \qquad \text{B.9}$$

Substituting B.9 into B.8 and squaring gives

$$\left(m_c + m_p\right)^2 E_c^2 + \left[2c\left(m_o + m_p\right) - 4m_o m_c E_o \cos^2\theta_c\right]E_c + c^2 = 0$$

$$E_c = \frac{-b \pm \sqrt{b^2 - 4ac}}{2a} \qquad \text{B.10}$$

where

$$a = \left(m_c + m_p\right)^2$$
$$b = -\left[2c\left(m_o + m_p\right) - 4m_o m_c E_o \cos^2\theta_c\right]$$
$$c = \left(m_o - m_p\right)E_o + Q_2$$

E_p is obtained from equation B.9 after E_c is calculated. From equation B.6

$$\sin\theta_p = -\left(\frac{m_c E_c}{m_p E_p}\right)^{1/2} \sin\theta_c \qquad \text{B.11}$$

Figure B.2 shows the velocity diagrams of Equations B.1 and B.2. The center-of-mass frame of $^{31}P^*$ will be centered at 0. Note that the polar axis of the lab system is chosen to be the beam direction while the polar axis of the ^{31}P center-of-mass system is defined to be along the $^{31}P^*$ recoil direction. In the rest frame of $^{31}P^*$, by conservation of energy,

$$E_p = E_\alpha^{cm} + E_{Al}^{cm} + Q_3 \qquad \text{B.12}$$

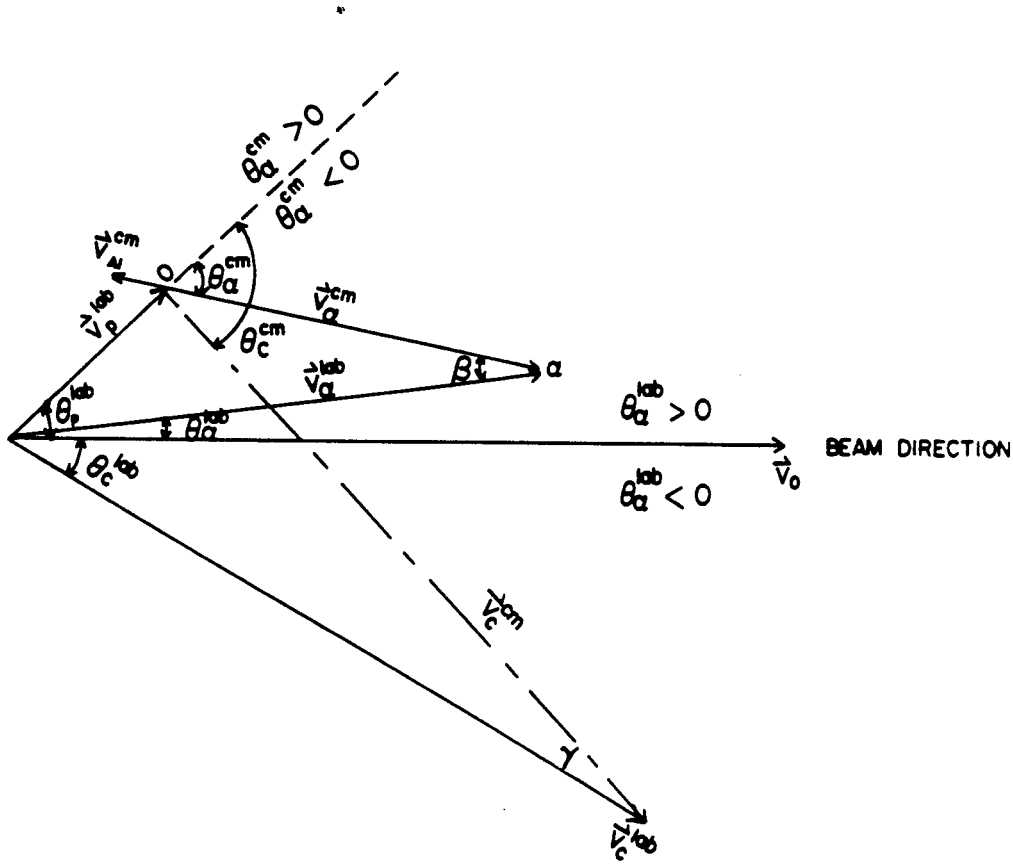

Fig B-2 Velocity diagram for the sequential process

$^{27}Al + ^{16}O \rightarrow ^{12}C + ^{31}P^*$; $^{31}P^* \rightarrow \alpha + ^{27}Al$

where Q_3 is the Q value of the break-up reaction B.2, E_p^* is the excitation energy of $^{31}P^*$ and E_i^{cm} is the energy of particle i in the $^{31}P^*$ center-of-mass frame.

Conservation of linear momentum gives:

$$\vec{P}_\alpha^{cm} = - \vec{P}_{Al}^{cm} \qquad \text{B.13}$$

where $\vec{P}_i^{cm}$ is the momentum vector of particle i in the center-of-mass system of $^{31}P^*$. Then the energies of Al and α can be related by

$$E_{Al}^{cm} = \frac{m_\alpha}{m_{Al}} E_\alpha^{cm} \qquad \text{B.14}$$

From Fig. B.2

$$\theta_\alpha^{cm} = -\left(\theta_p^{lab} - \theta_\alpha^{lab}\right) - \beta \qquad \text{B.15}$$

$$\frac{\sin\left(\theta_p^{lab} - \theta_\alpha^{lab}\right)}{|v_\alpha^{cm}|} = \frac{\sin\beta}{|v_p^{lab}|}$$

$$\sin\beta = \left(\frac{E_p\, m_\alpha}{E_\alpha^{cm}\, m_p}\right)^{1/2} \sin\left(\theta_p^{lab} - \theta_\alpha^{lab}\right) \qquad \text{B.16}$$

In order to eliminate the ϕ dependence in Ω in deriving the Jacobian, the direction of the velocity of $^{31}P^*$ is temporarily used as the polar axis

$$J_\alpha\left(\theta_\alpha^{lab}\right) = \frac{d\Omega_{lab}}{d\Omega_{cm}} = \left(\frac{d\Omega_{cm}}{d\Omega_{lab}}\right)^{-1}$$

$$= \left| \frac{\sin\theta_\alpha^{cm}}{\sin\left(\theta_p^{lab} - \theta_\alpha^{lab}\right)} \quad \frac{d\theta_\alpha^{cm}}{d\left(\theta_p^{lab} - \theta_\alpha^{lab}\right)} \right|^{-1} \qquad \text{B.17}$$

$$\frac{d\theta^{cm}}{d\left(\theta_p^{lab} - \theta_\alpha^{lab}\right)} = -\left(1 + \frac{d\beta}{d\left(\theta_p^{lab} - \theta_\alpha^{lab}\right)}\right)$$

$$= -\left(1 + \frac{1}{\cos\beta}\left(\frac{E_p\, m_\alpha}{E_\alpha^{cm}\, m_p}\right)^{1/2} \cos\left(\theta_p^{lab} - \theta_\alpha^{lab}\right)\right) \qquad \text{B.18}$$

$$J_\alpha\left(\theta_\alpha^{lab}\right) = \left(\frac{\sin\theta_\alpha^{cm}}{\sin\left(\theta_p^{lab} - \theta_\alpha^{lab}\right)} \quad X \right.$$

$$\left. \left(1 + \left(\frac{E_p\, m_\alpha}{E_\alpha^{cm}\, m_p}\right)^{1/2} \frac{\cos\left(\theta_p^{lab} - \theta_\alpha^{lab}\right)}{\cos\beta}\right)\right)^{-1} \qquad \text{B.19}$$

$J_c(\theta_c)$ can be found in a similar way as $J_\alpha\left(\theta_\alpha^{lab}\right)$

$$J_c(\theta_c) = \frac{\sin\theta_c^{cm}}{\sin\left(\theta_p^{lab} - \theta_c^{lab}\right)} \; X$$

$$\left(1 + \left(\frac{E_p\, m_c}{E_c^{cm}\, m_p}\right)^{1/2} \frac{\cos\left(\theta_p^{lab} - \theta_c^{lab}\right)}{\cos\gamma}\right)^{-1} \qquad \text{B.20}$$

where $\gamma = -\theta_c^{cm} - \theta_p^{lab} + \theta_c^{lab}$.

The angle transformations from θ_α^{lab} to θ_α^{cm} and the Jacobian $J_\alpha\left(\theta_\alpha^{lab}\right)$ for $\theta_c = -30°$ and $\theta_c = -40°$ have been plotted against θ_α^{lab} in Figures B.3 and B.4.

As shown in Figure IV.2, the out-of-plane data was taken in a plane perpendicular to the reaction plane and also contains the $^{31}P^*$ recoil direction. For a fixed Q value, the Jacobian and the center-of-mass angle between $^{31}P^*$ and alpha depend only on the relative laboratory angle between the $^{31}P^*$ and alpha particle. This means that $\phi_\alpha = 60°$, $\theta_\alpha = 43°$ has the same Jacobian and relative center-of-mass angle as $\theta_\alpha = 103°$, $\phi_\alpha = 0°$.

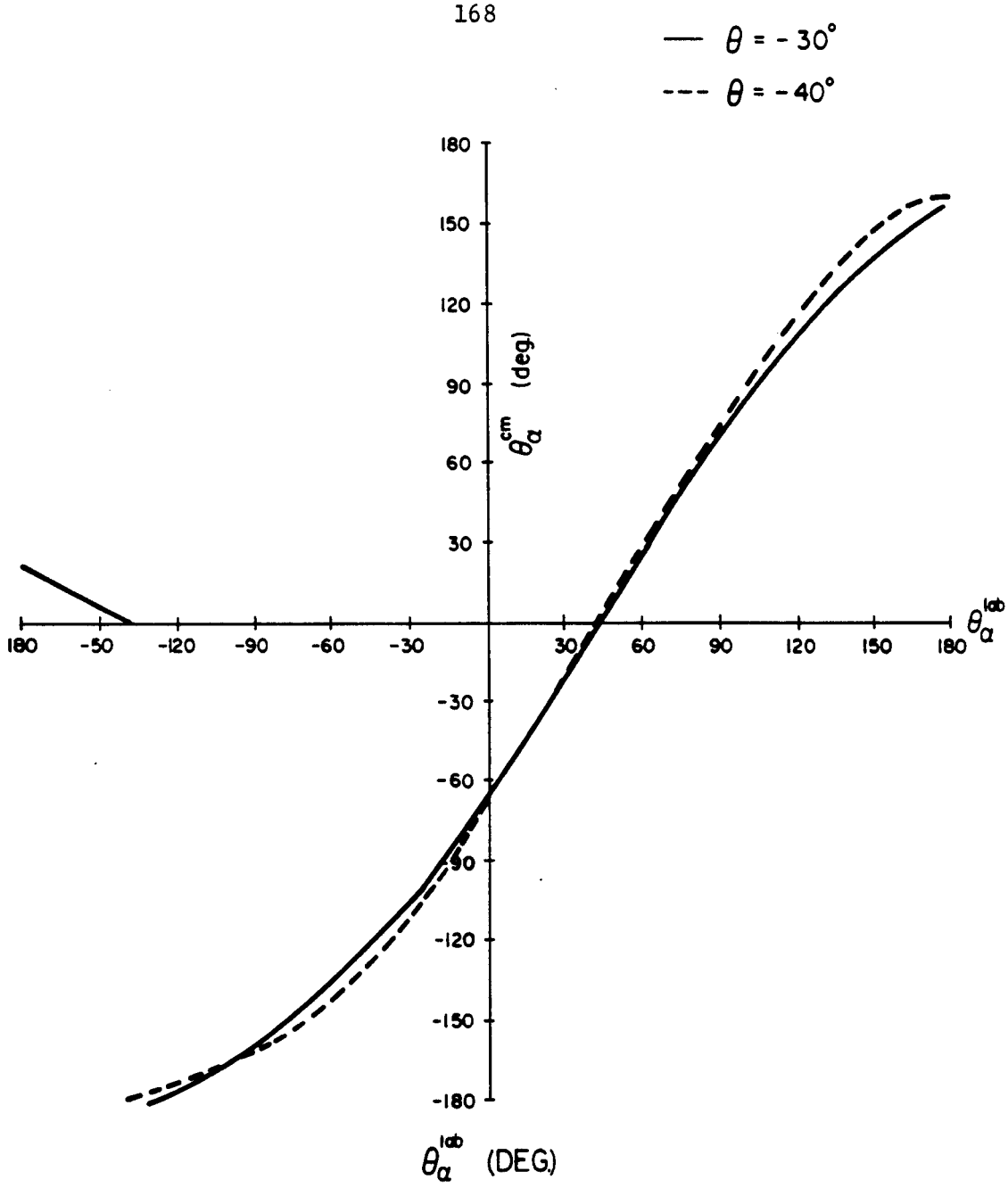

Fig. B-3 Alpha lab angle ($\theta_{\alpha x}^{lab}$) plotted as a function of $\theta_{\alpha x}^{cm}$ in the $^{31}P^*$ (E_x=14.5 MeV) center of mass system.

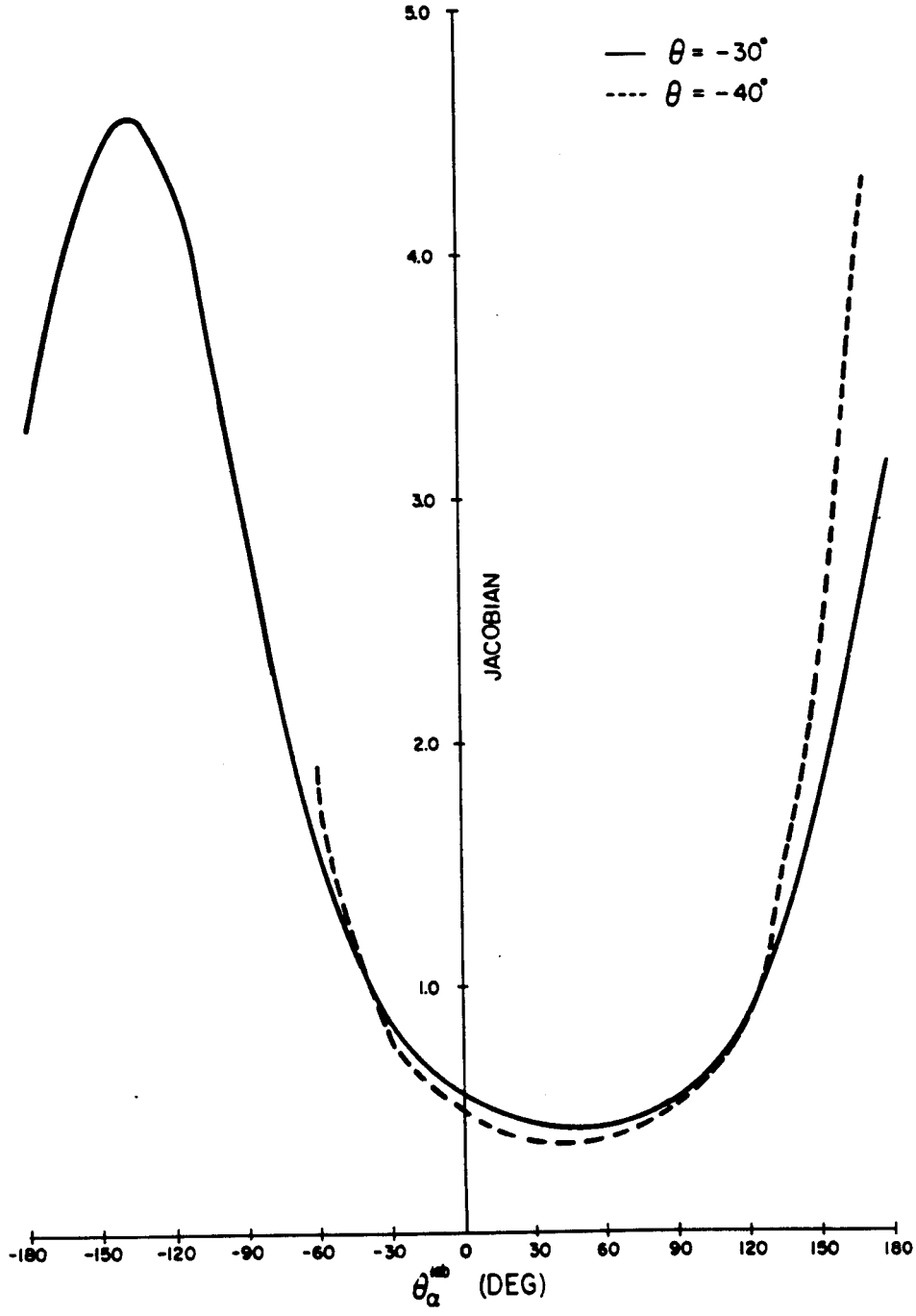

Fig B-4 Jacobian plotted as a function of alpha lab angle.

Appendix C

Charge Radius of ^{16}O

As described in Chapter VI-b, the ^{16}O is described as a bound state of a ^{12}C and an α particle. The ^{16}O wave function (ψ_o) can be expressed as the product of the individual wave functions of carbon (ϕ_c) and alpha ($\hat{\phi}_\alpha$) and the wave function that describes the relative motion of ^{12}C and α, $\left(\psi(\vec{r}_c - \vec{r}_\alpha)\right)$.

$$\psi_o = \psi(\vec{r}_c - \vec{r}_\alpha)\phi_c \hat{\phi}_\alpha \qquad C.1$$

where $\vec{r}_c$ and $\vec{r}_\alpha$ are the position vectors for the carbon and alpha particles respectively.

The mean square charge radius of a nucleus is defined to be

$$\langle r^2 \rangle = \frac{1}{Z} \langle \psi \left| \sum_{i=1}^{Z} \left(r_{p_i} - r_{cm} \right)^2 \right| \psi \rangle \qquad C.2$$

where p_i indicates individual proton in the nucleus with charge number Z, r_{cm} is the center of mass position.

From C.2, the mean square charge radii for ^{16}O, ^{12}C and α can be written as

$$\langle r_p^2 \rangle_o = \frac{1}{8} \langle \psi_o \left| \sum_{i=1}^{8} \left(r_{p_i} - r_o \right)^2 \right| \psi_o \rangle \qquad C.3$$

$$\langle r_p^2 \rangle_c = \frac{1}{6} \langle \phi_c \left| \sum_{i=1}^{6} \left(\vec{r}_{p_i} - \vec{r}_c \right)^2 \right| \phi_c \rangle \qquad C.4$$

$$\langle r_p^2 \rangle_\alpha = \frac{1}{2} \langle \hat{\phi}_\alpha \left| \sum_{i=1}^{2} \left(\vec{r}_{p_i} - \vec{r}_\alpha \right)^2 \right| \hat{\phi}_\alpha \rangle \qquad \text{C.5}$$

where $\vec{r}_o$, $\vec{r}_c$ and $\vec{r}_\alpha$ are the center of mass positions for ^{16}O, ^{12}C and α respectively. To simplify the derivation, ^{16}O is assumed to be at the origin, $\vec{r}_o = 0$. Then Eqs. C.1 and C.3 can be written as

$$\langle r_{p_o}^2 \rangle = \frac{1}{8} \langle \psi_o \left| \sum_{i=1}^{8} r_{p_i}^2 \right| \psi_o \rangle \qquad \text{C.6}$$

$$\psi_o = \psi(\vec{r}_c - \vec{r}_\alpha) \phi_c(\vec{r} - \vec{r}_c) \hat{\phi}_\alpha(\vec{r} - \vec{r}_\alpha) \qquad \text{C.7}$$

$$\sum_{i=1}^{8} r_{p_i}^2 = \sum_{i=1}^{2} r_{p_i}^2 + \sum_{i=1}^{6} r_{p_i}^2 \qquad \text{C.8}$$

Equation C.8 expresses the sum of $r_{p_i}^2$ operator into two groups, the first one operates on the protons in the α particle and the second one operates on the carbon particle. Then, with Eqs. C.7 and C.8, Eq. C.6 can be expanded into 2 terms

$$\langle r_{p_o}^2 \rangle = \frac{1}{8} \langle \psi(\vec{r}_c - \vec{r}_\alpha) \hat{\phi}_\alpha(\vec{r} - \vec{r}_\alpha) \left| \sum_{i=1}^{2} r_{p_i}^2 \right| \hat{\phi}_\alpha(\vec{r} - \vec{r}_\alpha) \psi(\vec{r}_c - \vec{r}_\alpha) \rangle$$

$$+ \frac{1}{8} \langle \psi(\vec{r}_c - \vec{r}_\alpha) \phi_c(\vec{r} - \vec{r}_c) \left| \sum_{i=1}^{6} r_{p_i}^2 \right| \phi_c(\vec{r} - \vec{r}_c) \psi(\vec{r}_c - \vec{r}_\alpha) \rangle \qquad \text{C.9}$$

The first term in the right hand side of Eq. C.9 can be further simplified if the identity $\vec{r}_p = (\vec{r}_p - \vec{r}_\alpha) + \vec{r}_\alpha$ is used, yielding

$$\frac{1}{8}\,\langle\psi(\vec{r}_c-\vec{r}_\alpha)\hat{\phi}_\alpha(\vec{r}-\vec{r}_\alpha)\Big|\sum_{i=1}^{2} r_{p_i}^{\,2}\Big|\hat{\phi}_\alpha(\vec{r}-\vec{r}_\alpha)\psi(\vec{r}_c-\vec{r}_\alpha)\rangle$$

$$= \frac{2}{8}\Bigg(\langle\hat{\phi}_\alpha(\vec{r}-\vec{r}_\alpha)\Big|(r_p-r_\alpha)^2\Big|\hat{\phi}_\alpha(\vec{r}-\vec{r}_\alpha)\rangle$$

$$+ \langle\psi(\vec{r}_c-\vec{r}_\alpha)\Big|r_\alpha^{\,2}\Big|\psi(\vec{r}_c-\vec{r}_\alpha)\rangle\Bigg) \qquad \text{C.10}$$

The cross term vanishes since $\langle\hat{\phi}(\vec{r}-\vec{r}_\alpha)\Big|(\vec{r}-\vec{r}_\alpha)\Big|\hat{\phi}(\vec{r}-\vec{r}_\alpha)\rangle = 0$.

To simplify the notation, the right hand side of C.10 can be written as $2[\langle r_p^{\,2}\rangle_\alpha + \langle r_\alpha^{\,2}\rangle_{c-\alpha}]$. Similarly the second term in the right hand side of equation C.9 becomes $\frac{6}{8}[\langle r_p^{\,2}\rangle_c + \langle r_c^{\,2}\rangle_{c-\alpha}]$. Thus C.9 can be written as $2[\langle r_p^{\,2}\rangle_\alpha + \langle r_\alpha^{\,2}\rangle_{c-\alpha}]$.

$$\langle r_p^{\,2}\rangle_o = \frac{1}{8}\Big(2\langle r_p^{\,2}\rangle_\alpha + 6\langle r_p^{\,2}\rangle_c + 2\langle r_\alpha^{\,2}\rangle_{c-\alpha} + 6\langle r_c^{\,2}\rangle_{c-\alpha}\Big) \qquad \text{C.11}$$

Since ^{16}O center of mass is defined as the origin, $\vec{r}_\alpha$ and $\vec{r}_c$ are related to the relative position of ^{12}C and α, $(r_{c-\alpha})$ by the following equation

$$|r_\alpha| = \frac{m_c}{m_o}\,|r_{c-\alpha}| \qquad \text{C.12}$$

$$|r_c| = \frac{m_\alpha}{m_o}\,|r_{c-\alpha}| \qquad \text{C.13}$$

From Eqs. C.12 and C.13, Eq. C.11 can be written as

$$\langle r_p^2 \rangle_o = 0.25\langle r_p^2 \rangle_\alpha + 0.75\langle r_p^2 \rangle_c + 0.1875\langle r_{c-\alpha}^2 \rangle \qquad \text{C.14}$$

The root mean square charge radii for ^{16}O, ^{12}C and α can be obtained from electron scattering data and are listed in the Atomic Data and Nuclear Data Table (De 74).

$$\langle r_p^2 \rangle_o^{1/2} = 2.73 \text{ fm}$$

$$\langle r_p^2 \rangle_\alpha^{1/2} = 1.71 \text{ fm}$$

$$\langle r_p^2 \rangle_c^{1/2} = 2.45 \text{ fm}$$

Then from Eq. C.14, $\langle r_{c-\alpha}^2 \rangle^{1/2} = 3.43$ fm.

In the three-body calculation, the ^{16}O nucleus consists of a ^{12}C particle and alpha particle in a bound state. The Woods-Saxon potential parameter $R_{c-\alpha} = 4.85$, $a_{c-\alpha} = 0.65$ are obtained from De Vries (De 73). The remaining parameter $U_{c-\alpha}^{nucl}$ is obtained by requiring the root mean square radius $\langle r_{c-\alpha}^2 \rangle^{1/2}$ defined as

$$\langle r_{c-\alpha}^2 \rangle = \frac{\int r^2 \, dt}{\int dt}$$

to be equal to the root mean square radius obtained earlier $\langle r_{c-\alpha}^2 \rangle^{1/2} = 3.43$ fm.

Appendix D

DISTRIBUTION SAMPLING USING THE MONTE CARLO METHOD

If an input parameter x has a probability density function f(x) over a range $a \leq x \leq b$, then the corresponding probability distribution function is defined to be

$$n = p(x) = \int_a^x f(x')dx' \qquad \text{D.1}$$

p(x) is set equal to the random number n, where n is uniformly distributed in the range [0,1], $0 \leq n < 1$, f(x) must satisfy the following constraints

$$p(a) = \int_a^a f(x')dx' = 0 \qquad \text{D.2}$$

$$p(b) = \int_a^b f(x')dx' = 1 \qquad \text{D.3}$$

Thus Eq. D.1 relates a random number n with the parameter x. Equation D.2 determines the integration constant which is always equal to zero and D.3 determines the normalization constant for f(x). The Monte Carlo method developed here to obtain any parameter x with a given probability density f(x) is very general. The procedure for obtaining x using Eqs. D.1, D.2, and D.3 will be illustrated with the three parameters b, $\phi_{c-\alpha}$ and $r_{c-\alpha}$ used to specify the initial conditions

in the three-body calculation discussed in Chapter VI-C. Since the subscript c-α is not relevant in the following discussion, it will be dropped from the notation of ϕ and r.

1. Impact parameter b

$$f(b) = N_b * b \qquad b_{fu} < b < b_{max} \qquad \text{D.4}$$

where N_b is the normalization constant. From Eq. D.1

$$n = p(b) = \int_{b_{fu}}^{b} f(b')db' = N_b(b^2 - b_{fu}^2) + k_b \qquad \text{D.5}$$

where k_b is the integration constant. From Eqs. D.2 and D.2

$$p(b_{fu}) = 0 \qquad k_b = 0 \qquad \text{D.6}$$

$$p(b_{max}) = 1 \qquad N_b = \frac{1}{b_{max}^2 - b_{fu}^2} \qquad \text{D.7}$$

Substituting the values of k_b and N_b into D.5,

$$n = \frac{b^2 - b_{fu}^2}{b_{max}^2 - b_{fu}^2} \qquad \text{D.8}$$

$$b = \left[n(b_{max}^2 - b_{fu}^2) + b_{fu}^2\right]^{1/2} \qquad \text{D.9}$$

2. In-plane c-α angle, ϕ

$$f(\phi) = N_\phi \qquad 0 \le \phi \le 2\pi \qquad \text{D.10}$$

$$n = N_\phi \int_o^\phi d\phi' = N_\phi * \phi + k_\phi \qquad \text{D.11}$$

From Eqs. D.1, D.2, and D.3

$$k_\phi = 0, \quad \text{and} \quad N_\phi = \frac{1}{2}$$

$$\phi = 2\pi n \qquad \text{D.13}$$

3. Relative distance of c-α, r

$$f(r) = \frac{N_r}{N(r)} \qquad r_1 < r < r_2 \qquad \text{D.14}$$

r_1, r_2 are the turning points and v(r) is the velocity of the alpha particle with respect to the carbon particle at the distance r.

$$v(r) = \frac{2(E - U(r))}{\mu} \qquad \text{D.15}$$

where E is the binding energy; U(r) is the Coulomb and nuclear potential, and μ is the reduced mass. With Eqs. D.1 and D.14

$$n = N_r \int_{r_1}^{r} \frac{1}{v(r)}\, dr + k_r \qquad \text{D.16}$$

r is an implicit variable in Eq. D.16. There is no simple equation relating r as a function of n.

$$k_r = 0$$

$$N_r = \frac{1}{\ln\left[\frac{v(r_2)}{v(r_1)}\right]} \qquad \text{D.17}$$

The following method is used to determine r as a function of n. The interval r_1 and r_2 is subdivided into 100 intervals,

$$r_1 < \ldots < r_i < r_{i+1} < \ldots < r_2$$

such that

$$p_{i+1}(r_{i+1}) - p_i(r_i) = N_r \int_{r_i}^{r_{i+1}} \frac{1}{v(r')}\, dr' = \frac{1}{100} \qquad \text{D.18}$$

for any i.

The values of r_i are first determined by numerically integrating D.18 with the trapezoidal rule. All the r_i are stored in a table. For any random number n, $p_i \leq n \leq p_{i+1}$, a corresponding r can be obtained by interpolating r_i and r_{i+1}.

VITA

ManYee Betty Tsang, a resident alien of United States, was born on November 20, 1951 in Kowloon, Hong Kong. She is the oldest child of Cheung-Ming Tsang and Wai-Chun Lai. She received her primary and secondary school education in Hong Kong and graduated from Saint Rose of Lima's Convent School in 1969.

She came to United States in 1970 and attended Taft College for a year. She received her Bachelor of Science degree in Mathematic from California State College, Bakersfield in 1973. She enrolled in the Chemistry Department of University of Washington in 1974 and joined the Nuclear Physics Laboratory in 1975